The HUNGARIAN JOURNAL OF INDUSTRY AND CHEMISTRY (HJIC)
formerly (until 2012) the Hungarian Journal of Industrial Chemistry

The HJIC is an international periodicals that focuses on results of fundamental and applied research in the field of

- Biotechnology
- Chemical Engineering Science
- Chemical Processes
- Energetics
- Environmental Chemistry
- Environmental Engineering & Technology
- Industrial Management
- Material Science
- Mechanical Engineering
- Mechatronics
- Process & System Engineering
- Recycling

in the form of original papers, reviews, short communications, and conference proceedings written in English.

EDITORIAL BOARD

EDITORIAL OFFICE: UNIVERSITY OF PANNONIA, P.O. BOX 158, VESZPRÉM, 8201 (HUNGARY)
Tel.: +36 (88) 624-746, e-mail: hjic@almos.uni-pannon.hu; web: hjic.mk.uni-pannon.hu
Felelős szerkesztő: Szilágyi Róbert Károly Nyelvi lektor: Matthew Chen
Kiadja: Pannon Egyetem, 8200 Veszprém, Egyetem u. 10.
Levélcím: H-8201 Veszprém, Postafiók 158, Tel.: (88) 624-000
Felelős kiadó: a Pannon Egyetem, Mérnöki Kar dékánja

Hung. J. Ind. & Chem. *2014*, Vol. 42(2), pp. 57-113

Table of Contents

EDITORIAL PREFACE

Systems and control theory is a constantly evolving scientific area and the dominant driving force in key industries and engineering fields e.g. process engineering, automotive engineering, bioengineering, and the energy industry. The aim of the current issue (Volume 42, Number 2) is to provide an overview of research topics pursued by selected PhD students.

The papers presented here were selected from contributions at the 13th International PhD Workshop on Systems and Control Conference held on August 25, 2014 (virt.uni-pannon.hu/phdws2014). The objective of the conference was to establish an international forum for young researchers. The meeting provided opportunities for the participants to present and discuss the latest results and up-to-date applications in systems and control.

This issue represents the entire spectrum of systems and control engineering as follows:

- process modelling and analysis
- control (traditional, intelligent, adaptive, etc.)
- process monitoring and supervision
- system identification and signal processing
- bioengineering
- traffic control
- reaction kinetic networks
- modelling of complex systems (classical, hierarchical, Bayesian, fuzzy, networks)
- image processing and pattern recognition
- artificial intelligence
- soft computing (neural, genetic, fuzzy algorithms, etc.)
- software (parallel computing, distributed and network computing, data visualization)
- decision making (decision support, data mining)
- applications of systems and control theory

The organizers are grateful for the contributions of the authors.

The tradition of the International PhD Workshop continues.
You are invited to participate at the 14th International PhD Workshop in Veszprém in 2015!

ATTILA MAGYAR
University of Pannonia, Veszprém, HUNGARY
Guest Editor

HUNGARIAN JOURNAL
OF INDUSTRY AND CHEMISTRY
VESZPRÉM
Vol. 42(2) pp. 57–64 (2014)

A COMPARISON OF ADVANCED NON-LINEAR STATE ESTIMATION TECHNIQUES FOR GROUND VEHICLES

GYÖRGY MAX✉ AND BÉLA LANTOS

[1] Department of Control Engineering and Informatics, Budapest University of Technology and Economics,
Magyar tudósok körútja 2, Budapest, 1117, HUNGARY
✉Email: max@iit.bme.hu

This paper presents a comparative examination of state-of-the-art non-linear state estimation techniques. First, the Sigma-Point (SPKF) stochastic estimators are investigated on the basis of the Unscented Transformation. This is followed by the technique of non-linear symmetry-preserving observers for non-linear dynamics on the basis of symmetrical LIE groups. The variety of the deterministic and stochastic state estimation algorithms is studied the kinematics of ground vehicles. Two cases are described that deal with the reliability of path tracking, the convergence and speed of off-line calibration.

Keywords: state estimation, invariant observers, unscented KALMAN filter, vehicle kinematics

Introduction

Vehicles are indispensable in modern society, and vehicle safety is consequently of importance in everyday life. A lack of information about the state of vehicle and parameters presents a major obstacle for the development of vehicle control systems.

The effectiveness of vehicle stability control largely depends on the accuracy of the vehicle state parameters that are measured by appropriate sensors. Unfortunately, measurements from these sensors contain bias, as well as electrical noise, and can drift with temperature changes. However, the state estimation method is also able to dramatically reduce errors introduced by measurement and process noise contained in the signal.

The focus of this work is the non-linear state estimation techniques. Firstly, the 'Sigma-Point KALMAN filter family' (SPKF) is discussed on the basis of the 'Unscented Transformation' (UT) and STERLING's interpolation [3, 5, 6]. Secondly, the symmetry-preserving observer is presented [15, 16, 18], which is based on Lie-transformation of invariant frames. The various state estimation procedures are then examined and compared through an illustrative non-linear example of vehicle kinematics.

Sigma-Point KALMAN Filters

Sigma-Point KALMAN filter [2, 4, 7] is a collective name for derivativeless KALMAN filters that employs the deterministic sampling based Sigma-point approach to calculate the optimal terms of the state estimation. Common methods use the Scaled Unscented Transformation [4] and STERLING's polynomial interpolation. The former replaces the original set of sigma-points with a transformed set in order to minimize the errors of higher order terms, the latter approximates the derivation of the divided difference filter [10, 11] and central difference filter in [12].

The Scaled Unscented Transformation

The Scaled Unscented Transformation (SUT) has two steps. First, a fixed number of sigma points is chosen to capture the desired moments (at least mean and covariance) of the original distribution. Then the sigma points are propagated through the non-linear function and the moments of the transformed variables are estimated. The advantage of SUT over the Taylor series based approximation is that SUT is better at capturing the higher order moments caused by the non-linear transformation, as discussed in [1, 8-10].

Consider a non-linear function $y = g(x)$ and assume x has mean $\bar{x}$ and covariance P_x. The first two moments of y are calculated by the following two steps:

1) Weighted Sigma-point selection:

$$\begin{aligned} X_0 &= \bar{x} \\ X_i &= \bar{x} + \left(\sqrt{(L+\lambda)P_x}\right)_{i=1\ldots L} \\ X_i &= \bar{x} - \left(\sqrt{(L+\lambda)P_x}\right)_{i=L+1\ldots 2L} \end{aligned} \tag{1}$$

with weights

$$\begin{aligned} w_0^m = \tfrac{\lambda}{L+\lambda} \qquad w_0^c &= \tfrac{\lambda}{L+\lambda} + (1-\alpha^2+\beta) \\ w_i^m = w_i^c &= \tfrac{\lambda}{2(L+\lambda)} \end{aligned} \tag{2}$$

where w_i^m, and w_i^c are associated with the i^{th} sigma-point such that $\sum_{i=0}^{2L} w_i = 1$. Symbols λ, α, and β denote scaling parameters and $\left(\sqrt{(L+\lambda)P_x}\right)_i$ is the i^{th} column of the matrix square root of the weighted $(L+\lambda)P_x$ covariance matrix.

2) Propagation: $Y_i = g(X_i)$

$$\begin{aligned} \bar{y} &\approx \sum_{i=0}^{2L} w_i^m Y_i \qquad P_y \approx \sum_{i=0}^{2L} w_i^c (Y_i - \bar{y})(Y_i - \bar{y})^T \\ P_{xy} &\approx \sum_{i=0}^{2L} w_i^c (X_i - \bar{x})(Y_i - \bar{y})^T \end{aligned} \tag{3}$$

where $\bar{y}$, P_y, and P_{xy} are the approximated mean, covariance and cross-covariance respectively.

The Unscented KALMAN Filter (UKF)

The algorithm of the UKF according to Refs. [3, 7, 8] consists of the following steps:

1) Initialization:

$$\hat{x}_0 = E\left[x_0\right],\ P_{x_0} = E\left[(x_0 - x_0)(x_0 - x_0)^T\right] \tag{4}$$

$$\hat{x}_0^a = E\left[\hat{x}_0^a\right] = \begin{bmatrix} \hat{x}_0^T & \bar{v}_0^T & \bar{n}_0^T \end{bmatrix}^T \tag{5}$$

$$P_0^a = \begin{bmatrix} P_{x_0} & 0 & 0 \\ 0 & R_v & 0 \\ 0 & 0 & R_n \end{bmatrix} \tag{6}$$

2) State estimation for $k = 1 \ldots \infty$:

a) Calculate Sigma-points:

$$X_{k-1}^a = \begin{bmatrix} \hat{x}_{k-1}^a & \hat{x}_{k-1}^a + \gamma\sqrt{P_{k-1}^a} & \hat{x}_{k-1}^a - \gamma\sqrt{P_{k-1}^a} \end{bmatrix} \tag{7}$$

b) Time-update:

$$\begin{aligned} X_{i,k|k-1}^x &= f(X_{i,k-1}^x, X_{k-1}^v, u_{k-1}), \quad i = 0,\ldots,2L \\ \hat{x}_k^- &= \sum_{i=0}^{2L} w_i^m X_{i,k|k-1}^x \\ P_{x_k}^- &= \sum_{i=0}^{2L} w_i^c (X_{i,k|k-1}^x - \hat{x}_k^-)(X_{i,k|k-1}^x - \hat{x}_k^-)^T \end{aligned} \tag{8}$$

c) Measurement-update:

$$\begin{aligned} Y_{i,k|k-1} &= h(X_{i,k|k-1}^x, X_{k-1}^n), \quad i = 0,\ldots,2L \\ \hat{y}_k^- &= \sum_{i=0}^{2L} w_i^m Y_{i,k|k-1} \\ P_{\hat{y}_k} &= \sum_{i=0}^{2L} w_i^c (Y_{i,k|k-1} - \hat{y}_k^-)(Y_{i,k|k-1} - \hat{y}_k^-)^T \\ P_{x_k y_k} &= \sum_{i=0}^{2L} w_i^c (X_{i,k|k-1}^x - \hat{x}_k^-)(Y_{i,k|k-1} - \hat{y}_k^-) \end{aligned} \tag{9}$$

$$\begin{aligned} K_k &= P_{x_k y_k} P_{\hat{y}_k}^{-1} \\ \hat{x}_k &= \hat{x}_k^- + K_k(y_k - \hat{y}_k^-) \\ P_{x_k} &= P_{x_k}^- - K_k P_{\hat{y}_k} K_k^T \end{aligned} \tag{10}$$

where $x_k^a = \begin{bmatrix} x_k^T & v_k^T & n_k^T \end{bmatrix}^T$ and $X_k^a = \begin{bmatrix} (X_k^x)^T & (X_k^v)^T & (X_k^n)^T \end{bmatrix}^T$ are the L dimension vectors of the augmented states and Sigma-points respectively, R_v and R_n are the covariances of the process and measurement noise respectively, $\gamma = \sqrt{L+\lambda}$, $\lambda = \alpha^2(L+\kappa)+L$, $\alpha = 10^{-3}$, $\kappa = 0$, $\beta = 2$, and w_i is the weighting parameter defined in *Eq.(2)*.

The Central-Difference KALMAN Filter

This approach is based on STERLING's polynomial interpolation, which was used in the derivations of divided difference filter [10, 11] and central difference filter in Ref. [12]. The result of this approximation can be used for sigma-point approach as in the case of SUT. The algorithm consists of the following steps:

1) Weighted Sigma-point selection:

$$\begin{aligned} X_0 &= \bar{x} \\ X_i &= \bar{x} + \left(h\sqrt{P_x}\right)_{i=1\ldots L} \\ X_i &= \bar{x} - \left(h\sqrt{P_x}\right)_{i=L+1\ldots 2L} \end{aligned} \tag{11}$$

with weights

$$w_0^m = \frac{h^2 - L}{h^2},\ w_i^m = \frac{1}{2h^2},\ w_i^{c_1} = \frac{1}{4h^2},\ w_i^{c_2} = \frac{h^2 - 1}{4h^2}, \tag{12}$$

where w_i^m, and w_i^c are associated with i = 1, …, $2L$ sigma-point.

2) Initialization: the same as defined in *Eqs.(4-6)*

3) State estimation for k = 1, …, ∞:

a) Sigma-points for time-update:

$$\hat{x}_{k-1}^{a_v} = \begin{bmatrix} \hat{x}_{k-1} & \bar{v} \end{bmatrix},\ P_{k-1}^{a_v} = \begin{bmatrix} P_{x_{k-1}} & 0 \\ 0 & R_v \end{bmatrix} \tag{13}$$

$$X_{k-1}^{a_v} = \begin{bmatrix} \hat{x}_{k-1}^{a_v} & \hat{x}_{k-1}^{a_v} + h\sqrt{P_{k-1}^{a_v}} & \hat{x}_{k-1}^{a_v} - h\sqrt{P_{k-1}^{a_v}} \end{bmatrix} \tag{14}$$

b) Time-update:

$$\begin{aligned} X_{i,k|k-1}^x &= f(X_{i,k-1}^x, X_{k-1}^v, u_{k-1}), \quad i = 0,\ldots,2L \\ \hat{x}_k^- &= \sum_{i=0}^{2L} w_i^m X_{i,k|k-1}^x \\ P_{x_k}^- &= \sum_{i=1}^{L} w_i^{c_1} (X_{i,k|k-1}^x - X_{L+i,k|k-1}^x)^2 + \\ &\quad \sum_{i=1}^{L} w_i^{c_2} (X_{i,k|k-1}^x + X_{L+i,k|k-1}^x - 2X_{0,k|k-1}^x)^2 \end{aligned} \tag{15}$$

c) Sigma-points for measurement-update:

$$\hat{x}_{k-1}^{a_n} = \begin{bmatrix} \hat{x}_k^- & \bar{n} \end{bmatrix}, P_{k|k-1}^{a_n} = \begin{bmatrix} P_{x_k}^- & 0 \\ 0 & R_n \end{bmatrix} \quad (16)$$

$$X_{k|k-1}^{a_n} = \begin{bmatrix} \hat{x}_{k|k-1}^{a_n} & \hat{x}_{k|k-1}^{a_n} + h\sqrt{P_{k|k-1}^{a_n}} & \hat{x}_{k|k-1}^{a_n} - h\sqrt{P_{k|k-1}^{a_n}} \end{bmatrix} \quad (17)$$

d) Measurement-update:

$$\begin{aligned} Y_{i,k|k-1} &= h(X_{i,k|k-1}^x, X_{k|k-1}^n), \quad i = 0,\ldots,2L \\ \hat{y}_k^- &= \sum_{i=0}^{2L} w_i^m Y_{i,k|k-1} \\ P_{\hat{y}_k} &= \sum_{i=0}^{2L} w_i^{c_1} (Y_{i,k|k-1} - Y_{L+i,k|k-1})^2 + \\ &\quad \sum_{i=0}^{2L} w_i^{c_2} (Y_{i,k|k-1} + Y_{L+i,k|k-1} - 2Y_{0,k|k-1})^2 \quad (18) \\ P_{x_k y_k} &= \sqrt{w_1^{c_1} P_{x_k}^-} (Y_{1:L,k|k-1} - Y_{L+1:2L,k|k-1})^T \\ K_k &= P_{x_k y_k} P_{\hat{y}_k}^{-1} \\ \hat{x}_k &= \hat{x}_k^- + K_k (y_k - \hat{y}_k^-) \\ P_{x_k} &= P_{x_k}^- - K_k P_{\hat{y}_k} K_k^T \end{aligned}$$

Symmetry-Preserving Observers

Among many problems in control theory, the symmetric nature of the system can be utilized, such as in the case of optimal control for feedback or regulations. The symmetry properties can also be used in the design of observers. Symmetry-preserving observers are also known as invariant observers that are based on the differential geometric background of abstract LIE-groups [15, 16, 18].

The constructive algorithm can be defined for designing invariant observers, which is based on the group transformation of symmetry. The aim is to produce invariant frames and invariant output errors to transform a locally asymptotically convergent observer around an equilibrium point into an invariant one, retaining its first-order approximation. The method in Refs. [16, 18] benefits from the fact that the error equations and the first-order approximation can be calculated explicitly and the relationships can be defined globally. In addition, the invariant error equations make stability issues easier to deal with [19-21].

Assumptions

Suppose G is a LIE-group with identity e on manifold Σ. The group transformation $(\varphi_g)_{g\in G}$ on Σ is a smooth mapping

$$(g,\xi) \in G \times \Sigma \to \varphi_g(\xi) \in \Sigma \quad (19)$$

such that $\varphi_e(\xi) = \xi$ and $\varphi_{g_2}(\varphi_{g_1}(\xi)) = \varphi_{g_2 g_1}(\xi)$ for ζ, g_1, and g_2. The transformation group is local if $\varphi_g(\xi)$ is defined only when g lies sufficiently near to e. We consider only local transformations.

Invariant observers are designed for the smooth non-linear system

$$\frac{d}{dt}x = f(x,u), \; y = h(x,u) \quad (20)$$

where x, u, and y belong to the open subsets $\mathrm{X} \subset \mathbb{R}^n$, $\mathrm{U} \subset \mathbb{R}^m$, and $\mathrm{Y} \subset \mathbb{R}^p$ respectively and $p \le n$. Let $r \le n$ be the dimension of the LIE-group. We assume that for each x the mapping $x \to \phi_g(x)$ is full rank. Time functions $u(t)$ and $y(t)$ are known.

Invariant Pre-Observer

For the differential geometric description of the symmetric observers [14], the following definitions and theorems should be introduced:

Definition 1. The group of local transformation on manifold $\mathrm{X} \times \mathrm{U}$ is expressed by

$$(X,U) = (\phi_g(x), \psi_g(u)) \quad (21)$$

where $\phi_g(x), \psi_g(u)$ is local diffeomorphism and $g \in G$

Definition 2. System $\frac{d}{dt}x = f(x,u)$ is G-invariant, if $f(\phi_g(x), \psi_g(u)) = D\phi_g(x) \cdot f(x,u)$ for g, x, u. Thus, the system remains unchanged for the local transformation, $\dot{X} = f(X,U)$.

Definition 3. The output $y = h(x,u)$ is G-equivariant, if there exists ρ_g transformation on Y, such that $g \in G$ and $h(\phi_g(x), \psi_g(u)) = \rho_g(h(x,u))$ for g, x, u. Thus, the output remains unchanged for the local transformation, $Y = h(X,U)$.

Definition 4. The vector field w is G-invariant on manifold X, if $\frac{d}{dt}x = w(x)$ is invariant to the transformation, i.e. $w(\phi_g(x)) = D\phi_g(x) \cdot w(x)$ for g, x.

Definition 5. An invariant frame (w_1, w_2, …, w_3) consists of n linearly point-wise independent G-invariant vector fields on X thus $(w_1(x), w_2(x), \ldots, w_n(x))$ is a basis of the tangent space $T_{\mathrm{X}}(x)$.

Lemma 1. The invariant frame can be constructed from the canonical basis of X. The vector field defined by

$$w_i(x) = (D\phi_{\gamma(x)})^{-1} \cdot \frac{\partial}{\partial x_i} \quad (22)$$

for i = 1, …, n forms an invariant frame.

Definition 6. The system $\frac{d}{dt}\hat{x} = F(\hat{x},u,y)$ is a pre-observer, if $F(x,u,h(x,u)) = f(x,u)$ is satisfied for x and u. Furthermore, if $\lim \hat{x}(t) = x(t)$ as $t \to \infty$, then the pre-observer is asymptotic.

Definition 7. The pre-observer is G-invariant, if

$$F(\varphi_g(\hat{x}),\psi_g(u),\rho_g(y)) = D\varphi_g(\hat{x})\cdot F(\hat{x},u,y) \qquad (23)$$

is satisfied for g, $\hat{x}$, u, and y i.e. the observer remains unchanged for the group transformation on $\mathrm{X},\mathrm{U},\mathrm{Y}$.

Thus, $X=\phi_g(x)$, $U=\psi_g(u)$, $Y=\rho_g(y)$, and $\frac{d}{dt}\hat{X}=F(\hat{X},U,Y)$.

An invariant observer is an asymptotic G-invariant pre-observer. Moreover, if the pre-observer is G-invariant and $\operatorname{rank}(F)=\dim y$, then the output map y is G-equivariant.

Definition 8. Smooth map $(\hat{x},u,y)\to E(\hat{x},u,y)\in\mathbb{R}^{\mathrm{p}}$ is an invariant output error if

a) $y\to E(\hat{x},u,y)$ is invertible for $\hat{x}$, u, and y

b) $E(\hat{x},u,h(\hat{x},u))=0$ for $\hat{x}$ and u

c) $E(\phi_g(\hat{x}),\psi_g(u),\rho_g(y))=E(\hat{x},u,y)$ for $\hat{x}$, u, and y.

The first two properties mean E is an output error, the third expresses the invariance. The introduction of the invariant error is necessary, because the output error $\hat{y}-y$ does not usually preserve the geometry of the system [21].

The following three theorems [15, 16] support the construction of the symmetry-preserving observers.

Theorem 1. The observer $\frac{d}{dt}\hat{x}=F(\hat{x},u,y)$ is a G-invariant pre-observer for the G-invariant non-linear *Eq.(20)* with a G-equivariant output if and only if

$$F(\hat{x},u,y)=f(\hat{x},u)+\sum_{i=1}^{n}L_i(I(\hat{x},u),E(x,u,y))w_i(\hat{x}) \qquad (24)$$

where E is an invariant output error, $(\hat{x},u)\to I(\hat{x},u)\in\mathbb{R}^{\mathrm{n+m-r}}$ is a full rank function, L_i is a smooth function, such that $L_i(I(\hat{x},u),0)=0$ and $(w_1,w_2,\ldots,w_n)$ is an invariant frame. Since $L_i(I,E)=\bar{L}_i(I,E)E$

$$\sum_{i=1}^{n}L_i(I,E)w_i=\sum_{i=1}^{n}w_i(\bar{L}_i(I,E)E) =\begin{pmatrix} w_1 & \ldots & w_n \end{pmatrix}\begin{pmatrix} \bar{L}_1(I,E)\\ \vdots \\ \bar{L}_n(I,E)\end{pmatrix}E \qquad (25)$$

The observer can be written as follows

$$F(\hat{x},u,y)=f(\hat{x},u)+W(\hat{x})L(I(\hat{x},u),E(\hat{x},u,y))E(\hat{x},u,y). \qquad (26)$$

Theorem 2. The following statements are valid:

- $(\hat{x},u,y)\to E(\hat{x},u,y)$ invariant output error exists,
- there is a $(\hat{x},u)\to I(\hat{x},u)\in\mathbb{R}^{\mathrm{n+m-r}}$ invariant function,
- every other invariant output error has the form of

$$\tilde{E}(\hat{x},u,y)=L(I(\hat{x},u),E(\hat{x},u,y)) \qquad (27)$$

where L is a smooth function such that $L(I, 0) = 0$ and $E\to L(I,E)$ is invertible.

Theorem 3. Consider the equilibrium of a non-linear system

$$f(\bar{x},\bar{u})=0 \text{ and } \bar{y}=h(\bar{x},\bar{u})$$

Assume that the linearized system A,B,C,D around this equilibrium is observable, where

$$A=\tfrac{\partial f}{\partial x}(\bar{x},\bar{u}),\ B=\tfrac{\partial f}{\partial u}(\bar{x},\bar{u}),\ C=\tfrac{\partial h}{\partial x}(\bar{x},\bar{u}),\ A=\tfrac{\partial h}{\partial u}(\bar{x},\bar{u})$$

and let L be such that $A+LC$ is a stable matrix. From the locally asymptotically convergent observer

$$\tfrac{d}{dt}\hat{x}=f(\hat{x},u)+L(\hat{y}-y),\ \hat{y}=h(\hat{x},u) \qquad (28)$$

an invariant observer can be constructed by the same linear approximation

$$\tfrac{d}{dt}\hat{x}=f(\hat{x},u)+W(\hat{x})\bar{L}(I(\hat{x},u),E(\hat{x},u,y))E(\hat{x},u,y) \qquad (29)$$

where $\bar{L}=-W(x)^{-1}LV^{-1}$ and $V=\frac{\partial E}{\partial y(\bar{x},\bar{u},\bar{y})}$ is an invertible matrix of $p\times p$ dimensions.

There is no general algorithm for designing the L_{i} gain functions of *Theorem 1*. However, if we consider the following invariant state error

$$\eta(x,\hat{x})=\phi_{\gamma(x)}(\hat{x})-\phi_{\gamma(x)}(x) \qquad (30)$$

instead of the $\hat{x}-x$ state error, where $\gamma(x)$ is the solution of

$$\phi_g^a(x)=c \qquad (31)$$

with respect to g, then the invariant error will only depend on the $I(x,u)$ trajectories.

Constructive Algorithm

Consider an invariant system, i.e. unchanged by transformation *Eq.(21)* with an equivariant output (*Definition 3*). The non-linear observer design for non-linear dynamic systems [10, 11] can be divided into the following steps:

a) Choose a G LIE-group and a group transformation taking into account the symmetrical properties of the system.
b) Solve the normalization *Eq.(31)*. Build an invariant error E and the complete set of scalar invariants I.
c) Construct the invariant frame *Eq.(22)*.
d) Determine the pre-observer *Eq.(25)*.
e) Linearize the system $f(\bar{x},\bar{u})=0$ around the equilibrium and obtain *A,B,C,D* matrices. Check the observability and design an invariant observer from the chosen linear observer by using *Theorem* 3. Choose an appropriate $\bar{L}$.
f) Choose the parameters of the linearized error equations, based on the invariant state-errors η, such that the invariant system will be asymptotically stable.

Then the non-linear symmetry-preserving observer is asymptotically stable, and converges locally and exponentially along all system trajectories.

Case Study: A Non-Holonomic Vehicle

In this section, the previously introduced state estimation procedures are employed for an example of a non-holonomic vehicle tracking control. The well-known model in the robotics of the simplified vehicle kinematics is considered. The tracking is maintained by satisfying the kinematic constraints with the appropriate choice of reference signals.

Kinematic Model

The simplified kinematic model of the vehicle can be written in the following form

$$\begin{pmatrix} \dot{x} \\ \dot{y} \\ \dot{\theta} \end{pmatrix} = \begin{pmatrix} u\cos\theta \\ u\sin\theta \\ uv \end{pmatrix}, \; h(x,y,\theta) = (x,y) \tag{32}$$

where u is the velocity, v is the curvature, i.e. a function of the steering angle and h is the measured output. All signals contain additive Gaussian noise. The model assumes that the contact point of the wheel and the ground does not slip. Notice, that the linearized system is not observable.

Tracking

For path tracking the control signals are set to satisfy the kinematic constraints, thus u and v are calculated as follows:

$$u(t) = \sqrt{\dot{x}_r^2(t) + \dot{y}_r^2(t)} \text{ and } v(t) = \frac{\ddot{y}_r(t)\dot{x}_r(t) - \dot{x}_r(t)\ddot{y}_r(t)}{u^3(t)} \tag{33}$$

where $x_r(t)$ and $y_r(t)$ are time functions of the reference signal. The initial conditions for tracking control is

$$\theta_r(0) = \tan^{-1}\left(\frac{\dot{y}_r(0)}{\dot{x}_r(0)}\right). \tag{34}$$

Hence, the reference signals for the vehicle velocity and steering function can be calculated. In the simulations, sinusoidal path tracking is implemented using the reference signals

$$x_r(t) = t, \text{ and } y_r(t) = A\sin(\omega t).$$

Invariant Observer Design

Group Transformation

Eq.(32) is independent of the origin and of the orientation of the frame chosen, i.e. it is invariant with regards to the group of rotations and translations. We chose the Lie-group $G = SE(2)$ and defined the group transformation as follows:

$$\begin{aligned} \phi_{(x_g,y_g,\theta_g)}(x,y,\theta) &= \begin{pmatrix} x_g \\ y_g \\ \theta_g \end{pmatrix} \cdot \begin{pmatrix} x \\ y \\ \theta \end{pmatrix} = \\ &= \begin{pmatrix} x\cos\theta_g - y\sin\theta_g + x_g \\ x\sin\theta_g + y\cos\theta_g + y_g \\ \theta + \theta_g \end{pmatrix} \end{aligned} \tag{35}$$

$$\psi_{(x_g,y_g,\theta_g)}(u,v) = \begin{pmatrix} u \\ v \end{pmatrix}$$

$$\rho_{(x_g,y_g,\theta_g)}(x,y) = \begin{pmatrix} x\cos\theta_g - y\sin\theta_g + x_g \\ x\sin\theta_g + y\cos\theta_g + y_g \end{pmatrix}$$

One can check that *Eq.(32)* is invariant to the transformations φ, and ψ in terms of *Definition 1* and the output is equivariant to transformation ρ in terms of *Definition 3*.

Invariant Output Errors

The normalization *Eq.(31)* for $c = 0$:

$$\begin{aligned} 0 &= x\cos\theta_\gamma - y\sin\theta_\gamma + x_\gamma \\ 0 &= x\sin\theta_\gamma + y\cos\theta_\gamma + y_\gamma \\ 0 &= \theta + \theta_\gamma \end{aligned} \tag{36}$$

The solution of *Eq.(36)*, the scalar invariants and output errors can be written as follows respectively

$$\begin{pmatrix} x_\gamma \\ y_\gamma \\ \theta_\gamma \end{pmatrix} = \begin{pmatrix} x \\ y \\ \theta \end{pmatrix}^{-1} = \begin{pmatrix} -x\cos\theta - y\sin\theta \\ x\sin\theta - y\cos\theta \\ -\theta \end{pmatrix} = \gamma \begin{pmatrix} x \\ y \\ \theta \end{pmatrix} \tag{37}$$

$$I(x,y,\theta,u,v) = \psi_{\gamma(x,y,\theta)}(u,v) = \begin{pmatrix} u \\ v \end{pmatrix} \tag{38}$$

$$\begin{aligned} E &= \rho_{(x_\gamma,y_\gamma,\theta_\gamma)}(\hat{x},\hat{y}) - \rho_{(x_\gamma,y_\gamma,\theta_\gamma)}(x,y) \\ &= \begin{pmatrix} \cos\hat{\theta} & \sin\hat{\theta} \\ -\sin\hat{\theta} & \cos\hat{\theta} \end{pmatrix} \begin{pmatrix} \hat{x} - x \\ \hat{y} - y \end{pmatrix} \end{aligned} \tag{39}$$

Invariant Frame

$$\begin{aligned} W &= (D\phi_{\gamma(x,y,\theta)}(x,y,\theta))^{-1} \frac{\partial}{\partial(x,y,\theta)} = \\ &= D\phi_{\gamma(x,y,\theta)}(x,y,\theta) = \begin{pmatrix} \cos\theta & -\sin\theta & 0 \\ \sin\theta & \cos\theta & 0 \\ 0 & 0 & 1 \end{pmatrix}. \end{aligned} \tag{40}$$

Invariant pre-observer

$$\frac{d}{dt}\begin{pmatrix}\hat{x}\\ \hat{y}\\ \hat{\theta}\end{pmatrix}=\begin{pmatrix}u\cos\hat{\theta}\\ u\sin\hat{\theta}\\ uv\end{pmatrix}+\begin{pmatrix}\cos\hat{\theta} & -\sin\hat{\theta} & 0\\ \sin\hat{\theta} & \cos\hat{\theta} & 0\\ 0 & 0 & 1\end{pmatrix}\bar{L}\times \begin{pmatrix}\cos\hat{\theta} & \sin\hat{\theta}\\ -\sin\hat{\theta} & \cos\hat{\theta}\end{pmatrix}\begin{pmatrix}\hat{x}-x\\ \hat{y}-y\end{pmatrix} \tag{41}$$

where $\bar{L}$ is a smooth 3×2 gain matrix, whose elements depend on the invariant error E and the invariants I.

Error Equations and Error Dynamics

$$\eta=\begin{pmatrix}\eta_x\\ \eta_y\\ \eta_\theta\end{pmatrix}=\gamma(\hat{x},\hat{y},\hat{\theta})\begin{pmatrix}\hat{x}\\ \hat{y}\\ \hat{\theta}\end{pmatrix}-\gamma(\hat{x},\hat{y},\hat{\theta})\begin{pmatrix}x\\ y\\ \theta\end{pmatrix}= =\begin{pmatrix}(\hat{x}-x)\cos\hat{\theta}+(\hat{y}-y)\sin\hat{\theta}\\ -(\hat{x}-x)\sin\hat{\theta}+(\hat{y}-y)\cos\hat{\theta}\\ (\hat{\theta}-\theta)\end{pmatrix} \tag{42}$$

$$\begin{pmatrix}\dot{\eta}_x\\ \dot{\eta}_y\\ \dot{\eta}_\theta\end{pmatrix}=\begin{pmatrix}u(1-\cos\eta_\theta)+(uv+\bar{L}_{31}\eta_x+\bar{L}_{32}\eta_y)\eta_y\\ u\sin\eta_\theta-(uv+\bar{L}_{31}\eta_x+\bar{L}_{32}\eta_y)\eta_x\\ 0\end{pmatrix}+ +\bar{L}\begin{pmatrix}\eta_x\\ \eta_y\end{pmatrix} \tag{43}$$

It can be seen that the invariant error equations are independent of the trajectory and only depend on the relative quantities η_x, η_y, and η_θ and the I invariants.

Stability and Convergence

The weighting matrix is defined as follows

$$\bar{L}=\begin{pmatrix}-|u|a & ubE_y-uv\\ uv-ubE_y & -|u|c\\ 0 & -ub\end{pmatrix}, \tag{44}$$

where a and b are $c$are positive scalars and $E_y = \eta_y$. The invariant error dynamics can be made locally asymptotically stable. Furthermore, the resulting symmetry-preserving observer is almost globally asymptotically convergent, i.e. it converges any initial condition except for one as described in Refs. [15-16].

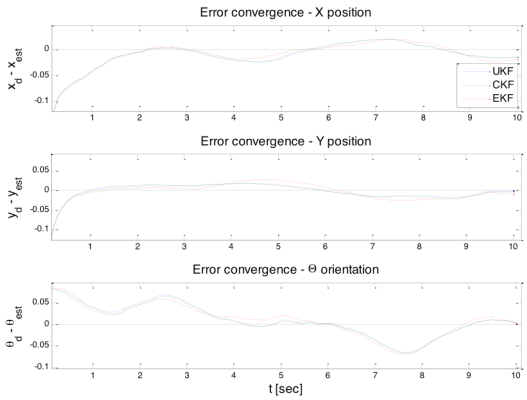

Figure 2: Estimation errors of the sigma-point and extended KALMAN filters from Example 1

Simulation Results

The state estimation techniques are illustrated in two tracking examples. For comparative purposes, the following algorithms have been implemented: Extended KALMAN Filter (EKF), Central Difference and Unscented KALMAN Filter (CKF, UKF) and the symmetry preserving observer (SYM) discretized by the sample time of the sigma-point estimators.

The reference paths are $x_r(t)=t$, and $y_r(t)=A\sin(\omega t)$, where A = 3 m and ω = π/5 rad s^{-1}. Zero mean additive Gaussian noise is assumed with standard deviations of 0.01 and 0.005 for the process noise and 0.02 for the measurement noise. The sampling time is T_s = 0.1 s. The initial values are $x_0^{est}=y_0^{est}=\theta_0^{est}=1$, and $x_0=y_0=0$.

Example 1

The vehicle starts from the origin of the *xy*-plane with large initial estimation error and tracks a sinusoidal path. *Fig.1* shows the estimated output positions of the vehicle using sigma-point KALMAN filters and symmetry-preserving observers. The estimation errors of different algorithms can be seen in *Figs.2* and *3*.

The errors are smaller and show smoother signals in the case of the SPKF estimators, which was expected, since the SYM observer is deterministic. Large errors appear at the peak values of the reference signals; however, both estimation techniques achieved the same satisfactory results in spite of the relatively small sampling frequency.

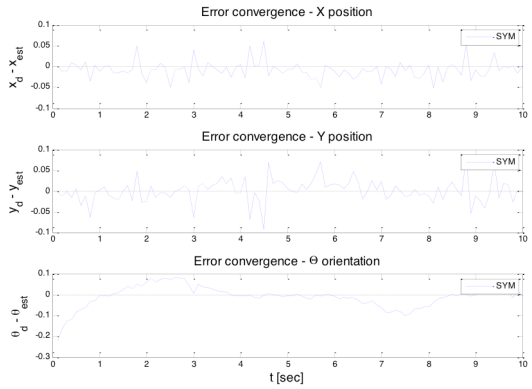

Figure 3: Estimation errors of the symmetry-preserving observer (SYM) from Example 1

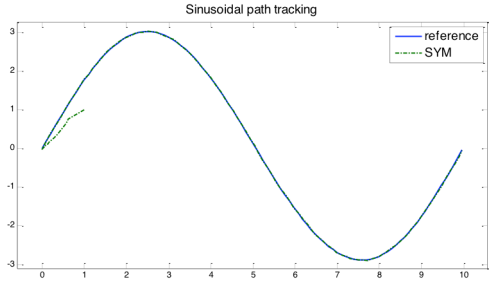

Figure 5: Estimated output position of the vehicle using symmetry-preserving observer (SYM) from Example 2

Table 1: Root-mean-squared errors of the estimated signals from Example 1

RMSE	x, m	y, m	θ, rad
UKF	0.1368	0.1587	0.0338
CKF	0.1366	0.1577	0.0336
EKF	0.1371	0.1551	0.0352
SYM	0.1371	0.1628	0.0455

Table 2: Root-mean-square errors of the estimated signals from Example 2

RMSE	x, m	y, m	θ, rad
UKF	0.0998	0.1180	0.0627
CKF	0.0993	0.1175	0.0628
EKF	0.1013	0.1165	0.0648
SYM	0.1264	0.1453	0.0760

Root-mean-square errors can be seen in *Table 1*. We can conclude that among the processes of state estimation techniques the SYM observer is competitive with SPKF estimators.

Example 2

In this example the vehicle performs an off-line estimation before movement starts, followed by an on-line estimation along a sinusoidal path. It is notable that in the stationary state the velocity is zero and at the beginning of movement the velocity changes to a non-zero value abruptly, see *Eq.(33)*. *Figs.4-7* illustrate the estimated output positions and the measurement errors for the sigma-point estimators and the invariant observers respectively

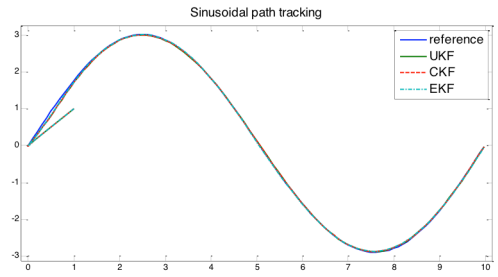

Figure 4: Estimated output position of the vehicle using sigma-point state estimation (UKF, CKF) and extended KALMAN Filter (EKF) from Example 2

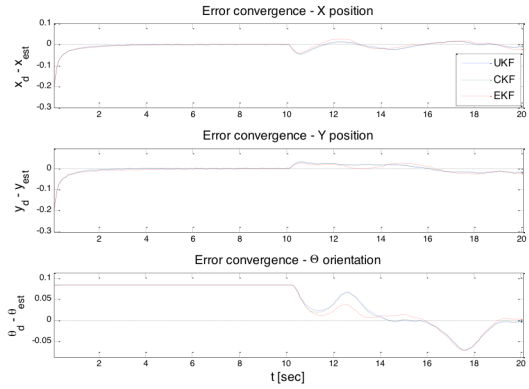

Figure 6: Estimation errors of the sigma-point and the extended KALMAN filters from Example 2

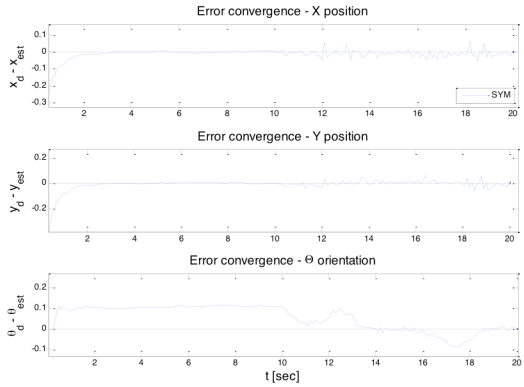

Figure 7: Estimation errors of the symmetry-preserving observer (SYM) from Example 2

The error signals show a quick convergence in the case of the symmetry-preserving observer. The speed of convergence depends on the parameters set in the $\bar{L}$ matrix; however, high gains can cause the observer to be divergent and make larger errors. Since there are no u and δ signals in the stationary position and the orientation is not directly measured, the orientation can only be estimated after the vehicle starts moving.

The error signal oscillates around zero in a similar way to Example 1. Due to calibration, smaller errors appear. The invariant observer and sigma-point estimators have the same magnitude of error components. The root-mean-square errors of the simulation can be seen in *Table 2*.

Conclusion

In this paper we presented a comparison of two different recently developed state estimation techniques. The Sigma-Point (SPKF) stochastic estimator is based on the Unscented Transformation and the non-linear symmetry-preserving observers are based on the group transformation of symmetrical LIE groups and invariant frames. Two examples are considered for the estimation of vehicle kinematics: the first example deals with the path tracking reliability of the vehicle; the second example examines the convergence and the speed of the off-line calibration followed by path tracking.

The examples illustrate that for non-linear systems in noisy environments the use of stochastic state-estimators is needed. Moreover the Sigma-point approach provides more accurate estimation results than the commonly used non-linear EKF state estimators.

The symmetry preserving observers for non-linear systems benefit from their constructive design method, which provides local asymptotic convergence. This method can be utilized by non-linear applications in which the physical and mechanical symmetry properties of the system can be exploited.

REFERENCES

[1] BAR-SHALOM Y., LI X.-R., KIRUBARAJAN T.: Estimation with Applications to Tracking and Navigationm, Wiley Interscience, New York, NY, U.S.A., *2001*

[2] SÄRKKÄ S.: Recursive Bayesian inference on stochastic differential equations, PhD Thesis, Helsinki University of Technology, Helsinki, Finland, *2006*

[3] JULIER S.J., UHLMANN J.K.: Unscented filtering and non-linear estimation, Proc. IEEE, *2004*, 92(3), 401–422

[4] VAN DER MERWE R., WAN E.A., JULIER S.: Sigma-Point KALMAN Filters for Nonlinear Estimation and Sensor-Fusion: Applications to Integrated Navigation, Proc. AIAA Guidance, Navigation & Control Conference (GNC), Providence, RI, U.S.A. *2004*

[5] VAN DER MERWE R.: Sigma-Point KALMAN Filters for Probabilistic Inference in Dynamic State-Space Models, PhD Thesis, Oregon Health & Science University, Eugene, OR, U.S.A., *2004*

[6] JULIER S.J., UHLMANN J.K.: Corrections to unscented filtering and non-linear estimation, Proc. IEEE, *2004*, 92(12), 1958–1958

[7] JULIER S.J., UHLMANN J.K.: Unscented filtering and non-linear estimation, Proc. IEEE, *2004*, 92(3), 401–422

[8] WAN E.A., VAN DER MERWE R.: The unscented KALMAN filter, in KALMAN Filtering and Neural Networks, Ed.: HAYKIN S., John Wiley and Sons, New York, NY, U.S.A., *2001*, Chapter 7

[9] NORGAARD M., POULSEN N., RAVN O.: Advances in Derivative-Free State Estimation for Non-linear Systems Tech. Rep. IMM-REP-1998-15, Dept. Math. Modelling, Technical University of Denmark, Lyngby, Denmark, *2000*

[10] NORGAARD M., POULSEN N., RAVN O.: New Developments in State Estimation for Nonlinear Systems, Automatica *2000*, 36(11), 1627–1638

[11] ITO K., XIONG K.: Gaussian Filters for Nonlinear Filtering Problems, IEEE Trans. Automatic Control *2000*, 45(5), 910–927

[12] VAN DER MERWE R., WAN E.: Efficient Derivative-Free KALMAN Filters for Online Learning, Proc. 9th Eur. Symp. Artificial Neural Networks (ESANN) Bruges, Belgium, *2001*, 205–210

[13] VAN DER MERWE R., WAN E.: The Square-Root Unscented KALMAN Filter for State- and Parameter-Estimation, Proc. IEEE Int. Conf. Acoustics, Speech, and Signal Processing (ICASSP), Salt Lake City, UT, *2001*, 6, 3461–3464

[14] SALAM ERAN: Filtering Algorithms and Avionics Systems for Unmanned Aerial Vehicles, PhD Thesis, MINES ParisTech, Paris, France, *2010*

[15] BONNABEL S., MARTIN P., ROUCHON P.: Non-linear Symmetry Preserving Observers on LIE-Groups, IEEE Transactions on Automatic Control, *2009*, 54(7), 1709-1713

[16] BONNABEL S., MARTIN P., ROUCHON P.: Symmetry-preserving Observers, IEEE Transactions on Automatic Control, *2008*, 53(11), 2514–2526

[17] BONNABEL S., MARTIN P., ROUCHON P.: A non-linear symmetry-preserving observer for velocity aided inertial navigation, Proc. 2006 American Control Conference, Minneapolis, MN, U.S.A., *2006*

[18] AYHANMAN N., ROUCHON P.: On invariant asymptotic observers, CDC, *2002*

[19] ROUCHON P., GUILLAUME D.: Observation and Control of Simplified Car, IFAC, *1998*

[20] BONNABEL S.: Symmetries in observer design: review of some recent results and application to EKF-based SLAM, Robot Motion and Control 2011, Lecture Notes in Control and Information Sciences *2012*, 422, 3–15

[21] COLLON C., RUDOLPH J., WOITTENNEK F.: Invariant Feedback Design for Control Systems with Lie-symmetries – a kinematic car example, Discrete Cont. Dyn. Sys. *2011*, 2(11), 312–321

HUNGARIAN JOURNAL
OF INDUSTRY AND CHEMISTRY
VESZPRÉM
Vol. 42(2) pp. 65–70 (2014)

TELEMEDICAL HEART RATE MEASUREMENTS FOR LIFESTYLE COUNSELLING

MARIO SALAI,✉ GERGELY TUBOLY, ISTVÁN VASSÁNYI, AND ISTVÁN KÓSA

Faculty of Information Technology, University of Pannonia, Egyetem u. 10.,Veszprém, 8200, HUNGARY
✉Email: mario.salai@gmail.com

In this paper we analyse a low-cost commercial chest belt to be integrated into a lifestyle counselling system as a source of heart rate data. We compared data from a Schiller ECG Holter device, which serves as a reference to a CardioSport device. Due to missing data in the CardioSport device caused by loss of contact with the body, the creation of special algorithms was necessary for synchronization and data validation. The results show that when using our synchronization algorithms the average absolute percentage error between the two signals was 2% with correlation of more than 99%. Using a data validation algorithm, we were able to get on average more than 70% of the signal with an absolute percentage error of 3% and a high average correlation of 99%. The mean RR interval values and standard deviation of RR intervals are very close to those of the reference device using both the synchronization and data validation algorithms. When using the data validation algorithm, the reference measurements produced only slightly better results with regard to false detections of atrial defibrillation than the CardioSport device. In conclusion, we found that with a simple pre-processing algorithm, CardioSport as a low-cost device can be safely integrated into a lifestyle support system as a telemedical solution.

Keywords: telemedicine, lifestyle counselling, heart rate monitor

Introduction

Low-cost telemedical sensors are often used in modern ambient assisted living (AAL) telemonitoring and self-management systems for providing inputs to medical intelligence algorithms [1]. Such systems extend the scope of traditional health care that is based purely on data measurement. However, the proper interpretation and reliability of the results depends on the reliability of the measured data and the sensor itself. Nevertheless, there are still surprisingly few reviews reported in the literature to date on the validation of the information content of such low-cost sensors compared to the clinically accepted reference device. An example of a device that was tested for validity is the SenseWear HR Armband [2]. In this study, they used the reference device simultaneously with the tested device as a way of validating data. However, most of the compared devices are expensive high-end devices, which present an obstacle for their wide use in telemedicine.

In this proof-of-concept paper, we analyse a simple commercial chest belt chosen to be integrated into the Lavinia lifestyle mirror system [3] as a source of heart rate (HR) data. In the Lavinia system, the HR signal of the patient will be used to (i) estimate the calories burnt by physical activity, (ii) calculate the heart rate variability (HRV) in order to detect periods of mental or emotional stress, and (iii) analyse arrhythmia patterns (Poincare plots) for atrial fibrillation detection. Our approach involves the comparison of the HRV and Poincare plots computed from the filtered chest belt signal, with those parameters computed from a reference Holter device.

Methods

Measurements

Two devices were used simultaneously by a healthy volunteer over a 24 hour period. A Schiller MT-101/MT-200 Holter device was our reference device designed for clinical use. The chest belt was a CardioSport TP3 Heart Rate Transmitter device. Since this device does not have its own memory for storing data, we used a Nexus 7 tablet with Android version 4.4.2 to connect the device via the Bluetooth 4.0 protocol and store the measured data on the tablet.

Although both devices were worn by volunteers for 24 hours, only 12 hours of the overall signal were used for analysis due to frequent detachments of the device from the body during nighttime. The measurements of 12 hours were repeated on 4 additional healthy male subjects.

Signal Analysis

The direct comparison of measured data was not possible due to the different designs of the reference and the telemedical devices. However, we wanted to

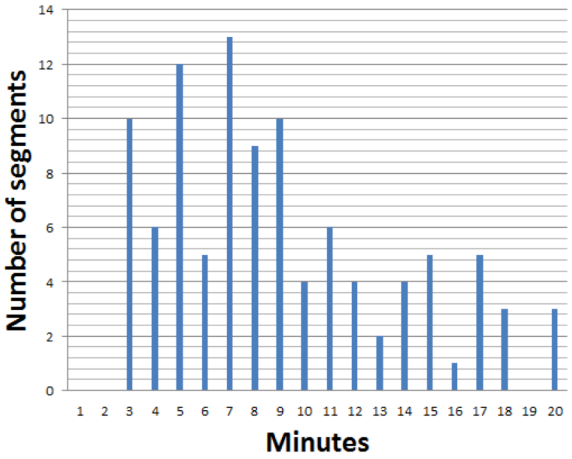

Figure 1: The distribution of strongly correlated segment lengths for all subjects

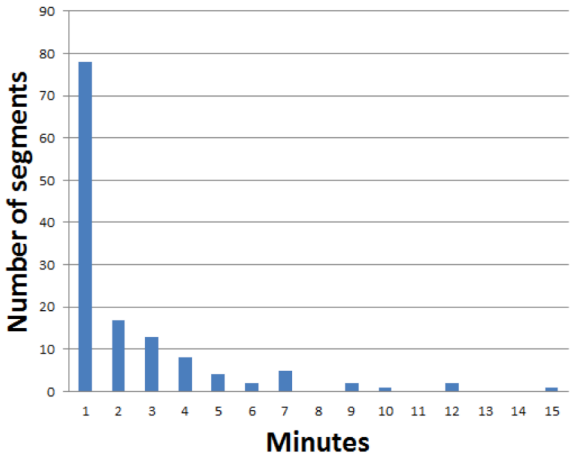

Figure 2: The distribution of weakly correlated segment lengths for all subjects

compare signals directly in terms of time and also to develop a data validation algorithm for removing the noisy parts of the CardioSport device measurements reliably without using the reference data. The problem was that the chest belt was not firmly attached to the body and sudden movements of the device caused signal loss. Therefore, we needed to create a software module for synchronization and data validation before any analysis. Data validation means removing obviously bad data (artefacts) and keeping only 'good' data segments of sufficient length, because, as a rule of thumb, both HRV and Poincare plot computations require data chunks of at least 5 minutes. Even though the data validation algorithm removed a considerable amount of data from the original signal, we still had enough useful data for analysis from the daytime.

The Synchronization Algorithm

Our simple algorithm for signal synchronization uses a sliding window that passes from the beginning of the chest belt signal to the end and calculates the absolute error between the two signals. When sliding finishes, the location of the sliding window with the minimum absolute error is considered as the point where the two signals should be synchronized. This applies only if the correlation of the data in the sliding window and the same amount of data from the reference device are higher than a minimum set by the user. If these conditions are met, the algorithm copies data from the sliding window into a newly generated third signal, which represents the chest belt signal fully synchronized with the reference signal. If conditions are not met, the third signal is filled with zeros. Finally, the algorithm extracts all the highly correlated segments from the third signal ignoring zero values. Also, a file with all the merged segments is generated for general analysis. The algorithm uses the following 5 main parameters that can be set up by the user:

1. window size: amount of data copied from the signal into the sliding window (default: 200),
2. window shift step: the number of samples by which we shift the sliding window in each iteration (default: 50),
3. absolute error window: amount of data used for calculating the minimum absolute error (default: 200),
4. maximum error distance: the number of samples by which we shift the absolute error window in order to find the minimum absolute error (default: 1000),
5. minimum correlation: minimum correlation, expressed as a percentage, required for the two signals to consider data in the chest belt signal as accurate (default: 97%).

Each parameter's default value was determined empirically. After running the synchronization process, we obtained segments of highly correlated data. *Fig.1* shows the distribution of the lengths of signal segments. We can see that most segments are 3 to 18 minutes long. The longest highly correlated segment with the reference data is 110 minutes long. The default parameter settings minimize the number of overly short (< 5 min) segments. Most of the bad segments (*Fig.2*) are shorter than one minute, and only one bad segment was 60 minutes long.

Data Validation Algorithm

Another type of algorithm was used in the real telemedical scenario for finding good parts of the signal without relying on reference data. This implies finding gaps and abnormal values and omitting them. First, we compared the timestamp of each data point with the timestamp of the previous one. If the difference between the timestamps was longer than 3 seconds, we marked this as a 'gap'. The 3-second gap detection was enabled by the chest belt's buffering system that can tolerate short detachments of the device from the body. In the second step we identified abnormal values in the signal that were treated as gaps. The abnormal values are identified by observing the mean value of 20 neighbouring data points (10 before and 10 after a given point). If the mean value differs from the value of the

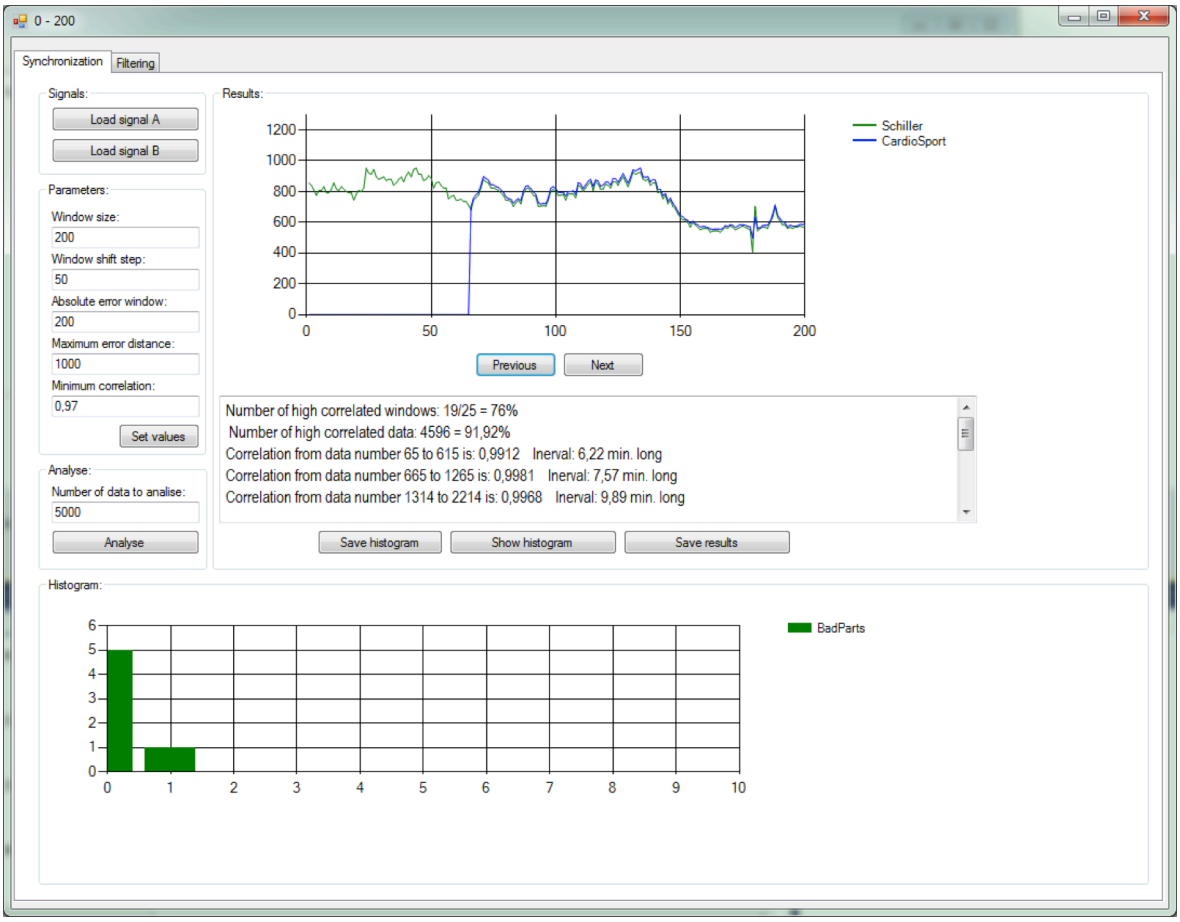

Figure 3: Synchronization and data validation software

current sample by more than 300 units, we consider it invalid and mark it as a gap/error in the signal. Finally, we extract the good segments from the signal with a length of more than 5 minutes.

We implemented the above algorithm in a simple software tool (*Fig.3*). On the left-hand side we can load the two signals and set the parameter values as well as the amount of data to be analysed. The graph shows two signals after the synchronization process was completed. The user can examine signals by clicking the Previous and Next buttons. General statistics are shown in the middle part of the screen, while in the lower part, we can see the histogram, and save the histogram and results as a file. Two tabs in the top left-hand corner allow the user to switch between synchronization and data validation algorithms.

Statistical Analysis

Time and frequency domain analyses, correlation comparisons, mean absolute percentage errors, and the slopes of scatter plot diagrams were compared between two measurements for HRV analysis. The specificities of a self-developed atrial fibrillation detector algorithm were compared for atrial fibrillation analysis. The latter algorithm is based on the k-means clustering of Poincaré plots (consisting of RR intervals)

The time and frequency domain analyses for HRV were performed using Kubios HRV analysis software,

Table 1: Signal duration after the synchronization process

Subject	Duration (h:m:s)
#1	10:53:28
#2	8:45:40
#3	10:30:17
#4	7:46:56

while the rest of the analysis for HRV and atrial fibrillation was performed in Microsoft Excel. Atrial fibrillation detection was done using the MATLAB environment and the results were saved as Microsoft Excel workbooks.

Results and Analysis

Heart Rate Variability

After the synchronization process, we got strongly correlated (greater than 97%) synchronized data segments of various durations. *Table 1* summarizes the duration of signals analysed.

Table 2 shows results in the time domain for Schiller and CardioSport devices after using the algorithm for the synchronization of signals. Time domain analysis shows similar values for mean RR values and standard deviation (STD RR in *Eq.(1)*). The average Mean RR values for the Schiller and CardioSport devices are 851 and 871 respectively. The average STD RR for the Schiller device is 108 and 110 for the CardioSport device.

Table 2: Time domain analysis after synchronization

Subject	Mean RR (ms) [a]		STD RR (ms) [b]	
	Schiller	CardioSport	Schiller	CardioSport
#1	738	755	123	125
#2	704	720	91	93
#3	908	929	90	93
#4	855	875	145	148
#5	937	959	107	109
Average	851	871	108	111

[a] with 2% error, [b] with 1-3% error

much less. Calculations show that in the worst scenario only 45% of the signal can be used for analysis using this data validation method, while in the best scenario this number reaches 95%. This leads to a conclusion that results are rather subject dependent.

The results of data analysis in the time domain after the removal of bad parts using the validation algorithm can be seen in *Table 5*. The mean RR intervals for Schiller and CardioSport devices are 851 and 871 and standard deviations are 104 and 106, respectively. The

Table 3: Frequency domain analysis after synchronization

Subject	Schiller Absolute power (ms^2)				CardioSport Absolute power (ms^2)				Error %			
	VLF	LF	HF	LF/HF	VLF	LF	HF	LF/HF	VLF	LF	HF	LF/HF
#1	7937.6	3086	1578	1.956	8444	3224	1330	2.4235	6	4	19	19
#2	5431.5	626.6	245	2.557	5723	659.3	250.9	2.6281	5	5	2	3
#3	4251.2	1927	494.4	3.898	4543	2055	538.8	3.8146	6	6	8	2
#4	12682	1790	636.5	2.813	13514	1869	621.5	3.0077	6	4	2	6
#5	6139.8	1212	476.7	2.542	6465	1274	481.4	2.6459	5	5	1	4

Table 4: Signal duration after data validation

Subject	Duration (h:m:s)
#1	1:28:10
#2	11:20:03
#3	6:15:38
#4	9:27:07
#5	4:29:44

$$STD\ RR = \sqrt{\frac{1}{N-1}\sum_{j=1}^{N}(RR_j - \overline{RR})^2} \qquad (1)$$

The frequency domain analysis for the synchronization process is presented in *Table 3*. The absolute power was compared for very low frequencies (VLF: 0-0.04 Hz), low frequencies (LF: 0.04-0.15 Hz), high frequencies (HF: 0.15-0.4 Hz) and ratios between low frequencies and high frequencies (LF/HF). Results show no significant difference between Schiller and CardioSport device values. The average mean absolute percentage error (MAPE) between two signals is 2% with a high average correlation of close to 100%.

Using the data validation algorithm, we extracted data points from the collected signals. The duration of the resulting signal is shown in *Table 4*. It is important to note that due to the noise on Schiller device recordings, we had to remove noisy parts from the original signal. Therefore, even though the signal was recorded continuously for 12 hours, overall duration is

Table 5: Time-domain analysis after data validation

Subject	Mean RR (ms) [a]		STD RR (ms) [b]	
	Schiller	CardioSport	Schiller	CardioSport
#1	701	724	136	139
#2	700	717	91	93
#3	899	921	100	100
#4	846	866	139	142
#5	958	981	88	90
Average	851	871	105	106

[a] with 2% error, [b] with 0-2% error

CardioSport device has slightly greater values, but these are practically identical.

The frequency domain analysis for the data validation process is presented in *Table 6*. The absolute power was compared for very low frequencies (VLF: 0-0.04 Hz), low frequencies (LF: 0.04-0.15 Hz), high frequencies (HF: 0.15-0.4 Hz), and ratios between low frequencies and high frequencies (LF/HF). As in the synchronization process, the results show no significant difference between the Schiller and CardioSport device values.

The minimum, maximum and average percentage errors on whole signals were calculated using 5 minute long sliding windows with one minute long shift steps (*Table 7*). Only one subject had a high maximum error value of 34%. By visual examination, it was determined that the cause of such a high error was the artefact of the Schiller device. In spite of that, the average error remained low (2%).

Table 6: Frequency domain analysis after data validation

Subject	Schiller Absolute power (ms^2)				CardioSport Absolute power (ms^2)				Error %			
	VLF	LF	HF	LF/HF	VLF	LF	HF	LF/HF	VLF	LF	HF	LF/HF
#1	10414	2297	1171	1.96	10847	2442	1004	2.43	4	6	17	19
#2	5446	631	245	2.57	5718	654	245	2.67	5	3	1	4
#3	5163	1990	523	3.80	5424	2054	540	3.80	5	3	3	0
#4	11683	1769	616	2.87	12149	1831	594	3.08	4	3	4	7
#5	4356	1235	317	3.89	4522	1303	330	3.95	4	5	4	1

Table 7: The minimum, maximum and average percentage errors

Subject	Minimum error	Maximum error	Average error
#1	0.1%	3.5%	1.5%
#2	0.0%	7.7%	2.1%
#3	0.0%	33.9%	3.2%
#4	0.1%	6.7%	1.9%
#5	0.1%	5.1%	2.2%
Average	0.1%	13.4%	2.4%

Fig.4 represents a typical relationship between CardioSport and Schiller devices. All gradient values are close to 1. The lowest slope value is 0.98 while the highest value is 1.02. The average mean absolute percentage error (MAPE) between two signals was 3% with a strong average correlation of 99%.

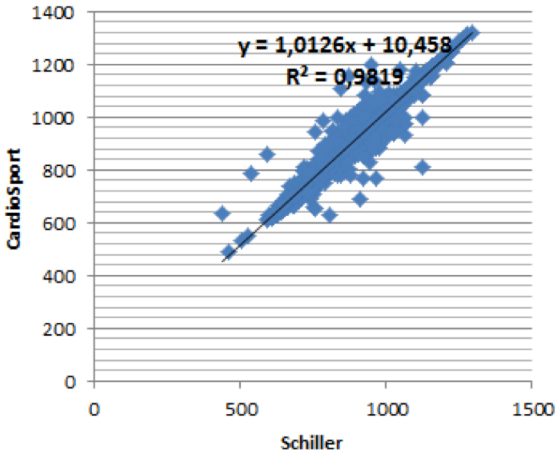

Figure 4: Comparison of the CardioSport and Schiller devices after data validation

Atrial Fibrillation

We carried out the detection of atrial fibrillation (AFib) by analysing POINCARÉ plots consisting of 30 RR intervals. We considered 30 RR intervals per iteration and in each iteration after constructing the POINCARÉ plot we calculated the dispersion around the diagonal line and used k-means based cluster analysis to determine the number of the clusters. If the dispersion was too high (greater than 0.06) and the number of clusters was 1, or the number of clusters was more than 9; we assigned "AFib" to that series of RR intervals, otherwise to "Non-AFib". The details of the algorithm can be seen in our previous study [16]. Since our data set did not contain real AFib cases, only specificity could be calculated with regard to the efficiency of detection. The evaluation of atrial fibrillation detection results for synchronized data validation can be seen in *Tables 8* and *9*.

Conclusion

Even though the CardioSport device may suffer from signal loss due to its design, we managed to determine that it can be safely used for telemedical purposes of measuring HRV and atrial fibrillation. We found only a few usable data segments that were less than 5 minutes long. With our algorithm that detects gaps and errors in

Table 8: Results from the synchronized data related to atrial fibrillation detection

Subject	Number of iterations	Schiller MT-101/MT-200 system				CardioSport TP3 Heart Rate Transmitter			
		AFib cases		Non-Afib cases		AFib cases		Non-Afib cases	
#1	331	26	8%	305	92%	31	9%	300	91%
#2	1796	9	1%	1787	99%	3	>1%	1793	~100%
#3	1120	7	1%	1113	99%	5	1%	1115	99%
#4	1427	11	1%	1416	99%	16	1%	1411	99%
#5	964	46	5%	918	95%	45	5	919	95%
Min	-	-	1%	-	92%	-	>1%	-	91%
Max	-	-	8%	-	99%	-	9%	-	~100%
Mean	-	-	3%	-	97%	-	3%	-	97%
STD	-	-	3%	-	3%	-	4%	-	4%

Table 9: Results from the data validation process related to atrial fibrillation detection

Patient	Number of iterations	Schiller MT-101/MT-200 system				CardioSport TP3 Heart Rate Transmitter			
		AFib cases		Non-Afib cases		AFib cases		Non-Afib cases	
#1	241	3	1%	238	99%	8	3%	233	97%
#2	1879	29	2%	1850	98%	2	>1%	1877	~100%
#3	808	15	2%	793	98%	3	>1%	805	~100%
#4	1296	10	1%	1286	99%	20	2%	1276	98%
#5	544	6	1%	538	99%	7	1%	537	99%
Min	-	-	1%	-	99%	-	>1%	-	97%
Max	-	-	2%	-	99%	-	3%	-	~100%
Mean	-	-	1%	-	99%	-	1%	-	99%
STD	-	-	>1%	-	>1%	-	1%	-	11%

the signal and removes them with an average effectiveness of more than 70%, which translates into having enough data to calculate HRV and atrial fibrillation from daytime measurements.

Regarding atrial fibrillation detection, we can conclude that by using the developed data validation algorithm the reference Schiller MT-101/MT-200 measurements produced only slightly better results with regard to false detections than the CardioSport TP3 Heart Rate Transmitter. In two cases the CardioSport measurements proved to be even better than Schiller records, which implies that some relatively simple heart rate recorders are equivalent to some Holter devices after signal processing using the data validation algorithm. We have to emphasize; however, that we have not performed any measurements on actual atrial fibrillating patients yet. Therefore, the investigation of the sensitivity of our atrial fibrillation detection algorithm under the presented circumstances could be the subject of further studies. In summary, the CardioSport as a low-cost device can easily be integrated into a lifestyle support system as a telemedical solution.

ACKNOWLEDGMENTS

This research was supported by the European Union and co-funded by the European Social Fund “Telemedicine-focused research activities in the field of Mathematics, Informatics and Medical Sciences” TÁMOP-4.2.2.A-11/1/KONV-2012-0073.

REFERENCES

[1] PATEL S., PARK H., BONATO P., CHAN L., RODGERS M.: A review of wearable sensors and systems with application in rehabilitation, J. Neuroengng. Rehab., *2012*, 9(21), 1–17

[2] KRISTIANSEN J., KORSHØJ M., SKOTTE J.H., JESPERSEN T., SØGAARD K., MORTENSEN O.S., HOLTERMANN A.: Comparison of two systems for long-term heart rate variability monitoring in free-living conditions - a pilot study, Biomed Eng. Online, *2011*, 10(27), 1–14

[3] KÓSA I., VASSÁNYI I., NEMES M., KÁLMÁNNÉ K.H., PINTÉR B., KOHUT L.: A fast, Android based dietary logging application to support the lifestyle change of cardio-metabolic patients, Global Telemedicine and eHealth Updates: Knowledge Resources, Eds.: M. JORDANOVA, F. LIEVENS, *2014*, 7, 553–556

[4] SALAI M., TUBOLY G., VASSANYI I., KOSA I.: Reliability of telemedical Heart Rate meters, IME J., *2014*, 8(5), 49–55

HUNGARIAN JOURNAL
OF INDUSTRY AND CHEMISTRY
VESZPRÉM
Vol. 42(2) pp. 71–77 (2014)

THE APPLICATION OF UNKNOWN INPUT ESTIMATORS TO DAMP LOAD OSCILLATIONS OF OVERHEAD CRANES

BÁLINT PATARTICS✉ AND BÁLINT KISS

Department of Control Engineering and Information Technology, Budapest University of Technology and Economics,
Magyar Tudósok krt. 2, Budapest, 1111, HUNGARY
✉E-mail: patarticsbalint@gmail.com

This paper focuses on the development of state estimation methods for mechanical systems with uncertain frictional parameters. The goal of the study is to provide reliable angle estimation for state-feedback-based crane control solutions, designed to reduce load sway. Cranes are underactuated systems, usually unequipped with the sensors necessary to measure the swinging angle, therefore the damping of their oscillatory behaviour is a challenging task. Two estimators are proposed for the calculation of the unmeasured states. One is based on an 'unknown input Kalman filter' (UIKF), the other applies the 'unscented Kalman filter' (UKF) with load prediction. Simulation results are provided to demonstrate the accuracy of the algorithms.

Keywords: overhead crane, state estimation, nonlinear systems, unknown inputs, Kalman filter

Introduction

The sway of the load carried by cranes is an unwanted phenomenon. Friction may decouple load motion from the remaining crane mechanism. This causes difficulty for inexperienced operators, especially when they try to land the cargo. The friction present in the crane mechanism makes the reduction of the swinging particularly demanding. Therefore the goal of the design of crane control systems is often to ensure minimal swinging along a specified trajectory [1–6].

There are numerous algorithms available in the literature for the solution to this problem. The design of such a control system can be addressed using soft computing methods such as fuzzy logic and neural network with genetic algorithm. These solutions require however the measurement of the load position, which is often based on workspace visualization [1]. Hard commuting techniques are also widely applied for sway reduction. An H_2 optimal solution is described in Ref.[2], which also relies on image processing for the measurement of the load coordinates. There are a variety of algorithms taking advantage of the flatness property (or exact linearizability) of overhead cranes [7]. The control systems in Refs.[3] and [4] consider all the states measurable, however an estimator is proposed in Ref.[3] for the computation of the uncertain parameters.

In the case of navy cranes, local asymptotic stability can be achieved without the measurement of the swinging angle, if trajectory planning exploits the flatness property of the system [6]. There is also a tracking control algorithm specifically designed for overhead cranes, that is capable of effectively reducing the sway despite the friction [5]. For the calculation of the unmeasured states, this controller uses a linear observer. In this paper we propose new methods of state observation for systems that take into account friction, and are applicable to overhead cranes. These estimators can replace the linear observer in Ref.[5] or the need to measure the load coordinates in any other state-feedback-based method to enhance the precision of the control. Our estimation methods are based on the assumption that the effect of the friction on the inputs can be reduced. This is true for most mechanical systems (including overhead cranes), where the actuating signals are usually forces and torques.

In the following section, the modelling of Lagrangian mechanical systems is overviewed, and it is shown how the friction can be handled as an input disturbance. In the next section the state estimation techniques are presented based on the possible approaches of interpreting the friction. The next section describes the results of the application of these methods to the state estimation problem of overhead cranes and presents the simulation results.

Lagrangian-Based Models of Mechanical Systems

The nonlinear dynamics of the controlled system can be obtained using the Euler-Lagrange equations. If the generalized coordinates are $q = \begin{pmatrix} q_1 & q_2 \dots q_n \end{pmatrix}^T$ and the generalized forces are $\tau = \begin{pmatrix} \tau_1 & \tau_2 \dots \tau_n \end{pmatrix}^T$, the Euler-Lagrange equations read

$$\frac{\mathrm{d}}{\mathrm{d}t}\frac{\partial \mathcal{L}}{\partial \dot{q}_i} - \frac{\partial \mathcal{L}}{\partial q_i} = \tau_i, \tag{1}$$

where $\mathcal{L}$ is the so-called Lagrangian, the difference between the kinetic and potential energy of the system, $\dot{q}_i = \frac{\mathrm{d}q_i}{\mathrm{d}t}$ and $i = 1, 2, \ldots n$.

Using these equations, under some conditions the controlled system's model can be written in the form

$$H(q)\ddot{q} + h(q, \dot{q}) + h_s(s) = \tau, \tag{2}$$

where $H(q)$ is the inertia matrix, $h(q, \dot{q})$ comprises the centrifugal, Coriolis and gravitational terms, and $h_s(s)$ is the frictional term with s being the vector of the frictional forces. In this form $h_s(s)$ can be reorganized to the right-hand-side of the equation. Introducing the disturbance torques as $\tilde{\tau} = \tau - h_s(s)$, *Eq.(2)* yields

$$H(q)\ddot{q} + h(q, \dot{q}) = \tilde{\tau}. \tag{3}$$

The state-space representation of the model is

$$\begin{aligned} \dot{x} &= f(x,\, u) \\ y &= g(x), \end{aligned} \tag{4}$$

where x is the state, u is the input, y is the output of the system, and f and g are nonlinear functions. This form can be obtained from *Eq.(5)* assuming that $x^T = \begin{pmatrix} q^T & \dot{q}^T \end{pmatrix}$, and the output is not directly dependent on the torques. The state-space equations read

$$\begin{aligned} \dot{x} &= \begin{pmatrix} \dot{q} \\ -H^{-1}(q)h(q, \dot{q}) \end{pmatrix} + \begin{pmatrix} 0 \\ H^{-1}(q) \end{pmatrix} \tilde{\tau} \\ y &= g(x). \end{aligned} \tag{5}$$

The inputs of mechanical systems are usually forces and torques, consequently they are only dependent on $\tilde{\tau}$. This means, that the effect of the friction can be reduced to the actuated degrees of freedom of the system.

If it is necessary for the design of the control system, the nonlinear dynamics can be approximated by a first order Taylor series expansion around a setpoint $(x_0,\, u_0)$. The linear model then becomes

$$\begin{aligned} \delta\dot{x} &= A\delta x + B\delta u \\ \delta y &= C\delta x, \end{aligned} \tag{6}$$

where the quantities prefixed with δ mean the distance from the setpoint, e.g. $\delta x = x - x_0$, and the matrices are Jacobians [8].

State Estimation Methods

Since the friction can be interpreted in our setup as an input disturbance, we consider two ways for its compensation in the state estimation. Either all input variables can be disregarded, or the additive disturbance can be estimated using a load predictor. These ideas form the basis of the two estimator design techniques described as follows.

The computations of the controllers implemented in embedded systems are based on sampled signals. Hence the design of the estimators is done in discrete-time.

Unknown Input Approach

Consider the discrete-time linear stochastic system model

$$\begin{aligned} x[k+1] &= \Phi x[k] + \Gamma_d d[k] + \omega[k] \\ z[k] &= Cx[k] + v[k], \end{aligned} \tag{7}$$

where x is the state, d is the unknown input (disturbance) of the system and z is the measurement of the output $y[k] = Cx[k]$. Φ and Γ_d are obtained from the matrices of *Eq.(6)* in the form of

$$\Phi = e^{AT_s}, \quad \Gamma_d = \int_0^{T_s} e^{At} B \,\mathrm{d}t, \tag{8}$$

where T_s is the sample time. The measurement and process noise v and ω are assumed to be additive, white, and Gaussian with mean of zero. Notice, that in *Eq.(7)*, all of the system inputs are considered to be disturbances.

The state and the unknown input of such a system can be estimated using an 'unknown input Kalman filter' (UIKF) [9], if the system satisfies the conditions

$$\dim\{d\} \leq \dim\{y\} \tag{9}$$

$$\mathrm{rank}\{C\} = \dim\{y\} \tag{10}$$

$$\mathrm{rank}\{\Gamma_d\} = \dim\{d\} \tag{11}$$

$$\mathrm{rank}\{C\Gamma_d\} = \dim\{d\}\,. \tag{12}$$

Additive Disturbance Approach

In the case of input disturbances, load prediction is often applied. Let us introduce the discrete-time nonlinear model of a system in the form

$$\begin{aligned} x[k+1] &= \phi(x[k],\, \tilde{u}[k]) + \omega[k] \\ z[k] &= g(x[k]) + v[k], \end{aligned} \tag{13}$$

where $\tilde{u}$ is the disturbed input of the system, and ϕ and g are nonlinear functions. We will follow the assumption, that the disturbance is additive to the input, thus $\tilde{u}[k] = u[k] + \Lambda d[k]$, where u is the vector of actuating signals, and Λ is a constant matrix.

We also assume a constant disturbance model with process noise ω_d, $d[k+1] = d[k] + \omega_d[k]$, resulting in the model

$$\begin{aligned} \tilde{x}[k+1] &= \tilde{\phi}(\tilde{x}[k], u[k]) + \tilde{\omega}[k] \\ z[k] &= \tilde{g}(\tilde{x}[k]) + v[k]. \end{aligned} \tag{14}$$

In *Eq.(14)* $\tilde{x}^T = \begin{pmatrix} x^T & d^T \end{pmatrix}$ is the extended state and $\tilde{\omega}^T = \begin{pmatrix} \omega^T & \omega_d^T \end{pmatrix}$ is the extended process noise. The extended nonlinear mappings of the system are given by $\tilde{g}(\tilde{x}[k]) = g(x[k])$ and

$$\tilde{\phi}(\tilde{x}[k],\, u[k]) = \begin{pmatrix} \phi(x[k],\, u[k] + \Lambda d[k]) \\ d[k] \end{pmatrix}. \tag{15}$$

In most cases the continuous-time differential equation of the observed system is available, in the form

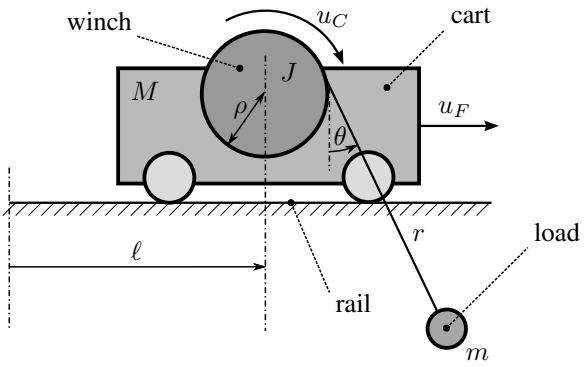

Figure 1: The two-dimensional ovearhead crane

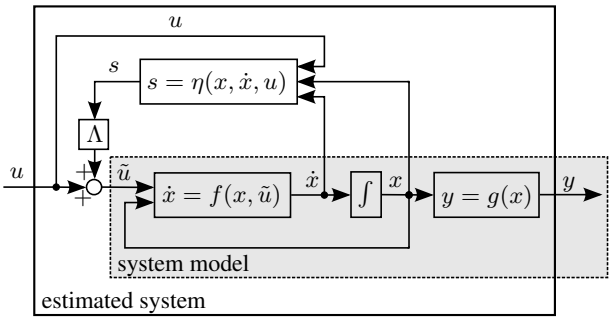

Figure 2: Dynamics of the estimated system

of *Eq.(4)*. The discrete-time state-transition equation can then be obtained by

$$\phi(x[k],\, u[k]) = x[k] + \int_{kT_s}^{(k+1)T_s} f(x,\, u[k])\,\mathrm{d}t, \qquad (16)$$

where the input is piecewise constant and $u[k] = u(kT_s)$. If the integral in *Eq.(16)* cannot be given in closed form and T_s is sufficiently small, the left rectangle rule approximation

$$\int_{kT_s}^{(k+1)T_s} f(x,\, u[k])\,\mathrm{d}t \approx T_s f(x[k],\, u[k]). \qquad (17)$$

can be used. Substituting this into *Eq.(15)*, the expression reads

$$\tilde{\phi}(\tilde{x}[k], u[k]) = \begin{pmatrix} x[k] + T_s f(x[k],\, u[k] + \Lambda d[k]) \\ d[k] \end{pmatrix}. \qquad (18)$$

For the observation of the system described by *Eq.(14)* and *Eq.(18)* the 'unscented Kalman filter' (UKF) [10] is applicable. We chose one of the implementation variants of this filter from Ref.[10].

Application of the Methods to Overhead Cranes

System Dynamics

We will now consider the state estimation problem of the two-dimensional overhead crane (*Fig.1*). Let us denote the horizontal displacement of the cart by ℓ, the length of the rope by r and the angle between the vertical and the rope by θ. The generalized coordinates of the system are chosen to be $q = \begin{pmatrix} \ell & r & \theta \end{pmatrix}^T$, and the state is $x = \begin{pmatrix} \ell & r & \theta & \dot{\ell} & \dot{r} & \dot{\theta} \end{pmatrix}^T$. Based on the sensors available, the output is $y = \begin{pmatrix} \ell & r & \dot{\ell} & \dot{r} \end{pmatrix}^T$.

Overhead cranes is a typical example of underactuated systems. It is actuated by two motors, one applying the force u_F on the cart, and another delivering the torque u_C to the winch. The system input consists of these, $u = \begin{pmatrix} u_F & u_C \end{pmatrix}^T$.

The parameters of the system are the mass of the cart M, the mass of the load m, the moment of inertia of the winch J and the radius of the winch ρ. The acceleration in the gravitational field is denoted by g.

The following assumptions are made of the system.

- The rope connecting the load to the winch is massless and behaves as a rigid rod during the motion.
- The load is a point mass.
- M, m, J and ρ are known.
- In the initial state of the system the unmeasured states are zero: $\theta = 0$ rad and $\dot{\theta} = 0$ rad/s.
- The effect of the aerodynamic resistance is negligible.

The Lagrangian of overhead cranes reads

$$\begin{aligned}\mathcal{L} =& \frac{1}{2}(M+m)\,\dot{\ell}^2 + \frac{1}{2}\frac{J}{\rho^2}\dot{r}^2 + +\frac{1}{2}m\left(\dot{r}^2 + r^2\dot{\theta}^2\right) \\ &+ m\dot{l}\dot{r}\sin\theta + m\dot{l}r\dot{\theta}\cos\theta + mgr\cos\theta.\end{aligned} \qquad (19)$$

Using *Eq.(1)*, the model can be written in the form of *Eq.(2)*, where the expressions become

$$H(q) = \begin{pmatrix} \left(M + m\sin^2\theta\right) & m\sin\theta & 0 \\ m\sin\theta & \left(\frac{J}{\rho^2} + m\right) & 0 \\ \cos\theta & 0 & r \end{pmatrix}, \qquad (20)$$

$$h(q,\dot{q}) = -\begin{pmatrix} m(r\dot{\theta}^2 + g\cos\theta)\sin\theta \\ mr\dot{\theta}^2 + mg\cos\theta \\ -2\dot{r}\dot{\theta} - g\sin\theta \end{pmatrix}, \qquad (21)$$

$$h_s(s) = -\begin{pmatrix} s_F \\ s_C \\ 0 \end{pmatrix}, \qquad \tau = \begin{pmatrix} u_F \\ -\frac{u_C}{\rho} \\ 0 \end{pmatrix}, \qquad (22)$$

where s_F is the frictional force between the cart and the rail and s_C is the frictional force applied to the winch.

The continuous-time linear model of the crane is computed around the setpoint $x_0 = \begin{pmatrix} 0 & r_0 & 0 & 0 & 0 & 0 \end{pmatrix}^T$, $u_0 = \begin{pmatrix} 0 & mg\rho \end{pmatrix}^T$, and $s_F = s_C = 0$ is substituted

Table 1: Numeric values of the parameters

	Value	Unit
M	5	kg
m	0.05	kg
J	$3.802 \cdot 10^{-4}$	kg m^2
ρ	0.02	m
g	9.81	m s^{-2}
T_s	1	ms
r_0	0.47	m
ℓ_D	0.5	m

into *Eq.(5)*. The resulting Jacobians are

$$A = \begin{pmatrix} 0 & 0 & 0 & 1 & 0 & 0 \\ 0 & 0 & 0 & 0 & 1 & 0 \\ 0 & 0 & 0 & 0 & 0 & 1 \\ 0 & 0 & \frac{m}{M}g & 0 & 0 & 0 \\ 0 & 0 & 0 & 0 & 0 & 0 \\ 0 & 0 & -\frac{m+M}{Mr_0}g & 0 & 0 & 0 \end{pmatrix},$$

$$B = \begin{pmatrix} 0 & 0 \\ 0 & 0 \\ 0 & 0 \\ \frac{1}{M} & 0 \\ 0 & -\frac{\rho}{m\rho^2+J} \\ -\frac{1}{Mr_0} & 0 \end{pmatrix}, \tag{23}$$

$$C = \begin{pmatrix} 1 & 0 & 0 & 0 & 0 & 0 \\ 0 & 1 & 0 & 0 & 0 & 0 \\ 0 & 0 & 0 & 1 & 0 & 0 \\ 0 & 0 & 0 & 0 & 1 & 0 \end{pmatrix}.$$

Substituting *Eq.(22)*, the disturbance torque term in *Eq.(3)* reads

$$\tilde{\tau} = \begin{pmatrix} u_F + s_F \\ -\frac{1}{\rho}\left(u_C - \rho s_C\right) \\ 0 \end{pmatrix}. \tag{24}$$

Eq.(24) shows, that the disturbed input of the system can be introduced in the form $\tilde{u} = u + \Lambda s$, where

$$\Lambda = \begin{pmatrix} 1 & 0 \\ 0 & -\rho \end{pmatrix}. \tag{25}$$

The frictional forces usually depend on the actuating signals, state variables, and the derivative of the state as well. The general characteristics of the friction reads as $s = \eta(x, \dot{x}, u)$. The block diagram of the dynamics of the system is illustrated in *Fig.2*. Only the system model block is used for estimator design, which is *Eq.(5)* if the effect of the friction is disregarded, $h_s(s) = 0$.

Proposition 1. *The discrete-time linear crane model obtained from the matrices in Eq.(23) and using Eq.(8) satisfies the design conditions of the UIKF in Eq.(9-12).*

Proof. It is clear that $\dim\{y\} = 4$, $\dim\{d\} = 2$ and $\operatorname{rank}\{C\} = 4$, thus *Eq.(9)* and *(10)* are satisfied. Using *Eq.(8)* and the numerical values in *Table 1*,

$$\Gamma_d = 10^{-2}\begin{pmatrix} 0.0001 & 0 \\ 0 & -0.025 \\ -0.0002 & 0 \\ 0.2 & 0 \\ 0 & -49.975 \\ -0.4255 & 0 \end{pmatrix}, \tag{26}$$

$$C\Gamma_d = 10^{-2}\begin{pmatrix} 0.0001 & 0 \\ 0 & -0.025 \\ 0.2 & 0 \\ 0 & -49.975 \end{pmatrix}.$$

We obtain $\operatorname{rank}\{\Gamma_d\} = 2$ and $\operatorname{rank}\{C\Gamma_d\} = 2$, which are both equal to the number of unknown inputs. This satisfies *Eqs.(11)* and *(12)*. The continuity argument holds for the rank of the matrices in *Eq.(26)*, therefore there exists a neighbourhood around our parameter set where the design conditions are still satisfied.

Simulation

The estimation results were obtained by simulation of overhead cranes in a closed-loop scenario using a simple discrete-time pole-placement-based linear controller. The simulation also took into account friction. There are various models of the friction phenomenon, ours included Coulomb, Stribeck, viscous friction, and stiction [11]. The numerical values of the parameters used in the simulation are given in *Table 1*.

Because of friction, but mainly stiction, the position of the crane can not be accurately controlled without integrators in the controller. Consequently we included the integral of the measurable positions in the controller design as proposed on page 309 of Ref. [8].

The outputs to be integrated are $y_I = \begin{pmatrix} \ell & r \end{pmatrix}^T$. Integrals of these quantities are approximated by the left rectangle rule as

$$x_I[k+1] = x_I[k] + T_s y_I[k] = x_I[k] + T_s C_I x[k], \tag{27}$$

where C_I is defined so that $y_I[k] = C_I x[k]$. In our case C_I is the first two rows of C in *Eq.(23)*. Using *Eq.(27)* and *Eq.(7)* a new system model is introduced in the form

$$\begin{aligned} \tilde{x}[k+1] &= \tilde{\Phi}\tilde{x}[k] + \tilde{\Gamma}u[k] \\ y[k] &= \tilde{C}\tilde{x}[k]. \end{aligned} \tag{28}$$

where the expanded state is $\tilde{x}^T = \begin{pmatrix} x^T & x_I^T \end{pmatrix}$ and the matrices are

$$\tilde{\Phi} = \begin{pmatrix} \Phi & 0 \\ T_s C_I & I \end{pmatrix}, \quad \tilde{\Gamma} = \begin{pmatrix} \Gamma_d \\ 0 \end{pmatrix}, \quad \text{and} \quad \tilde{C} = \begin{pmatrix} C & 0 \end{pmatrix}. \tag{29}$$

For the controller design the process and measurement noises are omitted.

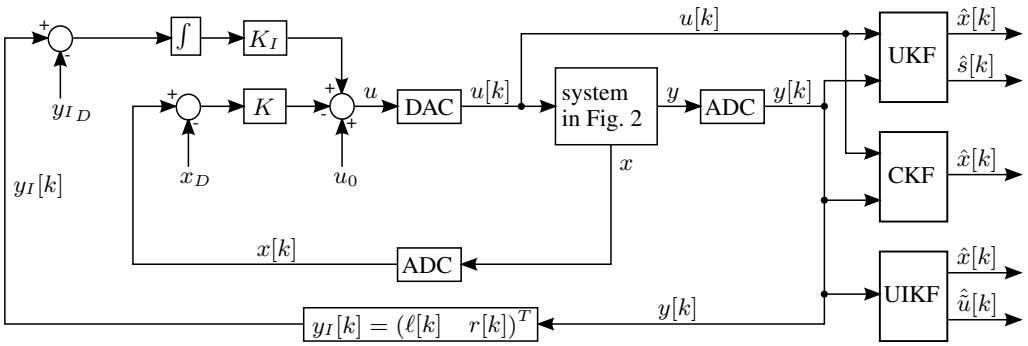

Figure 3: Closed-loop estimation setup used in the simulation

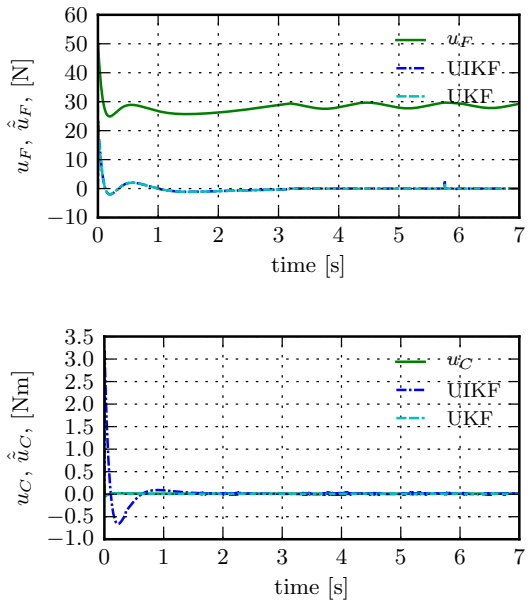

Figure 4: Actuating signals and the estimated inputs of the system

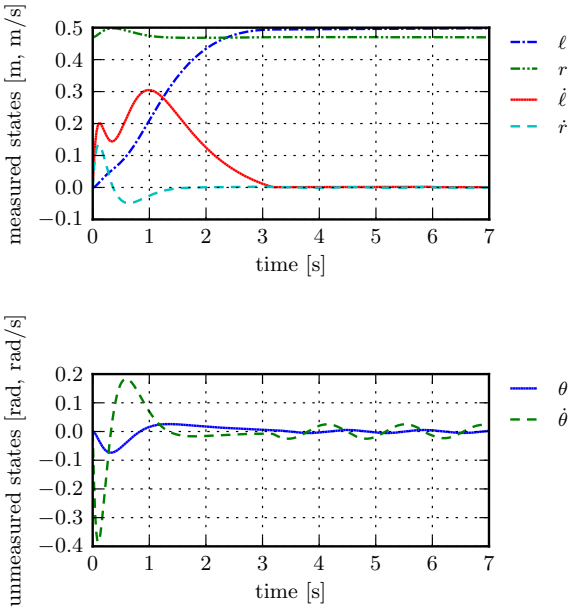

Figure 5: State evolution of the controlled crane using the true states as feedback

We want the state-feedback controller to output $u[k] = -\tilde{K}\tilde{x}[k] = -Kx[k] - K_I x_I[k]$. The gain $\tilde{K}$ can be computed using the eigenvalue placement method implemented in Matlab's `place` algorithm: $\tilde{K} = \texttt{place}(\tilde{\Phi}, \tilde{\Gamma}, \lambda)$, where λ contains the chosen eigenvalues of the closed-loop system. In continuous time they are $-1 + 0.5j$, $-1 - 0.5j$, -5.1, -5.2, -5.3 -5.4, -5.5, and -5.6. The controller gains are

$$K = \begin{pmatrix} 100.594 & -0.1273 \\ 0.6011 & -1.6765 \\ -185.407 & 0.0458 \\ 81.4011 & -0.0558 \\ 0.0562 & -0.3166 \\ -4.2257 & -0.0195 \end{pmatrix}^T, \quad \text{and} \tag{30}$$

$$K_I = \begin{pmatrix} 46.641 & 1.6026 \\ -0.074 & -2.955 \end{pmatrix}.$$

The closed-loop setup is illustrated in *Fig.3*. Here the integration is done using the left rectangle rule, and the ADC and DAC blocks are analogue-digital and digital-analogue converters respectively. The DAC uses the zero-order hold method for signal reconstruction. The desired state of the system is $x_D = \begin{pmatrix} \ell_D & r_0 & 0 & 0 & 0 & 0 \end{pmatrix}^T$, ℓ_D is the desired position of the cart and $y_{I\,D} = C_I x_D$.

Since we only want to demonstrate the results of the state estimation, first the real states are fed back to the controller. To compare the accuracy of our methods to a traditional solution, the classical Kalman filter (CKF) [12] is also implemented. As a result, the Kalman filters compute the estimated state of the system $\hat{x}[k]$, and they also provide information about the input.

The UIKF estimates the friction loaded actuating signals directly, while the UKF estimates the frictional forces superposed to the actuating signals. The actuating signals along with the estimates of the real inputs provided by the filters can be seen in *Fig.4*. Here, the estimated input of the UKF is computed as $\hat{\tilde{u}} = u[k] + \Lambda\hat{s}[k]$.

Because of friction, the real inputs are estimated to be

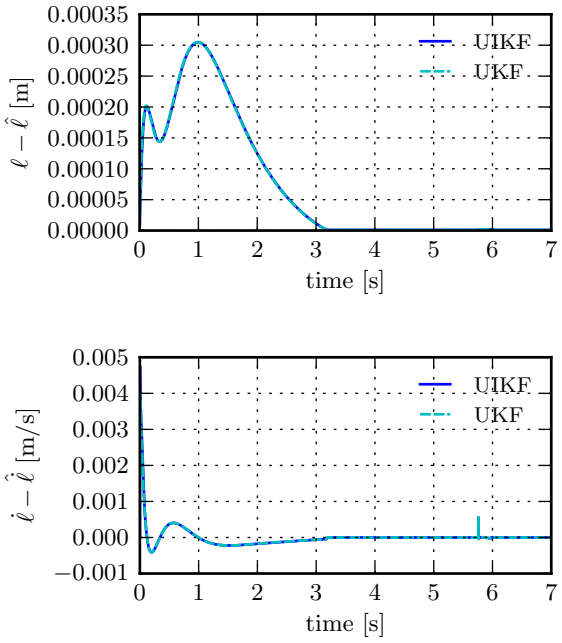

Figure 6: Error of the position and velocity estimations

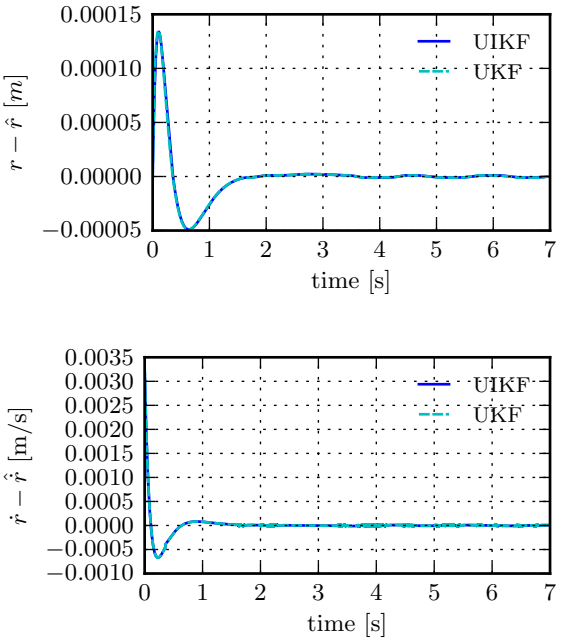

Figure 7: Error of the rope length and hoisting velocity estimations

much less than the actuating signals. The large offset in *Fig.4* is a consequence of the stiction, the cart will not move until u_F becomes greater than a certain value (in our case about 28 N). When the cart finally stops moving, the fluctuation of u_F tries to counter the load sway, during which the measured states do not change. This is the reason why the estimators find the input to be zero.

Fig.5 shows the transient of the states in a closed-loop. Results show that the controller can bring the system into the desired state, but friction prevents it from stopping the low amplitude swinging of the load, because it makes quick, short motions impossible. Error estimates are illustrated by *Figs. 6* and *7*. In all cases, the error becomes zero when the crane reaches the desired state.

This is not true for the angle and its derivative in *Fig.8*. The error decreases at the end of the state transient, but does not become zero. When the cart stops and the load swings, the measurements are all constant thus they carry no information regarding θ and $\dot{\theta}$. In these situations the cart and winch are usually also motionless due to friction. Consequently, the estimation error of these quantities never becomes zero.

It is possible to decrease the estimation error using two laser slot sensors. With the help of such devices, θ can be measured accurately in two positions and through the application of proper sensor fusion techniques the estimation of the angle can become more precise in between the chosen positions as well.

In *Fig.9* the estimation error of θ and $\dot{\theta}$ is illustrated using CKF. The filter was designed for the dynamics given by *Eq.(7)* except that it does not consider the inputs unknown. The results show that the error is substantially higher than in the case of the UIKF or UKF.

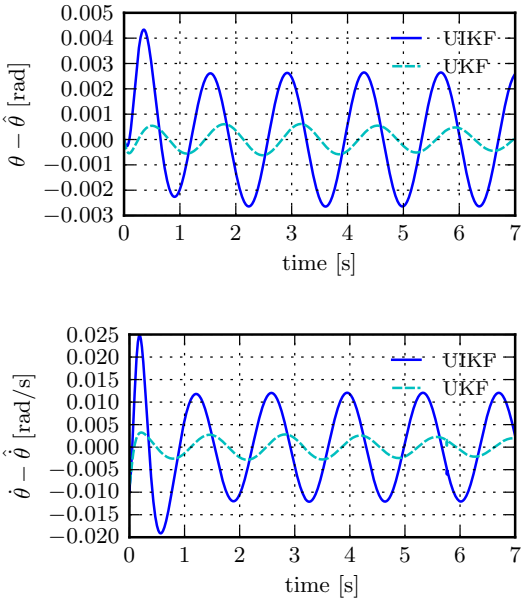

Figure 8: Error of the angle and angular velocity estimations

Fig.8 shows the estimation error of the UKF to be less. We applied this estimator in a closed-loop scenario identical to the one presented in *Fig.3*, but instead of $x[k]$ the $\hat{x}[k]$ of the UKF was used in the feedback loop. The state evolution of the crane in this simulation is illustrated in *Fig.10*. The system's behaviour is only slightly different from the case when the actual states were used in the feedback control in *Fig.5*.

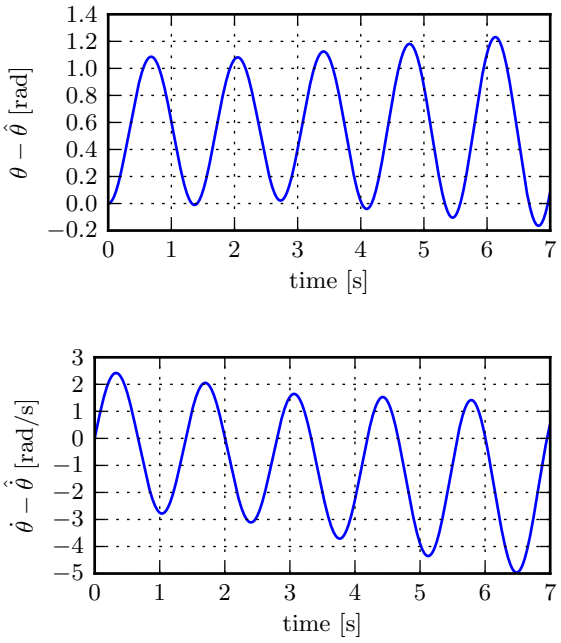

Figure 9: Error of the angle and angular velocity estimations using CKF

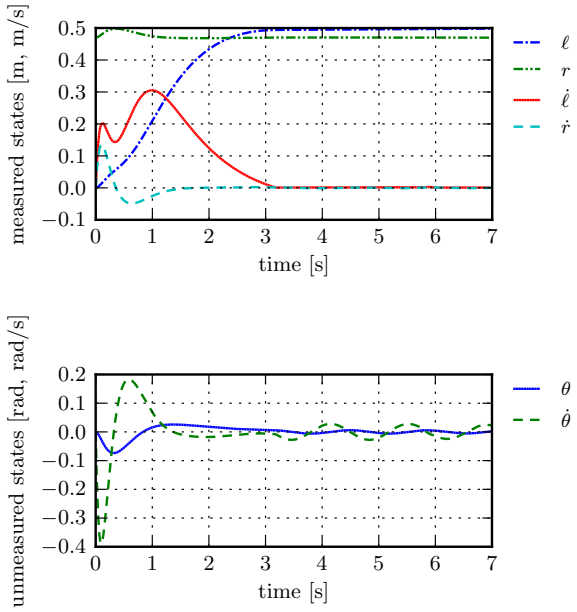

Figure 10: State evolution of the controlled crane using the UKF's estimated states as feedback

Conclusion

It was shown that in most mechanical systems the disturbing effect of friction can be reduced to the actuating signals. Based on this statement, two estimation methods were provided for the computation of the unmeasured states. One of these techniques considers the inputs completely unknown and uses UIKF for the estimation. The other algorithm treats the inputs as distorted by an additive disturbance, and applies UKF with a load predictor extension. Simulation results in a closed-loop controlled scenario were provided to prove the applicability of the concepts. It was also pointed out, that the precision of the estimators could be improved using laser slot sensors. This will be the subject of a forthcoming paper.

REFERENCES

[1] HYLA P.: The crane control systems: A survey, Proc. 17th Int. Conf. Methods and Models in Automation and Robotics (MMAR), *2012*, 505–509

[2] SCHINDELE D., MENN I., ASCHEMANN H.: Nonlinear optimal control of an overhead travelling crane, Proc. 18th IEEE Int. Conf. Control Applications, *2009*, 1045–1050

[3] BOUSTANY F., D'ANDREA NOVEL B.: Adaptive control of an overhead crane using dynamic feedback linearization and estimation design, Proc. IEEE Int. Con. Robotics and Automation, *1992*, 1963–1968

[4] NEUPERT J., HILDEBRANDT A., SAWODNY O., SCHNEIDER K.: Trajectory tracking for boom cranes using a flatness based approach, Proc. Int. Joint Conf. SICE-ICASE, *2006*, 1812–1816

[5] RÓZSA T., KISS B.: Tracking control for tow-dimensional overhead crane, Proc. 8th Int. Conf. Informatics in Control, Automation, and Robotics, ICINCO, *2011*, 1, 427–432

[6] KISS B., LEVINE J., MULLHAUPT P.: A simple output feedback PD controller for nonlinear cranes, Proc. 39th IEEE Conference on Decision and Control, *2000*, 5, 5097–5101

[7] KISS B., LÉVINE J., MÜLLHAUPT P.: Modelling, flatness and simulation of a class of cranes, Electrical Engineering, *1999*, 43, 215–225

[8] LANTOS B.: Theory and design of control systems I., Akadémia Kiadó, *2001* (in Hungarian)

[9] DAROUACH M., ZASADZINSKI M., ONANA A.B., NOWAKOWSKI S.: Kalman filtering with unknown inputs via optimal state estimation of singular systems, Int. J. Sys. Sci., *1995*, 26(10), 2015–2028

[10] HAYKIN S.S.: Kalman filtering and neural networks, John Wiley & Sons, Inc., *2001*

[11] ARMSTRONG-HÉLOUVRY B., DUPONT P., DE WIT C.C.: A survey of models, analysis tools and compensation methods for the control of machines with friction, Automatica, *1994*, 30, 1083–1138

[12] KALMAN R.E.: A new approach to linear filtering and prediction problems, Journal of basic Engineering, *1960*, 82, 35–45

HUNGARIAN JOURNAL OF INDUSTRY AND CHEMISTRY

HJIC

Advertise upcoming meetings,

conferences, workshops,

new products or services;

make public announcements,

introduce your research laboratory

on the pages of the

Hungarian Journal of Industry and Chemistry

Please contact us if interested!

EDITORIAL OFFICE: UNIVERSITY OF PANNONIA
P.O. BOX 158, VESZPRÉM H-8201 (HUNGARY)
Tel.: +36 (88) 624-746, E-mail: hjic@almos.uni-pannon.hu;
web: hjic.mk.uni-pannon.hu
Felelős szerkesztő: Szilágyi Róbert Károly, PhD
Kiadja: Pannon Egyetem, 8200 Veszprém, Egyetem u. 10.
Levélcím: H-8201 Veszprém, Postafiók 158, Tel.: (88) 624-000
Felelős kiadó: a Pannon Egyetem, Mérnöki Kar dékánja

HUNGARIAN JOURNAL
OF INDUSTRY AND CHEMISTRY
VESZPRÉM
Vol. 42(2) pp. 79–84 (2014)

CHALLENGES OF ENTERPRISE POLICY COMPLIANCE WITH SMARTPHONE ENABLEMENT OR AN ALTERNATIVE SOLUTION BASED ON BEHAVIOUR-BASED USER IDENTIFICATION

SÁNDOR DOBOS✉ AND ATTILA KOVÁCS

Department of Information Technology, ELTE University Budapest, Budapest, 1117, HUNGARY
✉Email: sandor.dobos@hu.ibm.com

Current trends show the intense growth in the role and importance of mobile technology (smartphones, tablets, etc.) in business due to economic, social and technological reasons. The social element drives a powerful convenience expectation called "Bring Your Own Device" (BYOD) for taking notes and accessing internal and external network resources. Apparently, the future is leading toward a more extensive enablement of smartphones and tablets with their enterprise applications. Internal security standards along with applicable regulatory ones to achieve 'policy enforcement' as types of solutions and controls; however, this allows for merely one aspect of compliance. An alternative solution could be behaviour-based analysis to identify the user, attacker or even a malicious program accessing resources on phone or internal networks. Complex networks can be defined by graphs, such as connections to resources on smartphones and serve as a blueprint. In case the motif is different from the user's actual behaviour, the company can initiate specific actions to avoid potential security violations. This document reviews the IT security challenges related to smartphones as well as the concept of graph-based user identification. The challenges of the latter are the identification of motif, selection of search algorithm and defining rules for what is considered a good or bad behaviour.

Keywords: mobile device security, "Bring Your Own Device" (BYOD) management, secure data communication, behaviour-based identification of threat, graph-based user identification

Introduction

Enterprise policy enforcement with current mobile technology management tools (Mobile Device Management (MDM), virus detection, and other necessary modules) ensure only the compliance of piece of equipment. Within enterprise, MDM Servers initiate the compliant actions, if the smartphone client fails the access privilege is taken away; however, this has an immediate impact on revenue through operational efficiency affecting the business. The enterprise compliance of the smartphone device is only a validated response, which can be altered by understanding the mobile technology, such as the application structures or the way MDM technology works. Hackers are heavily attacking smart devices with malicious software (Malware). These can be viruses, spyware, adware, and other types of attacks. A specific example is the "`Obad.a` Trojan", which is now being distributed *via* mobile botnets. The trojans are occupying a larger space and becoming more complex, which shows the need for IT security to find new ways to detect them.

The secure enterprise environment is crucial for organizations to ensure the business strategy and continuity of operation, irrespective of its environment being production, service delivery, or customer support related. Companies are following the trend to ensure efficiency and simplify service accessibility for their customers, business partners or employees. It is an essential element of the IT security strategy to be aligned with the business strategy due to (i) the intense growth of mobile technology and (ii) pressure from enterprise that has transformed business operations.

Forrester Research from the Q2 Foresights Security Survey shows (*Fig.1*) that mobile security is of primary concern amongst enterprise leaders. CEOs are concerned about the risk of data loss, particularly due to device loss or theft. Another worry regards data protection or data leak prevention usually in connection with data related to finance and innovation.

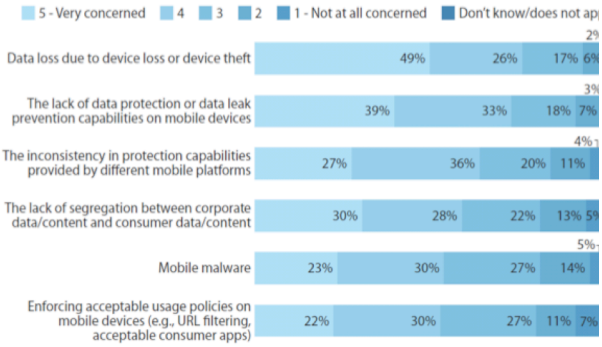

Figure 1: Degree of concern of CEOs from Forrester Research, Foresights Security Survey

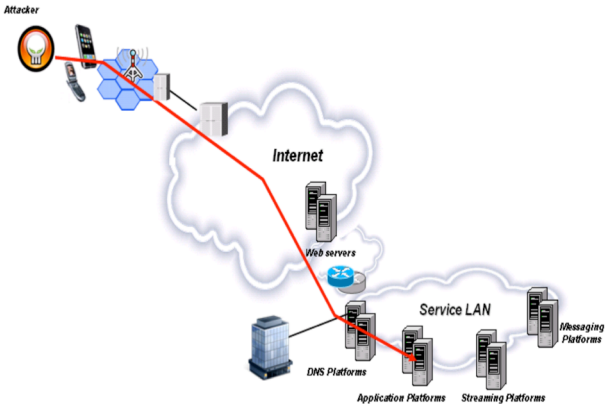

Figure 2: Graphical illustration of mobile phone technology security threats

Current Challenges

Within today's economic environment, profit-driven organizations are challenged from revenue, growth or profit target perspectives. In order to meet such expectations, organizations are under high pressure to offer innovative products (services) within newly identified channels and more accessible yet-to-be-penetrated markets to a demanding customer base, especially in the area of providing smartphone solutions. On the other hand, regulatory bodies are alarmed at mobile enablement and organizations in general striving to protect critical financial systems better, in particular via identity and access management. At the same time, organizations need to maintain operational resiliency and perform risk management assessments as an integrated part of day-to-day operations. The cost perspective is an important factor for customers facing the task of achieving a lower total cost of ownership (TCO) although, by this shift in paradigm, they move from reactive protection to proactive value creation mode.

The alignment of the current IT strategy to business strategy is a challenge for corporations as IT is a service provider within an enterprise also offering business enablement leads. Companies need to manage security policy at the corporate level, assess the security health of the heterogeneous IT environment, monitor the security weakness(es) in processes and systems and, of course, meet the plethora of banking laws, regulations and standards including SOX, BASEL III, GLBA, and PCI compliance.

With the adaptation of the BYOD concept in business practices, mobile technology itself contributes to additional and more complex challenges. Enterprises are not the owners of those smart devices with access to enterprise networks and their data. *Fig.2* illustrates how smartphones with applications developed by unknown sources could be a threat to enterprise's sensitive data.

Business Drivers for Change

As introduced above an active need is emerging for more effective mobile solutions. It is not only a reflection of the compliance requirements but a real protective solution against mobile threats without any restrictions on financial growth or cutbacks on efficiency initiatives. There are compelling reasons to act and change now including data potentially at risk, pressure from regulatory bodies and audit firms to be compliant with the applicable data handling regulations, and the implementation of mobile security into an existing security structure.

Highlights of a Political-Economic-Social-Technology (PEST) Analysis

Politicians are setting high standards for data management regardless of platforms, even if they are related to mobile devices or mobile applications. These regulations mostly focus on the handling of financial data such as The Sarbanes–Oxley Act of 2002 (SOX). There are new developments regarding data (pictures, text, etc.) ownership such as The Stop Online Privacy Act (SOPA). The Preventing Real Online Threats to Economic Creativity and Theft of Intellectual Property Act or in short PROTECT IP Act (PIPA) will have an even more rigorous norm for enterprises who need to meet these regulations in order to obtain permission to operate in a certain field or market (market player).

The economic situation puts more pressure on businesses as the trend still shows stagnancy on a macro level while in some segments it is still in decline. Firms have high demands for business achievements measured by revenue and profit perspectives to meet shareholder expectations. One way to do so is to improve cost structures with mobile enablement (particularly BYOD).

Society wants to live more comfortably by searching for easily accessible services, such as online mobile-enabled bank transfers or online mobile retail orders. Companies aim to reach their customers via mobile applications that are more easily accessible through user-friendly interfaces, such as social network platforms. As usual, this trend is typical for major market areas, such as North America or, Western Europe; however, other regions are expected to follow.

The trend in technology continues to be more vivid from a computing power and portability perspective. Internet Service Providers are granting access to higher bandwidth networks for new applications and online content.

Policy Enforcement and its Weaknesses

To manage the various types of mobile devices in an enterprise, a solution was introduced in 2008 by STRICKLEN, MCHALE, CAMINETSKY and REDDY based on Pattern Definition for Mobile Device Management (MDM). MDM is the most common approach how mobile devices (including smartphones, tablets) are managed within the enterprise as a management tool for monitoring and policy enforcement. Even though this technology is available and wide-spread, according to ABI research, mobile threats grew by 261% just in the

last quarter of 2012; however, MDM technology is not growing at a comparable rate to the number of vulnerabilities and attacks.

One of the components of MDM is the registration module, which is responsible for identifying mobile devices within the enterprise network, where the identifier indicates the platform of each mobile device, e.g. smartphone and tablet. The other significant element is the management module. Its job is to receive a management function definition performed on mobile devices using identifiers from mobile devices. The management module is responsible for instructions for the first platform to perform the management tasks and provides instructions for the other modules specific to the second platform to perform the management task on at least the second device.

However, MDM is not the ultimate solution for mobile device security within the enterprise environment due to some concerns regarding the verifiable device integrity. There are attempts at identifying MDM solutions to detect modifications of the underlying platform, but since the MDM agent has limited privileges and was susceptible to compromise by malicious privileged software, these stand little chance of detecting a targeted attack. The US National Security Agency (NSA) describes an immutable cryptography, as the 'root of trust' on a specific platform, to be available for leveraging by MDM or other software, providing a means of countering this type of threats. Encryption enables devices to attest their integrity on an enterprise and carry out any local policy decisions. The availability of this 'root of trust' to other software can vigorously complement a chain of trust that begins when booting and extends into the system runtime. An additional benefit of an immutable root of trust is that it allows a company to bind the unique identifier of that device together with other credentials to restrict company access to only those devices. In effect, the device itself can become one of the factors of a multi-factor access.

In summary, MDM's current capabilities support the BYOD and enterprise-owned use of mobile devices with certain gaps for high-security issues. Management capabilities are limited to those provided for MDM products by the underlying mobile OS (iOS, Android, and other platforms), and therefore, these capability gaps cannot be closed by MDM providers alone. On-going cooperation between enterprise customers, OS vendors, and MDM vendors is critical to the continued advancement of enterprise-level security for mobile devices. Closing stated holes will enable the deployment of commercially available mobile devices to tackle high-security use issues common in sensitive industrial and governmental environments.

Secure data networks need to guarantee integrity, confidentiality and availability; this is when security is fulfilled. Policy enforcement with the MDM can be too liberal, but then there is no real need for MDM or strictly constraining users thus limiting the value-add. The proposed solution is to identify the user based on behaviour and compare behaviour changes.

Behaviour Analysis and Challenges

Growing recognition drove the importance of network science related to the behaviour of sophisticated systems that is shaped by relations among their constituent elements. The rising availability and tractability of large and high quality data sets on a wide range of complex systems [1-3] have led to a primary insight: substantially diverse complex systems often share core key organizational principles. These can be quantitatively characterized by the same parameters, which means that they show remarkably similar macroscopic behaviour despite reflective differences in the low-level details of the components of each system or their mechanisms of interaction.

The behaviour as described above can be modelled by mathematical graphs, where the graphs are defined simply as a set of nodes called vertices linked together in direct or indirect ways by connections (edges). From a mathematical point of view, $G(V, E)$ are canonical graphs as the vertices and edges are labelled. In network science, methodological advances permit research to quantify other topological properties of complex systems, such as modularity [4], hierarchy [5], centrality [6] and the distribution of network hubs [7,8]. There have also been significant efforts to form the development or evolution of complex networks [9], to link network topology to network dynamics, and to explore network robustness and vulnerability. These topics are likely to become more relevant in relation to behavioural studies.

Structural and functional behaviour maps can be created using graph theory through the following four steps:

1. Define the network nodes.
2. Estimate a continuous measure of association between nodes.
3. Generate an association model by compiling all pairs of associations between nodes and usually apply a threshold to each element of this model to produce a binary adjacency matrix or undirected graph.
4. Calculate the network parameters of interest in this graphical model of the behaviour network and evaluate them against the equivalent parameters of a population of random networks.

The elements such as defined network nodes, relationship of nodes, generated association matrix and network parameters give the basis of the behaviour type of "blueprint" of a user. A mobile user can be defined as an identity based on certain features of this behavioural "blueprint" as the key points of a fingerprint within the enterprise company. In *Fig.3* the darker highlighted edges could be the essential elements for the identifier.

Access to resource driven networks is defined in the graph theory as a set of nodes or vertices and the edges or lines, plus the connections between them. The graph topology can be quantitatively captured by a wide variety of measures used to generate the key points of the blueprint. The most important measurement is the node degree. The degree of a node is the number of

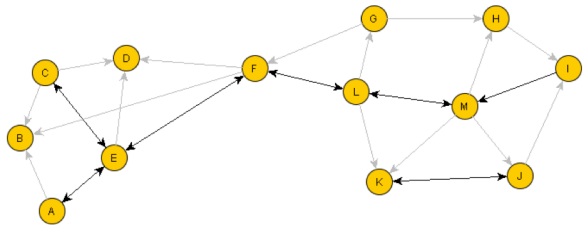

Figure 3: An example of a mobile user's identity on the basis of a "blueprint" network

connections it links to the rest of the network. Based on this definition, it is the most elementary network measure, and most other measures are ultimately linked to the node degree. The degrees of all the network's nodes identified form a degree distribution [10]. In randomly selected networks all of the connections are equally probable, i.e. the result is a Gaussian distribution. However, complex networks in general have non-Gaussian distributions, often with a long tail towards higher degrees. The degree distributions of the scale-free networks follow a power law [11]. This landmark study [11] was the first to describe the scale-free organization of many complex networks and proposed a simple growth rule for their formation.

The number of connections could give a large graph network that could be used for usability needs to define clustering, coefficients, and motifs. If the nearest neighbours of a node are also directly linked to each other, they form a cluster, and the clustering coefficient quantifies the number of connections that subsist between the nearest neighbours of a node as a quantity of the maximum number of possible connections [12]. The randomly selected networks exhibit low average clustering, whereas compound networks displays high clustering. Interactions between neighbouring nodes can also be counted by counting the occurrence of small motifs of interconnected nodes [13]. The distribution of different motif classes (nodes EFL and KMJ in *Fig.3*) in a network provides information about the types of local interactions that the network can support [14].

The numbers of reachable nodes and hops needed for connectivity are defined by the path length and efficiency. The path length is the minimum number of edges that must be passed through to start moving from one node to another. Random, complex networks have short mean path lengths; they exhibit high global efficiency of parallel information transfer, whereas regular patterns exhibit long mean path lengths. Efficiency is inversely related to path length. Nevertheless it is numerically easier to estimate topological distances between elements of disconnected graphs. Moreover, the link density or cost of the route provides further description. The connection density is the actual number of the network edges in the graph as a proportion of the total number of possible edges and is the simplest estimator of the physical cost of the network.

Hubs are nodes of high degree, where the centrality of a node measures how many of the shortest paths exist between all other node pairs in the network passing through it. It can be asserted that nodes with high centrality are thus crucial to efficient communication [15]. The importance of an individual node to network effectiveness can be assessed by deleting it and estimating the efficiency of the severed network. The robustness property refers either to the structural integrity of the network following the deletion of nodes, edges or effects of perturbations on local or global network states.

Finally, modularity is the property that has significant influence on the "blueprint" of the behaviour. There are algorithms that estimate the modularity of the network on the basis of hierarchical clustering [16]. Each module contains several densely interconnected nodes, and there are relatively few connections between these nodes in different modules. Airline hubs described this as a function of their roles in community structure [17]. Provincial hubs are connected mainly to nodes in their modules where the connector hubs are connected to nodes in other modules.

Graph Based Analysis of Smartphone Usage

Previously, the challenges of using mobile devices in the enterprise environment were discussed. It is important to identify the activities on the device in order to take either preventive or corrective actions. $G(V, E)$ used for the behaviour identification and description graphs. Vertices are defined as applications, more precisely, vertices within the device or network addresses and sites. Edges are the connections between the vertices applications called websites, network addresses, user- or process-initiated connections.

- Network nodes can be defined as the resource access, i.e. applications, programs, and device elements access initiated by the user or application calls.
- Association between network nodes could be defined as the connections of the applications (calls, connections, as web access), usually resources are connecting together.
- Based on the above elements, network nodes and associations provide the details to calculate the association matrix.
- The following steps include network parameter analysis calculated from the above.

The question is not whether mobile activity can be defined as a complex network and describable by graph, but whether the process identies a user by a motif. However, before this question can be answered certain challenges need to be faced:

- identify motifs as maximum independent set,
- search motif in the complex network,
- define „approved behaviours" according to the identification of user behaviour.

Identification of the Motif in the Graph

The task is to find the Maximum Independent Set (MIS) of a particular graph as was defined by GAREY and JOHNSON [18] as NP-complete and remains so even for bounded degree graphs. According to FEIGE *et al*. [19] MIS cannot be approximated even within a factor of $|V|^{1-o(1)}$ in polynomial time.

The greedy algorithm (GMIS) can provide a solution for the identification of the maximum independence set. The algorithm selects a vertex of minimum degree, deletes that vertex and all of its neighbours from the graph, and repeats this process until the graph becomes empty. A recent detailed analysis of the GMIS algorithm has shown that it produces reasonably good approximations of the MIS for bounded- and low-degree graphs defined by HALLDORSSON and RADHAKRISHNAN [20]. In particular, for a graph G with a maximum degree Δ and an average degree $\bar{d}$, the size $|I|$ of the MIS satisfies *Eq.(1)*.

$$|I| \leq \min\left(\frac{\Delta+2}{3}|\mathrm{GMIS}(G)|, \frac{\bar{d}+2}{2}|\mathrm{GMIS}(G)|\right) \quad (1)$$

where |GMIS(G)| is the size of the approximate MIS found by the GMIS algorithm.

Eq.(1) provides an upper-bound of the number of edge-disjoint embeddings of a particular sub-graph, and will use this bound to obtain a computationally tractable problem formulation that is guaranteed not to miss any sub-graphs that can potentially be frequent.

Searching for a Discover Motif in the Graph

The GROCHOW-KELLIS method [21] can be used to find all examples of sub-graphs of a given size, similar to exhaustive methods. In the background, all non-isomorphic graphs are generated of a particular size using MCKAY'S tools [22]. Then for each graph, the method evaluates its significance. Due to symmetries, a set sub-graph of G may be mapped to a set query graph H multiple times. Therefore, a simple mapping-based search for a query graph will locate every case of the query graph as many times as the graph has symmetries. To avoid this, the method computes and enforces several symmetry-breaking conditions, which ensure that there is an exclusive map from the query graph H for each case of H in G, so that the search only spends time finding each instance once

```
IsomorphicExtensions (f,H,G[,C(h)]:
Finds all isomorphic extensions of partial map f :
   H → G [satisfying C(h)]
Start with an empty list of isomorphism.
Let D be the domain of f.
If D=H, return a list consisting solely of f.
   (Or write to disk.)
Let m be the most constrained neighbour of any d ∈ D
   (constrained by degree, neighbours mapped)
For each neighbour n of f (D)
If there is a neighbour d ∈ D of m such that n is not
   neighbours with f(d),
or if there is a non-neighbour d ∈ D of m such that n
   is neighbours with f(d)
[or if assigning f (m)=n would violate a symmetry-
   breaking condition in C (h)],
then continue with the next n.
Otherwise, let f=f on D, and f (m)=n.
Find all isomorphic extensions of f.
Append these maps to the list of isomorphism.
Return the list of isomorphism
```

The symmetries of a graph H equals automorphism (self-isomorphism). The collection of automorphism of H is indicated by $Aut(H)$. For a set A of automorphism, two nodes are stated to be "A-equivalent" if there is some automorphism in A which maps one to the other, or just "equivalent" if A $=Aut(H)$. Given a set of conditions C, α preserves the conditions C if, given a labelling L1 of H which satisfies C, the corresponding labelling L2: $H \rightarrow Z$ given by $L2(n) = L1(\alpha(n))$ also satisfies C. We are thus searching for setting C, such that the only automorphism preserving C is the identity. This ensures exactly one map from H onto each of its instances in G to satisfy the conditions. To find these conditions, an $Aut(H)$-equivalence class $\{n_0, ..., n_k\}$ of nodes of H, and the condition $L(n_0) < \min(L(n_1), ..., L(n_k))$ imposed. Any automorphism must send n_0 to one of the n_i, since these are all of the nodes equivalent to n_0. However to preserve this state, an automorphism must send n_0 to itself. Then the process continues recursively, replacing $Aut(H)$ with set A of automorphisms that send n_0 to itself. Because `FindSubgraphInstances` starts with a particular node that node can be considered already fixed.

The main reasons for the selection of the GROCHOW and KELLIS method are summarized as follows:

- Capable of finding more significant motifs by enabling exhaustive discovery of motifs up to seven nodes. To find even larger motifs, the method samples a connected subgraph, and then finds all its occurrences and assesses their significance using this method. This practice has enabled the algorithm to find motifs of up to fifteen nodes and examine subgraphs of up to thirty-one nodes;
- Capable of quering a particular subgraph by querying whether a particular subgraph is significant;
- Capable exploring motif clustering; because the algorithm finds all occurrences of a given subgraph, it can be used to examine how these cases cluster together to form larger structures;
- Time and space applied to all subgraphs of a set size, takes exponentially a smaller amount of time than previous methods, even when implementing the previous method with the hashing scheme.

Conclusions

Apparently the current policy enforcement solutions are not sufficient because they mainly focus on policy compliance based on the response of the device. The installation of malicious applications could alter the mobile devices response (jailbreak on IOS or Android

and software imitating a response to the MDM server) taking to more serious security issues. Similarly to the recently identified malware `Oldboot.B`, which can install malicious applications in the background, it can inject malicious modules into the system process that prevents malware applications from uninstalling. `Oldboot.B` can change the browser setup (set a new and unwanted home page), and it also can uninstall or disable installed Mobile Antivirus software, and even steal data such as credit card information or any other critical data. This malware is especially dangerous as it implements evasion techniques to stay undetected. In order to optimize current threat detection, which is also in line with business requirements, additional and different methodologies are required such as user identification based on the blueprint of the behaviour of the user.

To create a working model of the graph-based user identification, several tasks await completion. The running tasks are the edges started by the system or user defined as the connections between them. Once the complex network and graph are set up the motif can be identified with a greedy algorithm and search of the global graph with the GROCHOW-KELLIS Algorithm. In order to have a behaviour-based decision making system, all of the above algorithms will be tested to further develop the behaviour-based system.

REFERENCES

[1] AMARAL L.A.N., SCALA A., BARTHELEMY M., STANLEY H.E.: Classes of small-world networks, Proc. Natl Acad. Sci. USA *2000*, 97, 11149–11152

[2] AMARAL L.A.N., OTTINO J.M.: Complex networks. Augmenting the framework for the study of complex systems, Eur. Phys. J. B *2004*, 38, 147–162

[3] BARABÁSI A.L., OLTVAI Z.N.: Network biology: understanding the cell's functional organization, Nature Rev. Genet. *2004*, 5, 101–113

[4] GIRVAN M., NEWMAN M.E.J.: Community structure in social and biological networks. Proc. Natl Acad. Sci. USA *2002*, 99, 7821–7826

[5] RAVASZ E., BARABÁSI A.L.: Hierarchical organization in complex networks, Phys. Rev. E Stat. Nonlin. Soft Matter Phys. *2003*, 67, 026112

[6] BARTHÉLEMY M.: Betweenness centrality in large complex networks, Eur. Phys. J. B *2004*, 38, 163–168

[7] GUIMERA R., AMARAL L.A.N.: Functional cartography of complex metabolic networks, Nature *2005*, 433, 895–900

[8] GUIMERA R., MOSSA S., TURTSCHI A., AMARAL L.A.: The worldwide air transportation network: anomalous centrality, community structure and cities' global roles, Proc. Natl Acad. Sci. USA *2005*, 102, 7794–7799

[9] KASHTAN N., ALON U.: Spontaneous evolution of modularity and network motifs, Proc. Natl Acad. Sci. USA *2005*, 102, 13773–13778

[10] AMARAL L.A.N., SCALA A., BARTHELEMY M., STANLEY H.E.: Classes of small-world networks, Proc. Natl Acad. Sci. USA *2000*, 97, 11149–11152

[11] BARABÁSI A.L., ALBERT R.: Emergence of scaling in random networks, Science *1999*, 286, 509–512

[12] WATTS D.J., STROGATZ S.H.: Collective dynamics of "small-world" networks, Nature *1998*, 393, 440–442

[13] AMARAL L.A.N., OTTINO J.M.: Complex networks. Augmenting the framework for the study of complex systems, Eur. Phys. J. B *2004*, 38, 147–162

[14] BARABÁSI A.L., OLTVAI Z.N.: Network biology: understanding the cell's functional organization. Nature Rev. Genet. *2004*, 5, 101–113

[15] FREEMAN L.C.: A set of measures of centrality based on betweenness, Sociometry *1977*, 40, 35–41

[16] GIRVAN M., NEWMAN M.E.J.: Community structure in social and biological networks. Proc. Natl Acad. Sci. USA *2002*, 99, 7821–7826

[17] GUIMERÀ R., MOSSA S., TURTSCHI A., AMARAL L.A.: The worldwide air transportation network: anomalous centrality, community structure and cities' global roles. Proc. Natl Acad. Sci. USA *2005*, 102, 7794–7799

[18] GAREY M.R., JOHNSON D.S.: Computers and Intractability: A Guide to the Theory of np-completeness. New York: W. H. Freeman and Company, *1979*

[19] FEIGE U., GOLDWASSER S., LOVASZ L., SAFRA S., SZEGEDY M.: Approximating clique is almost NP complete, Proc. 32nd IEEE Symposium on Foundations of Computer Science (FOCS), *1991*, 2–12

[20] HALLDORSSON M.M., RADHAKRISHNAN J.: Greed is good: Approximating independent sets in sparse and bounded-degree graphs, Algorithmica, *1997*, 18(1), 145–163

[21] GROCHOW J.A., KELLIS M.: Network Motif Discovery using Subgraph Enumeration and Symmetry-Breaking, Computer Science and AI Laboratory, M.I.T. Broad Institute of M.I.T. and Harvard, *2007*

[22] MCKAY B.D.: Isomorph-free exhaustive generation, J. Algorithms, *1998*, 26, 306–324

HUNGARIAN JOURNAL
OF INDUSTRY AND CHEMISTRY
VESZPRÉM
Vol. 42(2) pp. 85–89 (2014)

MEASUREMENT-BASED MODELLING AND SIMULATION OF A HYDROGEN-GENERATING DRY CELL FOR COMPLEX DOMESTIC RENEWABLE ENERGY SYSTEMS

ATTILA GÖLLEI,✉ PÉTER GÖRBE, ATTILA MAGYAR, AND LÁSZLÓ NEUKIRCHNER

Department of Electrical Engineering and Information Systems, University of Pannonia, Egyetem u. 10., Veszprém, 8200, HUNGARY
✉E-mail: golleia@almos.uni-pannon.hu

Nowadays, the growing need for energy from renewable sources and growing revulsion towards fossil and nuclear fuels puts sustainable and green energy in the limelight. Producing (electrical) energy in domestic power plants from renewable sources (mainly solar and wind) hardly results in difficulties, but the storage of energy not consumed immediately is a great engineering challenge. In the present paper a complex model has been developed by investigating renewable energy sources, the surplus energy not actually consumed and stored in electrical vehicle (EV) batteries, the conversion to hydrogen for storage purposes and how the main grid is fed. A measurement-based model of a hydrogen generating cell developed for the simulation of complex energetic systems. The parameter estimation of the static model was based on the collected measurement data coming from the detailed examination of a built demonstration cell. The novel element of this work is the Matlab Simulink model for the hydrogen generation cell. Using this model, a dynamic simulator of a complex domestic power plant is made available using renewable energy sources and hydrogen generation cells. Hydrogen generation enables the lossless long-term storage of surplus electric energy collected, but not consumed or injected into the low voltage grid. The generated hydrogen can be consumed for transportation purposes in suitable vehicles or it can be applied in fuel cells generating direct electrical energy for energy-deficient low voltage network situations. Energetic situations potentially occurring in practice were simulated in our complex model. Simulations showed that the presented model is suitable for domestic scale low voltage complex energetic systems.

Keywords: hydrogen generation, renewable energy sources, domestic power plants, modelling and simulation, measurement-based modelling

Introduction

Producing hydrogen gas (H_2) from excess energy is not a new idea. This is an alternative way to store and convert renewable energy for further utilization. The produced hydrogen can be stored or used in power cells to be converted back to electric energy or in vehicles for hydrogen propulsion [1]. Although the described procedure is efficient and able to produce a high quantity of H_2 it is not suitable for application in combination with domestic power plants.

The most relevant from of H_2 production is when the energy consumption and quantity of produced H_2 are controlled. When power consumption and generation are continuous (and not necessarily deterministic) functions of time, the H_2 production depends solely on the excess energy of the grid. The best solution is the usage of Supervisory Control and data Acquisition Systems (SCADA) of management [2]. The domestic applicability of this technology in the future depends on the cost of SCADA system installation.

Producing hydrogen and oxygen gases from water using electricity in a laboratory is a simple electrochemical process that can be performed easily and in a very demonstrative way. Producing hydrogen on a large scale or in industrial quantities calls for an optimized or near-optimized cell model. In an energy demanding process only a few percent of variance in efficiency could mean a significant energy surplus or shortage [3]. The electrochemical parameters of a dry cell (*Fig.1*) that are used here are discussed to simulate hydrogen and oxygen gas production. Compared to wet oxyhydrogen (HHO) cells where the entire unit is underwater, the plates of dry cells are separated with rubber seals. These seals stop the water from leaking from the cell. The electrical connections and edges of

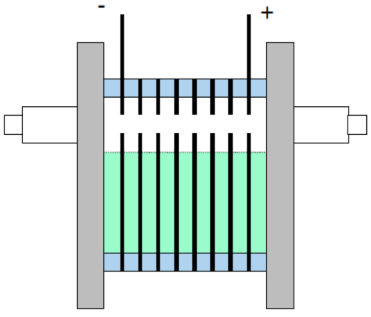

Figure 1: The theoretical setup of a dry HHO block

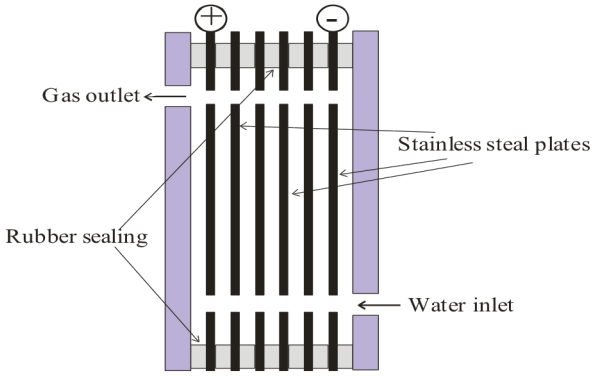

Figure 2: The setup of a HHO gas generator cell block

the plates do not touch the electrolyte. These parts of the unit stay dry, thus the name dry cell. To make sure the gas made from the electrolyte gets out of the cell and the solution flows between the plates, there are holes on the top (for the gas) and bottom (for the electrolyte) on the metal slats (*Fig.1*).

The application of dry HHO units has two main advantages. The surface of the dry cell plates enables one to use smaller amounts of electrolyte compared to with wet cells; therefore, the volume and weight of the cell is smaller. Furthermore, the connectors of dry cells remain dry, i.e. they do not corrode unlike to wet cells, where the connectors are underwater therefore their surface slowly corrodes [4].

Electrochemical Foundations

Electrochemical cells can be considered as galvanic batteries where the electrochemical reactions are supported by an external current supply. They are composed of two electrodes and a conductive electrolyte fluid. If the electrode material does not participate directly in the electrode reaction, it is called an indifferent electrode (e.g. graphite). During electrolysis, if there is more than one possible type of electrochemical reaction, then a simple anion will detach from the positive anode (e.g. chloride), without this anion, HO^- will be created by water splitting. The dissolution voltage of water is 1.23 V at 25 °C, the temperature coefficient is -0.85 mV/K, which means that at 100 °C this voltage decreases to 1.17 V. Therefore, in the light of these data, the specific energy demand to make hydrogen *via* electrolysis at 25°C can be calculated from *Eqs.(1–4)*.

The amount of charge needed to evolve 1 kg of H_2 gas is

$$q = zFM = 2 \cdot 96487 \cdot 0.5 = 96487 \text{ A s mol}^{-1} = \\ = 26801 \text{ Ah kg}^{-1} \quad (1)$$

$$w_{H_2} = qE_{MF} = 26801 \cdot 1.23 = 32966 \text{ Wh kg}^{-1} \quad (2)$$

Since the volume of 1 kg of standard state H_2 is 12474 dm^3, the amount of energy required to produce 1 dm^3 of H_2 gas is:

$$w_{H_2} = \frac{32966}{12474} = 2.64 \text{ Wh dm}^{-3} \quad (3)$$

Table 1: Experimental results

Electrolyte concentration, g dm^{-3}	MMW[a], cm^3 min^{-1} W^{-1}	Gas production, dm^3 min^{-1}	Power of unit, W
1	2.13	0.20	10.8
2	2.66	0.75	34.4
3	2.66	1.37	55.8
4	2.59	1.51	82.2
5	2.72	1.90	90.6
6	2.63	2.52	119.5
7	2.67	2.96	140.0
8	2.65	2.76	125.0
9	2.46	2.28	105.6
10	1.82	2.15	103.2

[a] millilitres per minute per watt

To generate 1 dm^3 of hydrogen gas, 1.5 dm^3 of HHO gas is needed and thus the energy demand of producing 1 ldm^3 of HHO gas (0.667 dm^3 H_2) is:

$$w_{H_2(HHO)} = 0.667 \cdot 2.64 = 1.76 \text{ Wh dm}^{-3} \quad (4)$$

The unit has been measured at 10 different electrolyte concentrations, using different currents. At the same time, the voltage on the plates and amount of gas produced by electrolysis has also been measured.

The HHO Cell Unit

The setup of one block of the unit is shown in *Fig.2*. Usually five cells make up one block giving one gas-producing block. The block's electrical connections are on the ends of two plates (*Fig.1*). Four of the six electrode plates are neutral electrodes, as there is no voltage connected to them. The potential is divided between the neutral plates according to voltage division in series connections. It means that the voltage between two electrodes is one fifth of the voltage on one whole block. In the experiment, a unit with three blocks connected in parallel has been used. Besides the HHO cell, a water reserve tank to infuse the electrolyte into the cell was necessary. A tube between the gas outlet and the tank has also been installed since due to bubbling, electrolyte comes out of the tube that needs to be recycled back into the system. Then, as the electrolyte drips back into the tank, the gas can escape into the bottle through another hose. The produced H_2 volume and the production speed are measured with this bottle. A power supply (Manson SPS9600) has been connected to the electrical connections of the HHO unit, in this way the input current was controlled (*Table 1*).

Matlab Model of the Dry Cell

The model of the dry cell considered was implemented in Matlab Simulink using the SimPowerSystems Toolbox. Two unknown functional relationships between the generated H_2 volume, the cell current and the KOH concentration and between cell voltage, cell current and KOH concentration were approximated using fourth and third order polynomials, respectively

Table 2: Coefficients of the polynomial relationship describing the cell voltage

	Value		Value		Value
p_{00}	1.429	p_{10}	0.2548	p_{01}	-0.1226
p_{20}	-0.008571	p_{11}	-0.01191	p_{02}	0.008257
p_{30}	0.0001141	p_{21}	-8.76e-05	p_{12}	0.0009697

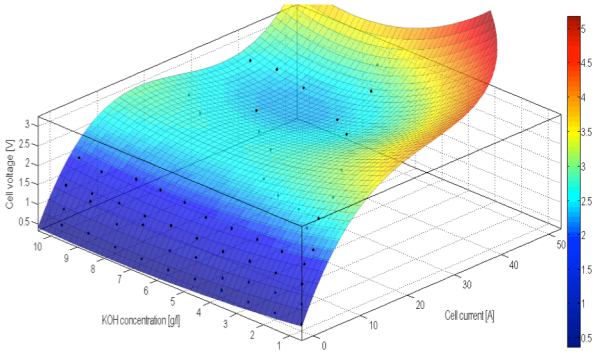

Figure 3: Simulation of the cell model with a constant current of 5 A for 1 day

using the Matlab Surface Fitting Tool. As the fitted polynomials do not have a physical connection to the given device, the model is applicable to any similar electrochemical H_2 generation device with an electric two-pole system. In the different linear and non-linear physical and chemical models different coefficients become dominant. The voltage relationship is given by *Eq.(5)*, where i_{cell} denotes the cell current and c_{KOH} stands for the KOH concentration. Parameters can be found in *Table 2*.

$$u_{cell}(i_{cell},c_{KOH}) = p_{00} + p_{10}\, i_{cell} + p_{01}\, c_{KOH} + p_{20}\, i_{cell}^2 + p_{11}\, i_{cell} c_{KOH} + p_{02} c_{KOH}^2 + p_{30} i_{cell}^3 + p_{21} i_{cell}^2 c_{KOH} \quad (5)$$

The volume of the generated H_2 is given by *Eq.(6)*.

$$H_2(i_{cell},c_{KOH}) = p_{00} + p_{10}\, i_{cell} + p_{01}\, c_{KOH} + p_{20}\, i_{cell}^2 + p_{11}\, i_{cell} c_{KOH} + p_{02}\, c_{KOH}^2 + p_{30}\, i_{cell}^3 + p_{21}\, i_{cell}^2 c_{KOH} + p_{12}\, i_{cell} c_{KOH}^2 + p_{03}\, c_{KOH}^3 + p_{40}\, i_{cell}^4 + p_{31}\, i_{cell}^3 c_{KOH} + p_{22}\, i_{cell}^2 c_{KOH}^2 + p_{13}\, i_{cell} c_{KOH}^3 \quad (6)$$

Table 3 and *Figs.3-4* show representative results for the model. As expected, the H_2 generation speed decreases and the cell finally stops working as the amount of water decreases and the KOH concentration increases.

A Simulink block scheme of the cell model is depicted in *Fig.5*. This Simulink model was validated by considering a system with the same parameters as the layout of the experimental cell. In this layout, we ran a simulation for 24 h using this model, decreasing water and increasing KOH concentrations. The results of this simulation can be seen in *Fig.6*. It can be seen that the hydrogen gas generated is reduced because of the rising KOH concentration. The exact values are in good agreement with our measurements.

Table 3: Coefficients of the polynomial relationship for the generated H_2 gas

	Value		Value		Value
p_{00}	-0.1695	p_{10}	0.1687	p_{01}	-0.01765
p_{20}	-0.007486	p_{11}	-0.03234	p_{02}	0.03446
p_{30}	-0.0001077	p_{21}	0.00412	p_{12}	-0.004094
p_{03}	-0.004061	p_{40}	-4.269e-06	p_{13}	6.169e-05
p_{22}	-0.0005518	p_{13}	0.0009544		

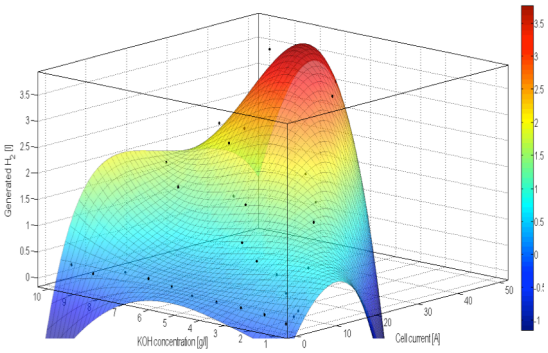

Figure 4: Generated H_2 as a function of KOH concentration and dry cell current

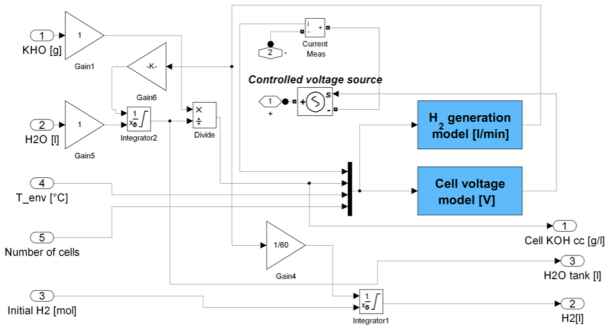

Figure 5: Matlab Simulink model of the HHO cell. The functional blocks implementing *Eqs.(5)* and *(6)* are denoted by different background colours

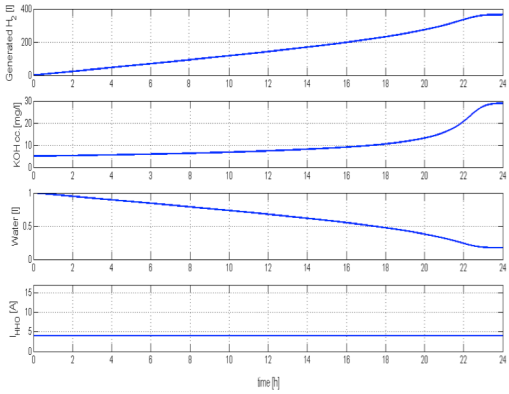

Figure 6: Simulation of a cell model with a constant current of 5 A for 1 day

Dry Cell Model in Complex Energetic Systems

The model for H_2 generating cells described in the previous section was investigated in the Matlab Simulink simulation environment that studies the energy flow conditions of a complex energetic system consisting of a renewable source with a grid-

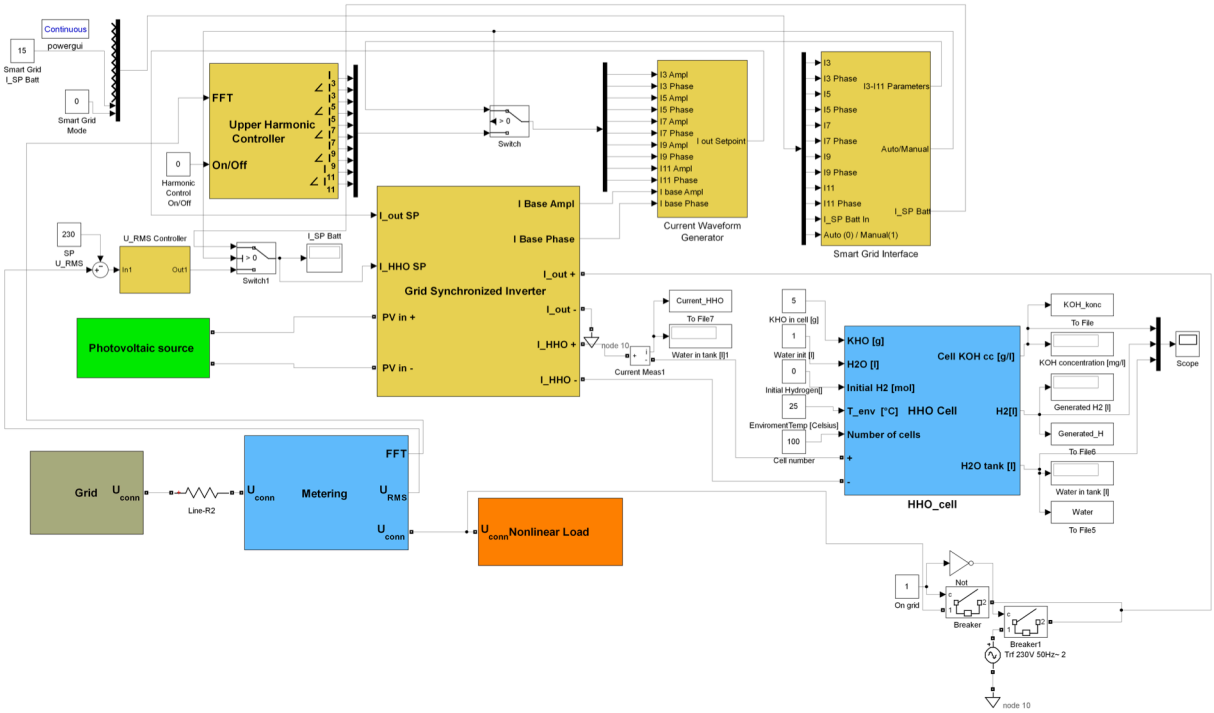

Figure 7: Simulink model of a complex energetic system with an HHO cell model inside

synchronized inverter, a low voltage grid, an intermediate voltage controller [3,5] and a lithium ion battery. We replaced the lithium ion battery in this cell model, which reduces the potential energy flow modes, because this cell can only adsorb current for storing energy in hydrogen production. It cannot reverse the electrochemical process for electrical energy generation from hydrogen gas. The structure of the system can be seen in *Fig.7*, where it is apparent that the cell model is connected directly only to the grid-synchronized inverter module of the system. The system depicted in *Fig.7* operates in different discrete states according to the energy flow direction. Four cases can be defined:

- Normal inverter mode: The energy flows from the renewable source to the grid only (*Fig.8A*).
- Normal inverter and hydrogen generation mode: The energy flows from the renewable source to both the dry cell and the grid (*Fig.8B*).
- Hydrogen generation only mode: The energy flows from the grid to the dry cell only (*Fig.8C*).
- Distortion reduction only mode: The energy flows from the grid into the intermediate capacitance and from the intermediate capacitance into the grid. The energy balance is zero for a period, and the active power is zero (*Fig.8D*).

Model verification was performed by changing the energy flow modes in subsequent time intervals, and this was implemented by changing the energy balance of the system with outer current loads ($I_{\text{outer load}}$). The different values for the simulations as parameters can be

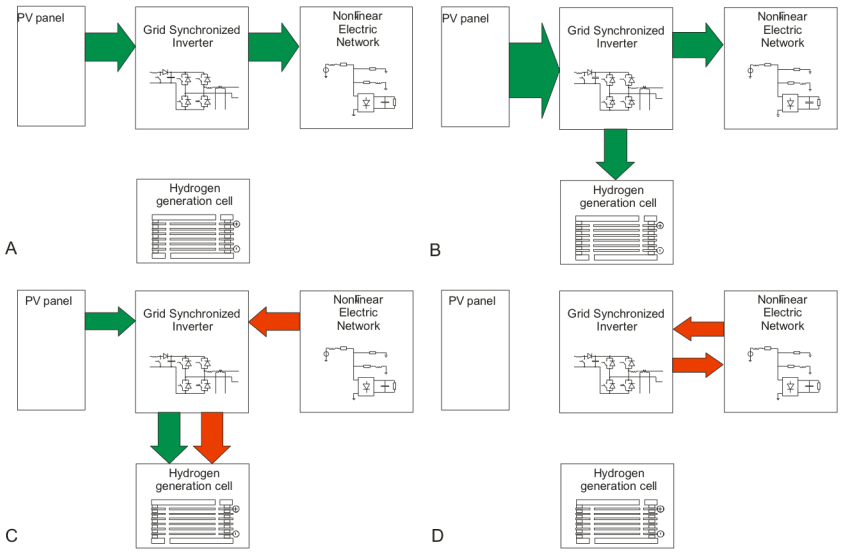

Figure 8: Complex energetic system energy flow modes: A: normal inverter mode, B: inverter and hydrogen generator mode, C: hydrogen generation only mode, D: distortion reduction only mode

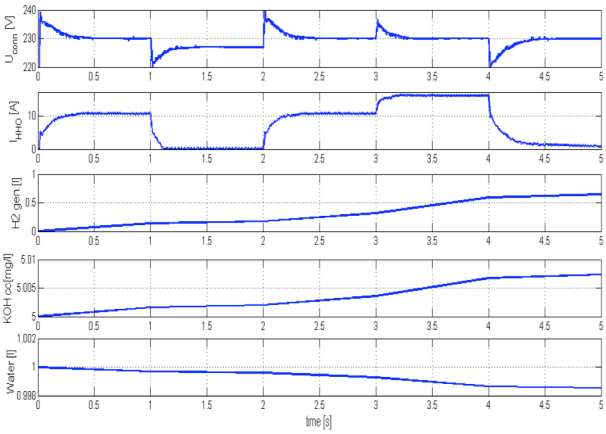

Figure 9: Simulation results of a complex energetic system using a cell model short time range (5 sec)

seen in *Table 4*. The simulation results are shown in *Fig.9*, where U_{conn} is the effective value of the voltage at the connection point, I_{HHO} is the current value of the dry cell, V_{H_2} is the volume of generated hydrogen gas, c_{KOH} is the KOH concentration of the electrolyte and V_{water} is the volume of water inside the cell system. These values are plotted as a function of time. The results of the simulation show that the behaviour of the simulated electronic two-pole system is identical to that of the measured database.

Conclusion

We developed a complex model to investigate renewable energy sources, for the conversion of surplus energy to hydrogen gas for storage and to represent how a main grid is fed. We built a measurement-based model of a hydrogen-generating cell for the simulation of complex energy systems in MATLAB SIMULINK environment. We estimated the parameters of the model based on measurements collected during the detailed examination of a demonstration cell. We carried out a series of experiments on a HHO gas producing dry cell to find the optimal electrolyte concentration, current value, etc. or change the setup by altering the distance between the plates with KOH electrolyte solution. We monitored the experimental setup in several regards, for example cell voltage, and gas production. The novel element is the temperature and concentration dependent Matlab Simulink model of the hydrogen generation cell, which was found to be suitable for simulation purposes. We tested it in a simulation of a complex domestic power plant using a renewable energy source and hydrogen generation cell. Hydrogen generation enables the long-term storage of surplus electrical energy collected, but not consumed or injected into the low voltage grid. The generated hydrogen can be consumed by vehicles for transportation purposes or it can be applied in fuel cells generating direct electrical energy for energy-deficient low voltage network situations. We simulated all the potential energetic situations in this complex model of an energetic system. The simulations showed that the presented model of a hydrogen-generating cell performed well.

ACKNOWLEDGEMENT

We acknowledge the financial support of this work by the Hungarian State and the European Union under the TAMOP-4.2.2.A-11/1/ KONV-2012-0072 project.

REFERENCES

[1] KOUTSONIKOLASA D.E., KALDISA, S.P., PANTOLEONTOSB, G.T., ZASPALISAC, V.T., SAKELLAROPOULOSC, G.P.: Techno-Economic Assessment of Polymeric, Ceramic and Metallic Membranes Integration in an Advanced IGCC Process for H_2 Production and CO_2 Capture, Chem. Engng. Trans. *2013*, 35, 715-720

[2] ZIOGOUA C., ELMASIDESB C., PAPADOPOULOUCA S., VOUTETAKISA S.: Supervisory Control and Unattended Operation of an Off-Grid Hybrid Power Generation Station with Hydrogen Storage Chem. Engng. Trans. *2013*, 35, 529-534

[3] GÖRBE P., MAGYAR A., HANGOS K.M.: Line Conditioning with Grid Synchronized Inverter's Power Injection of Renewable Sources in Nonlinear Distorted Mains, Proc. 10th International PhD Workshop on Systems and Control, *2009*, 978-980

[4] AL-ROUSAN A.A.: Reduction of fuel consumption in gasoline engines by introducing HHO gas into intake manifold, Int. J. Hydrogen Energy, *2010*, 35, 12930-12935

[5] GÖRBE P., MAGYAR A., HANGOS K.M.: THD Reduction with Grid Synchronized Inverter's Power Injection of Renewable Sources, Proc. 20th Int. Symp. Power Electronics, Electrical Drives, Automation and Motion (SPEEDAM) *2010*, 1381-1386

HUNGARIAN JOURNAL OF INDUSTRY AND CHEMISTRY

HJIC

Advertise upcoming meetings,

conferences, workshops,

new products or services;

make public announcements,

introduce your research laboratory

on the pages of the

Hungarian Journal of Industry and Chemistry

Please contact us if interested!

EDITORIAL OFFICE: UNIVERSITY OF PANNONIA
P.O. BOX 158, VESZPRÉM H-8201 (HUNGARY)
Tel.: +36 (88) 624-746, E-mail: hjic@almos.uni-pannon.hu;
web: hjic.mk.uni-pannon.hu
Felelős szerkesztő: Szilágyi Róbert Károly, PhD
Kiadja: Pannon Egyetem, 8200 Veszprém, Egyetem u. 10.
Levélcím: H-8201 Veszprém, Postafiók 158, Tel.: (88) 624-000
Felelős kiadó: a Pannon Egyetem, Mérnöki Kar dékánja

HUNGARIAN JOURNAL
OF INDUSTRY AND CHEMISTRY
VESZPRÉM
Vol. 42(2) pp. 91–95 (2014)

QUASI-POLYNOMIAL REPRESENTATION-BASED CONTROL OF MECHANICAL SYSTEMS

LÁSZLÓ NEUKIRCHNER✉ AND ATTILA MAGYAR

Department of Electrical Engineering and Information Systems, University of Pannonia, Egyetem u. 10., Veszprém, 8200, HUNGARY
✉E-mail: neu.groszber@gmail.com

A simple kinematic model of a differential steering mobile robot is investigated using a nonlinear technique based on the quasi-polynomial representation of the dynamical model. Dynamical systems can be embedded in the generalized Lotka-Volterrs (or quasi-polynomial) form under mild conditions. Quasi-polynomial systems are good candidates for a general nonlinear system representation, since their global stability analysis is equivalent to the feasibility of a linear matrix inequality. The stabilizing quasi-polynomial state feedback controller design problem is equivalent to the feasibility of a bilinear matrix inequality. The classical stabilizing state feedback problem for quasi-polynomial systems was extended with the ability of tracking time-dependent reference signals. It is shown that the stabilizing quasi-polynomial controller design is equivalent to a bilinear matrix inequality. The results are applied to the model of the differential steering mobile robot. The goal reaching quasi-polynomial controller is shown to be a special kind of proportional state feedback.

Keywords: quasi-polynomial, robotics, differential drive robot, control systems, kinematics, Lotka-Volterra system

Introduction

Trajectory and goal tracking of mobile robots is an intensively studied field of modern robotics as well as modern control theory. Several papers deal with an adaptive output feedback approach [1]. On the other hand some groups try to apply neural network-based methods for the task [2]. Another direction is to describe the problem as an optimal control problem and apply optimal control results for it [3]. The class of quasi-polynomial (QP) systems plays an important role in the theory of nonlinear dynamical systems because nonlinear systems with smooth nonlinearities can be transformed into quasi-polynomial form Ref.[4]. This means, that any applicable method for quasi-polynomial systems can be regarded as a general technique for nonlinear systems [5]. The aim of this work is to widen the applicability of the quasi-polynomial representation-based methods to the class of mechanical systems, more precisely to mobile robots. The goal reaching problem of a differential steering mobile robot is reformulated as a globally stabilizing feedback design problem in the quasi-polynomial framework.

Basic Notions

Differential Drive Mobile Robot Kinematics

The chosen mechanical system is the kinematic model of a two wheeled differential drive mobile robot *Eq.(1)*. The model deals with the geometric relationships that govern the system. It calculates the motion without considering the affecting forces. The system's states are the Cartesian coordinates x, and y and the orientation θ of the mobile robot. The basic kinematic model of the differential drive robot is given by

$$\begin{aligned} \dot{\theta} &= \frac{r}{2a}(\omega_{\text{left}} - \omega_{\text{right}}) \\ \dot{x} &= \frac{r}{2}\cos(\theta)(\omega_{\text{left}} + \omega_{\text{right}}) \\ \dot{y} &= \frac{r}{2}\sin(\theta)(\omega_{\text{left}} + \omega_{\text{right}}), \end{aligned} \tag{1}$$

where a is half the shaft's diameter, r is the radius of the wheels and ω is the angular velocity of the right or left wheel. To order the robot to reach a specific goal, it is acceptable to design a proportional controller to govern the expected trajectory *Eq.(2)* [6] . In this case, the model is modified to calculate the state errors between the ordered and the present value. The new error model with proportional gain is

$$\begin{aligned} \dot{x} &= K_{\text{v}}(e_{\text{dis}}\cos(\theta) - x(t)) \\ \dot{y} &= K_{\text{v}}(e_{\text{dis}}\sin(\theta) - y(t)) \\ \dot{\theta} &= K_{\text{h}}(e_{\text{ang}} - \theta(t)) \\ e_{\text{dis}} &= \sqrt{(x_{\text{g}} - x(t))^2 + (y_{\text{g}} - y(t))^2} \\ e_{\text{ang}} &= \arctan\left(2\frac{y_{\text{g}} - y(t)}{x_{\text{g}} - x(t)}\right), \end{aligned} \tag{2}$$

where K_{v} is the velocity control gain, K_{h} is the rotational velocity control gain, e_{dis} is the distance error, e_{ang} is the

angular error, and x_g, y_g are the Cartesian coordinates to reach.

Quasi-Polynomial Representation of Nonlinear Systems

Some basic notions of quasi-polynomial and Lotka-Volterra systems are summarised in this section.

Generalised Lotka-Volterra Form

Representing an ODE in generalised Lotka-Volterra (GLV) form can increase the structural simplicity in exchange for increasing its dimension. The GLV or quasi-polynomial (QP) form:

$$\begin{aligned} \dot{x}_i &= x_i \left(\lambda_i + \sum_{i=1}^{m} A_{ij} \cdot \prod_{k=1}^{n} x_k^{B_{ij}} \right), \\ i &= 1, \ldots, n, \\ m &\geq n \end{aligned} \tag{3}$$

where $\boldsymbol{A}$ and $\boldsymbol{B}$ are $n \times m$, $m \times n$ real matrices, and $\boldsymbol{\lambda} \in \mathbb{R}^n$ is a vector. The set of non-linear ODEs can be embedded into QP form if it meets two requirements: (i) The non-linear ODEs should follow this form:

$$\begin{aligned} \dot{x}_s &= \sum_{i_{s1} \ldots i_{sn}, j_s} a_{i_{s1} \ldots i_{sn}, j_s} x_1^{i_{s1}} \ldots x_n^{i_{sn}} f(\bar{x})^{j_s}, \\ x_s(t_0) &= x_s^0, \\ s &= 1 \ldots n \end{aligned} \tag{4}$$

where $a_{i_{s1} \ldots i_{sn}, j_s} \epsilon R$, $s = 1 \ldots n$, and $f(\bar{x})$ is some scalar function which cannot be reduced to quasy-monomial form. (ii) The partial derivatives of the system *Eq.(4)* should fulfil:

$$\frac{\partial f}{\partial x_s} = \sum_{e_{s1} \ldots e_{sn}, e_s} b_{e_{s1} \ldots e_{sn}, e_s} x_1^{e_{s1}} \ldots x_n^{e_{sn}} f(\bar{x})^{e_s}, \tag{5}$$

where $b_{e_{s1} \ldots e_{sn}, e_s} \epsilon R$, $s = 1 \ldots n$. By embedding, we introduce the new auxiliary variable:

$$\begin{aligned} y &= f^q \prod_{s=1}^{n} x^p s_s. \\ q &\neq 0 \end{aligned} \tag{6}$$

Differentiating the new, substituted equations we get the QP representation of the original equation *Eq.(4)*:

$$\begin{aligned} \dot{x}_s &= x_s \left[\sum_{i_{s1} \ldots i_{sn}, j_s} \left(a_{i_{s1} \ldots i_{sn} j_s} y^{j_s/q} \right. \right. \\ &\quad \left. \left. \prod_{k=1}^{n} x^{i_{sk} - \delta_{sk} - j_s p_k / q} \right) \right], \\ s &= 1 \ldots n \end{aligned} \tag{7}$$

where $\delta_{sk} = 1$ if $s = k$ and 0 otherwise. A new additional dimension appears as the ODE of the new variable y:

$$\begin{aligned} \dot{y} &= y \left[\sum_{i_{s1} \ldots i_{sn}, j_s} \left(p_s x_s^{-1} \dot{x}_s + \right. \right. \\ &\quad + \sum_{\substack{i_{s\alpha}, j_s \\ e_{s\alpha}, e_s}} a_{i_{s\alpha}, j_s} b_{i_{s\alpha}, j_s} q y^{(e_s + j_s - 1)/q} \times \\ &\quad \left. \left. \times \prod_{k=1}^{n} x_k^{i_{sk} + e_{sk} + (1 - e_s - j_s) p_k} \right) \right]. \\ \alpha &= 1 \ldots n \end{aligned} \tag{8}$$

It is important to mention that the new ODE is not unique because we can choose the parameters p_s and q.

The quasi-monomial transformation is defined as:

$$\begin{aligned} x_i &= \prod_{k=1}^{n} x_k^{C_{ik}}, \\ i &= 1 \ldots n \end{aligned} \tag{9}$$

where C is an arbitrary invertible matrix. The matrices of GLV can be modified as $\hat{B} = B \cdot C$, $\hat{A} = C^{-1} \cdot A$, and $\hat{\lambda} = C^{-1} \cdot \lambda$, and the transformed set is also in GLV form.

Lotka-Volterra Models

The above family of models is split into classes of equivalence according to the values of the products $\boldsymbol{M} = \boldsymbol{B}\,\boldsymbol{A}$ and $\boldsymbol{N} = \boldsymbol{B}\,\boldsymbol{L}$. The *Lotka-Volterra form* gives the representative elements of these classes of equivalence. If rank$(\boldsymbol{B}) = n$, then the set of ODEs in *Eq.(3)* can be embedded into the following *m*-dimensional set of equations, the so-called Lotka-Volterra model:

$$\dot{z}_j = z_j \left(N_j + \sum_{i=1}^{m} M_{ji} z_i \right), \quad j = 1, \ldots, m \tag{10}$$

where

$$\boldsymbol{M} = \boldsymbol{B}\,\boldsymbol{A}, \quad \boldsymbol{N} = \boldsymbol{B}\,\boldsymbol{L},$$

and each z_j represents a so-called *quasi-monomial*:

$$z_j = \prod_{k=1}^{n} y_k^{B_{jk}}, \qquad j = 1, \ldots, m. \tag{11}$$

Input-Affine QP Model

The well known input-affine model of nonlinear systems is given in the following state space model:

$$\dot{x} = \boldsymbol{f}(\boldsymbol{x}) + \sum_{j=1}^{p} \boldsymbol{g_j}(\boldsymbol{x}) u_j$$

where $\boldsymbol{f} \in \mathbb{R}^n \to \mathbb{R}^n$, and $\boldsymbol{g_j} \in \mathbb{R}^n \to \mathbb{R}^n$ are QP functions and the input variable $\boldsymbol{u}$ is p-dimensional. In

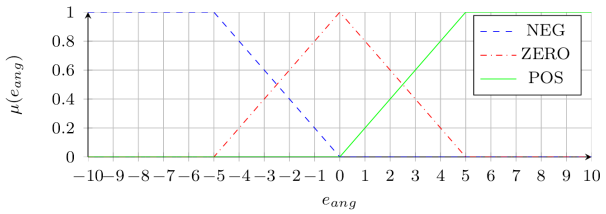

Figure 1: Membership functions for angular error

this case we need a QP form with the matrices from the GLV form ODE set:

$$\begin{aligned}\dot{x}_i &= x_i\left(\lambda_i + \sum_{j=1}^{m} A'_{ij}\prod_{k=1}^{n} x_k^{B_{jk}}\right) + \\ &+ \sum_{l=1}^{p} x_i\left(\mu_{li} + \sum_{j=1}^{m} C_{lij}\prod_{k=1}^{n} x_k^{B_{jk}}\right) u_l. \\ i &= 1\ldots n \end{aligned} \tag{12}$$

It can be proven that if $u = H(x)$ state feedback is in QP form, the closed-loop system remains in QP form as well, but the quasi-monomials of the system will be greater, than the system's without the feedback.

Global Stability Analysis

Global equilibrium points can be obtained by finding a Lyapunov function $V(\cdot)$. For LV systems there is a well known Lyapunov function family:

$$\begin{aligned} V(\boldsymbol{z}) &= \sum_{i=1}^{m} c_i\left(z_i - z_i^* - \ln\frac{z_i}{z_i^*}\right), \\ & c_i \geq 0, i = 1\ldots m \end{aligned} \tag{13}$$

and the time derivative:

$$\begin{aligned}\dot{V}_z &= \frac{\partial V(\boldsymbol{z})}{\partial \boldsymbol{z}}\cdot\frac{\partial \boldsymbol{z}}{\partial t} = \\ &= \frac{1}{2}(\boldsymbol{z}-\boldsymbol{z}^*)(\boldsymbol{C}\,\boldsymbol{M} + \boldsymbol{M}^T\,\boldsymbol{C})(\boldsymbol{z}-\boldsymbol{z}^*),\end{aligned} \tag{14}$$

where $\boldsymbol{z^*} = (z_1^*\ldots z_m^*)^T$ is the unique positive equilibrium point, $\boldsymbol{C} = \mathrm{diag}(c_1,\ldots,c_m)$ and $\boldsymbol{M}$ is the invariant coefficient matrix of the LV form. If $\boldsymbol{C}\,\boldsymbol{M}^T + \boldsymbol{M}\,\boldsymbol{C}$ is negative semi-definite then $\boldsymbol{z}^*$ is stable and if negative definite then $\boldsymbol{z}^*$ is asymptotically stable. The global stability analysis is thus equivalent to the linear matrix inequality

$$\begin{aligned}\boldsymbol{C}\,\boldsymbol{M}^T + \boldsymbol{M}\,\boldsymbol{C} &\leq 0 \\ \boldsymbol{C} &> 0.\end{aligned} \tag{15}$$

The presented Lyapunov function *Eq.(13)* can be extended to GLV systems by embedding the system using the LV coefficient matrix $\boldsymbol{M} = \boldsymbol{B}\,\boldsymbol{A}$. It is necessary to solve the LMI system *Eq.(15)* for the stability analysis of the QP and LV system:

$$\begin{pmatrix} \boldsymbol{C} & 0 \\ 0 & -\boldsymbol{C}\,\boldsymbol{M}^T - \boldsymbol{M}\,\boldsymbol{C}\end{pmatrix} > 0 \tag{16}$$

Controller Design in Quasi-Polynomial Representation

The globally stabilizing QP state feedback design problem for QP systems can be formulated as follows [7]. Consider arbitrary quasi-polynomial inputs in the form:

$$u_l = \sum_{i=1}^{r} k_{il}\hat{q}_i, \quad l = 1\ldots,p \tag{17}$$

where $\hat{q}_i = \hat{q}_i(y_1,\ldots,y_n)$, $i = 1,\ldots,r$ are arbitrary quasi-monomial functions of the state variables of the system and k_{il} is the constant gain of the quasi-monomial function $\hat{q}_i$ in the l-th input u_l. The closed-loop system will also be a QP system furthermore, the closed-loop LV coefficient matrix $\hat{\boldsymbol{M}}$ can also be expressed in the form

$$\hat{\boldsymbol{M}} = \hat{\boldsymbol{B}}\,\hat{\boldsymbol{A}} = \boldsymbol{M_0} + \sum_{l=1}^{p}\sum_{i=1}^{r} k_{il}\boldsymbol{M_{il}}. \tag{18}$$

Then the global stability analysis of the closed-loop system with unknown feedback gains k_{il} leads to the following *bilinear matrix inequality*

$$\begin{aligned}\hat{\boldsymbol{M}}^T\boldsymbol{C} + \boldsymbol{C}\hat{\boldsymbol{M}} = \boldsymbol{M_0}^T\boldsymbol{C} + \boldsymbol{C}\boldsymbol{M_0} + \\ \sum_{l=1}^{p}\sum_{i=1}^{r} k_{il}\left(\boldsymbol{M_{il}}^T\boldsymbol{C} + \boldsymbol{C}\boldsymbol{M_{il}}\right) \leq 0.\end{aligned} \tag{19}$$

The variables of the BMI are the $p \times r$ k_{il} feedback gain parameters and the c_j, $j = 1,..,m$ parameters of the Lyapunov function. If the BMI above is feasible then there exists a globally stabilizing feedback with the selected structure.

Quasi-Polynomial Control of a Differential Drive Mobile Robot

Quasi-Polynomial Representation of the Kinematic Model

With the given differential drive robot model *Eq.(1)* and the explained error model *Eq.(2)* the QP representation can be built. The fist step as mentioned, is to find the new auxiliary variables, that help to eliminate the non-QP expressions. The newly chosen auxiliary variables are:

$$\begin{aligned}\alpha &= \cos(\theta), \\ \beta &= \sin(\theta), \\ \gamma &= \arctan\left(2\frac{y_\mathrm{g}-y}{x_\mathrm{g}-x}\right), \\ \delta &= (x_\mathrm{g}-x)^2 + (y_\mathrm{g}-y)^2, \text{and} \\ \epsilon &= \sqrt{\delta} + (x_\mathrm{g}-x).\end{aligned} \tag{20}$$

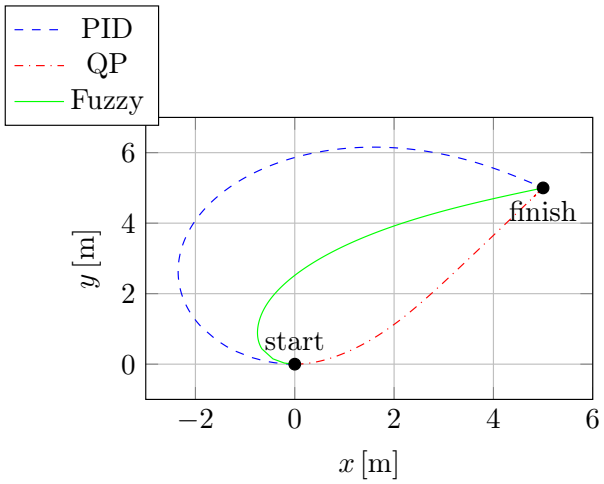

Figure 2: Comparison of different controllers

By substituting them into the original system *Eq.(2)* and performing the differentiation of the new equations *Eq.(20)*:

$$\begin{aligned}
\dot{x} &= x\left(\frac{K_\mathrm{v}\sqrt{\delta}\alpha}{x} - K_\mathrm{v}\right)\\
\dot{y} &= y\left(\frac{K_\mathrm{v}\sqrt{\delta}\beta}{y} - K_\mathrm{v}\right)\\
\dot{\theta} &= \theta\left(\frac{K_\mathrm{h}\gamma}{\theta} - K_\mathrm{h}\right)\\
\dot{\alpha} &= \alpha\left(-\frac{\beta}{\alpha}\right)\\
\dot{\beta} &= \beta\left(\frac{\alpha}{\beta}\right)
\end{aligned} \tag{21}$$

$$\begin{aligned}
\dot{\gamma} = \gamma\cdot\Big(&-\tfrac{2K_\mathrm{v}\beta\sqrt{\delta}}{\gamma\epsilon} + \tfrac{K_\mathrm{v}y}{\gamma\epsilon} - \tfrac{K_\mathrm{v}x_\mathrm{g}\beta}{\gamma\epsilon} + \tfrac{K_\mathrm{v}x\beta}{\gamma\epsilon}\\
&+\tfrac{K_\mathrm{v}x_\mathrm{g}y}{\gamma\epsilon\sqrt{\delta}} - \tfrac{K_\mathrm{v}xy}{\gamma\epsilon\sqrt{\delta}} + \tfrac{K_\mathrm{v}y_\mathrm{g}\alpha}{\gamma\epsilon} - \tfrac{K_\mathrm{v}y\alpha}{\gamma\epsilon}\\
&-\tfrac{K_\mathrm{v}y_\mathrm{g}x}{\gamma\epsilon\sqrt{\delta}} + \tfrac{K_\mathrm{v}xy}{\gamma\epsilon\sqrt{\delta}}\Big)
\end{aligned} \tag{22}$$

$$\begin{aligned}
\dot{\delta} = \delta\Big(&-\tfrac{2K_\mathrm{v}x_\mathrm{g}\alpha}{\sqrt{\delta}} + \tfrac{2K_\mathrm{v}x_\mathrm{g}x}{\delta} + \tfrac{2K_\mathrm{v}x\alpha}{\sqrt{\delta}} - \tfrac{2K_\mathrm{v}x^2}{\delta}\\
&-\tfrac{2K_\mathrm{v}y_\mathrm{g}\beta}{\sqrt{\delta}} + \tfrac{2K_\mathrm{v}y_\mathrm{g}y}{\delta} + \tfrac{2K_\mathrm{v}y\beta}{\sqrt{\delta}} - \tfrac{2K_\mathrm{v}y^2}{\delta}\Big)
\end{aligned} \tag{23}$$

$$\begin{aligned}
\dot{\epsilon} = \epsilon\Big(&-\tfrac{K_\mathrm{v}x_\mathrm{g}\alpha}{\epsilon} + \tfrac{K_\mathrm{v}x\alpha}{\epsilon} + \tfrac{K_\mathrm{v}x_\mathrm{g}x}{\epsilon\sqrt{\delta}} - \tfrac{K_\mathrm{v}x^2}{\epsilon\sqrt{\delta}}\\
&-\tfrac{K_\mathrm{v}y_\mathrm{g}\beta}{\epsilon} + \tfrac{K_\mathrm{v}y\beta}{\epsilon} + \tfrac{K_\mathrm{v}y_\mathrm{g}y}{\epsilon\sqrt{\delta}} - \tfrac{K_\mathrm{v}y^2}{\epsilon\sqrt{\delta}}\\
&+\tfrac{K_\mathrm{v}\alpha}{\epsilon} - \tfrac{K_\mathrm{v}x}{\epsilon\sqrt{\delta}}\Big)
\end{aligned} \tag{24}$$

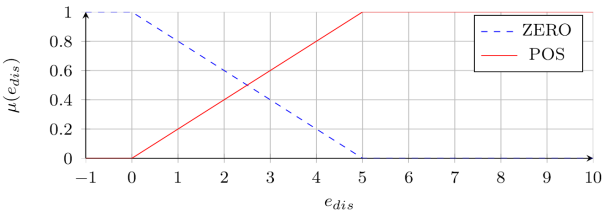

Figure 3: Membership functions for distance error

The closed-loop QP system *Eq.(21-24)* has 29 quasi-monomials.

$$\begin{aligned}
x:&\ \alpha\sqrt{\delta}x^{-1}\\
y:&\ \beta\sqrt{\delta}y^{-1}\\
\theta:&\ \gamma\theta^{-1}\\
\alpha:&\ \beta\alpha^{-1}\\
\beta:&\ \alpha\beta^{-1}\\
\gamma:&\ \beta\sqrt{\delta}\gamma^{-1}\epsilon^{-1},\ y\gamma^{-1}\epsilon^{-1},\ \beta\gamma^{-1}\epsilon^{-1},\\
&\ x\beta\gamma^{-1}\epsilon^{-1},\ y\gamma^{-1}\delta^{-1/2}\epsilon^{-1},\ \alpha\gamma^{-1}\epsilon^{-1},\\
&\ y\alpha\gamma^{-1}\epsilon^{-1},\ x\gamma^{-1}\delta^{-1/2}\epsilon^{-1}\\
\delta:&\ \alpha\delta^{-1/2},\ x\delta^{-1},\ x\alpha\delta^{-1/2},\\
&\ x^2\delta^{-1},\ \beta\delta^{-1/2},\ y\delta^{-1},\\
&\ y\beta\delta^{-1/2},\ y^2\delta^{-1}\\
\epsilon:&\ \alpha\epsilon^{-1},\ x\alpha\epsilon^{-1},\ x\epsilon^{-1}\delta^{-1/2},\\
&\ x^2\epsilon^{-1}\delta^{-1/2},\ \beta\epsilon^{-1},\ y\beta\epsilon^{-1},\\
&\ y\epsilon^{-1}\delta^{-1/2},\ y^2\epsilon^{-1}\delta^{-1/2},
\end{aligned} \tag{25}$$

The QP system *Eq.(21-24)* can obtain the GLV form invariants with the help of monomials.

These matrices are: $\boldsymbol{A}$ the coefficient matrix, $\boldsymbol{B}$ the exponential matrix and $\boldsymbol{\lambda}$ the constant's matrix. The invariant matrix product $\boldsymbol{B}\,\boldsymbol{A}$ results in the LV coefficient matrix $\boldsymbol{M}$, which is necessary for the global stability analysis.

Controller Design

As the original model *Eq.(2)* already contains the proportional controller parameters K_h and K_v, they naturally appear in the QP and Lotka-Volterra forms, respectively.

The closed-loop Lotka-Volterra coefficient matrix $\boldsymbol{M}$ contains the proportional gains in a linear manner *Eq.(26)* [7]

$$\boldsymbol{M} = \boldsymbol{M}_0 + K_\mathrm{h}\,\boldsymbol{M}_\mathrm{h} + K_\mathrm{v}\,\boldsymbol{M}_\mathrm{v}, \tag{26}$$

where $\boldsymbol{M} \in \mathbb{R}^{29\times 29}$. This means, that the globally stabilizing feedback design BMI can be formulated, and checked for feasibility.

The controller design is practically solved as a control-Lyapunov function-based state feedback. The prescribed Lyapunov function parameters are $c_{1,2,3} = 0.1$, $c_{4,5} = 1$ and $c_{6-29} = 0$. The control gains are obtained by solving an LMI version of the feedback design BMI by substituting $\boldsymbol{C}$ into *Eq.(19)*. The obtained values are $K_\mathrm{h} = 2.78$ and $K_\mathrm{v} = 0.8$.

Table 1: Rules for the fuzzy controller

$\wedge$			$\wedge$	
e_{ang}	e_{dis}		ω_{left}	ω_{right}
ZERO	ZERO		ZERO	ZERO
POS	ZERO		POS	NEG
	ZERO	$\Rightarrow$	NEG	POS
ZERO	POS		POS	POS
POS	POS		POS	ZERO
	POS		ZERO	POS

Comparison of Results for Different Controller Types

The first and most basic method was the proportional controller approach. This was explained in the second chapter. This is a more systematic approach, but with the increasing non-linearities it is becoming a more difficult method to solve. *Fig.3* shows that the robot moves on a significantly wider curve compared to the other two designs.

Secondly a fuzzy controller was designed to compare the original design to. This is a much more intuitive approach, the physical nonlinearities were easily implementable with the cost of inaccuracy. This can be seen in *Fig.3*, where the robot travels on a much smaller curve. *Table 1* shows the definition of the rules. The membership functions follow simple triangular shapes according to the acceptable rate of angular and velocity changes. The QP controller performance can be seen in *Fig.3*. where a classical PID controller and a fuzzy logic controller are also shown. It is apparent, that the QP controller performs well by means of the length of the trajectory.

Conclusions

A quasi-polynomial representation-based nonlinear control design method has been applied to the kinematics of a differential steering mobile robot in this work. It has been shown, that the quasi-polynomial model of the mobile robot's kinematics extended with the tracking error dynamics has 29 quasi-monomials, i.e. the sizes of matrices appearing in the bilinear matrix inequality that should be solved for a globally stabilizing feedback controller are reasonably great. The resulting controller and the trajectory were compared to the trajectories of a reference PID controller and a fuzzy logic controller. It can be seen that the controller performs satisfactorily. Possible future directions include the application of the LMI and /or BMI cost function to introduce some optimality measure to the problem to be minimised. A next step would be the application of a time dependent goal position (i.e. a trajectory).

Acknowledgement

This research was supported by the European Union and the State of Hungary, co-financed by the European Social Fund in the framework of the TÁMOP 4.2.4. A/2-11-1-2012-0001 'National Excellence Programme'.

REFERENCES

[1] HUANG J., WEN C., WANG W., JIANG Z.-P.: Adaptive output feedback tracking control of a nonholonomic mobile robot, Automatica, *2004*, 50(3), 821–831

[2] MOHARERI O., DHAOUADI R., RAD A.B.: Indirect adaptive tracking control of a nonholonomic mobile robot via neural networks, Neurocomputing, *2012*, 88, 54–66

[3] LI J., GUO X., LI Z., CHEN W.: Stochastic Adaptive Optimal Control of Under-actuated Robots Using Neural Networks, Neurocomputing, *2014*, 142, 190-200

[4] HERNÁNDEZ-BERMEJO B., FAIRÉN V.: Nonpolynomial vector fields under the Lotka-Volterra normal form, Phys. Lett. A, *1995*, 206, 31–37

[5] MAGYAR A., FODOR A.: Quasi-polynomial Control of a Synchronous Generator, Hung. J. Ind. Chem., *2013*, 41(1), 55–61

[6] TZAFESTAS S.G.: Mobile Robot Control I: The Lyapunov-Based Method, in Introduction to Mobile Robot Control (TZAFESTAS S.G., ed.) Elsevier, Oxford, *2014*, 137–183

[7] MAGYAR A., SZEDERKÉNYI G., HANGOS K. M.: Globally stabilizing feedback control of process systems in generalized Lotka-Volterra form, J. Proc. Contr., *2008*, 18(1), 80–91

HUNGARIAN JOURNAL OF INDUSTRY AND CHEMISTRY

HJIC

Advertise upcoming meetings,

conferences, workshops,

new products or services;

make public announcements,

introduce your research laboratory

on the pages of the

Hungarian Journal of Industry and Chemistry

Please contact us if interested!

EDITORIAL OFFICE: UNIVERSITY OF PANNONIA
P.O. BOX 158, VESZPRÉM H-8201 (HUNGARY)
Tel.: +36 (88) 624-746, E-mail: hjic@almos.uni-pannon.hu;
web: hjic.mk.uni-pannon.hu
Felelős szerkesztő: Szilágyi Róbert Károly, PhD
Kiadja: Pannon Egyetem, 8200 Veszprém, Egyetem u. 10.
Levélcím: H-8201 Veszprém, Postafiók 158, Tel.: (88) 624-000
Felelős kiadó: a Pannon Egyetem, Mérnöki Kar dékánja

HUNGARIAN JOURNAL
OF INDUSTRY AND CHEMISTRY
VESZPRÉM
Vol. 42(2) pp. 97–101 (2014)

A NETWORK MODEL FOR SIMULATING THE DYNAMIC BEHAVIOUR OF AN ENERGY DISTRIBUTION NETWORK

LEVENTE BÁLINT,[1]✉ TIBOR DULAI,[2] ÁGNES STARK-WERNER,[2] GERGELY APOSTOL,[1] AND ÁDÁM TOMPOS[1]

[1] Faculty of Information Technology, University of Pannonia, Egyetem u. 10., Veszprém, 8200 HUNGARY
✉E-mail: balintlevente.z@gmail.com
[2] Department of Electrical Engineering and Information Systems, Faculty of Information Technology, University of Pannonia, Egyetem u. 10., Veszprém, 8200 HUNGARY

The aim of this paper is to present the planning and implementation of a network model for an energy distribution network for simulating its dynamical behaviour. The model includes different types of energy sources, distribution centres and consumers. The prepared simulation environment makes it possible to add/remove/modify any type of node – to/form/in the model. Other actions that may be carried out are the initiation/termination of an energy source or change to its production level. The main goal of the simulation is to investigate the effect of an immediate event (such as a power plant failure, decreased production, etc.) on the network and search for the most appropriate substitute possible. The search may happen either on cost bases or time bases. The system created is based on web technology, any user is able to create/save/load his own model and do simulations on it. This work serves as a basis for further work, which involves more complex electrical knowledge and possibilities regarding the network.

Keywords: energy distribution network, energy sources, dynamical behaviour, network model, simulation

Introduction

Energy efficiency has an increasing importance due to cost- and environment-related factors. At the same time, the customer demands have to be satisfied. These circumstances result in a largely heterogeneous energy producing and distributing environment. Renewable energy is applied to a considerable degree in addition to the electricity produced by traditional power plants [1]. This resulted in a system, where different types of energy sources – with different properties, like cost, response time, etc. – are applied in a mixed way. It is a non-trivial task to decide, which sources to apply even in the case of pre-determined demands. Moreover, in practice the amount of the demand appears only when needed.

Earlier efforts implemented simulation environments for analysing the effect of the hybrid manner of an electric network [2, 3]. However, the problem becomes more complex when an immediate negative event happens, e.g. an energy source becomes unavailable or has to decrease its output suddenly. The optimal answer depends on many factors: e.g. how quickly a new energy source can be applied or how much it will cost. Moreover, some types of energy sources are only able to produce discrete levels of output power.

This paper describes a web-based system, which makes it possible to create and modify an energy distribution network (including different types of energy sources and customers, too) with the goal of simulating different immediate events. The requirements to be collected and the network model and its elements are introduced, followed by details of the implementation and simulation.

Requirements: The Desired Properties of the System

Functional requirements include mainly the creation and manipulation of network models and simulations. *Fig.1* presents the possible applications of the system. The interface contains a tree graph-based model whose root is the power source, the inner nodes are the network stations and the leaves are the consumers. The graph's edges are the connections between the components. There are multiple projects in the system, each project contains a model. The main functions of the system are available through the modeling and simulation interfaces. During the simulation the components can be switched on and off. After two hours of simulation a statistic diagram can be viewed for each component of the model, showing its consumption or production. Information about components can be edited while the system is not simulating. Next to the functional requirements, the system-related requirements are that:

- the system has to be web-based,
- no user authentication is needed,
- the reaction time is less than 1 s, even if there are 100 users, and
- any system or communication failure has to be presented by an unambiguous alert to the user.

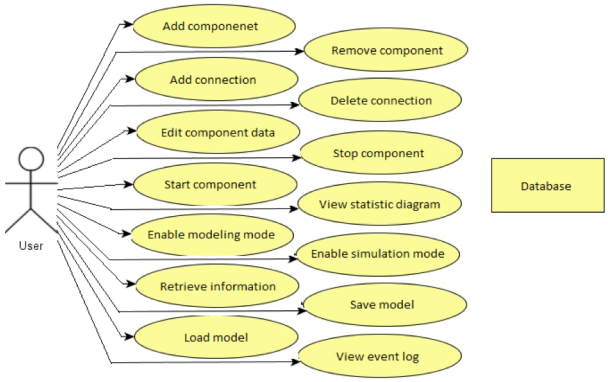

Figure 1: Example uses of the prepared system

The Interface

The interface of the system contains four important elements. On the upper edge is the modelling control bar with the component adding buttons, background theme switcher and save/load buttons. By pressing the load button, the system opens the project selector. The save button must be pressed before loading another project in order to save the current one. Under the right side of the control bar, there is the simulation control panel. There are buttons on it for editing corporate and residential priority orders, and sliders for the importance of certain properties while calculating the priority order of the power sources. There are buttons for starting, stopping, and restarting simulation time. The simulation time begins at 6:00 am and the step time can be set from 1 to 60 minutes. In the bottom left-hand corner, the event-log is located, which indicates the basic events like start/stop simulation, add/remove components in black and important events like system failure or insufficient power in red. All events have a time-stamp. While hovering the mouse over a component, the system shows the detailed properties of the element. Double clicking selects a component or deletes a connection. While a component is selected, the edit, delete and diagram buttons appear in the modelling control bar. The diagram button works only after a minimum of two hours of simulation. In simulation mode the modelling control bar is hidden and double clicking switches a component on/off.

The Network Model and its Elements

As the system's main potential is in handling different types of network nodes and making the investigation of a heterogeneous energy producing and distribution system possible, the elements of the network models and their properties have a huge role. The network nodes can be classified as follows.

Energy Sources

The system considers renewable energy sources (water, bio, wind, solar, and geo), non-renewable energy sources (natural gas, petrol, coal, nuclear), and quick start-up energy sources (gas turbines) when the energy provided by power plants is insufficient for consumers.

Figure 2: Edit power source properties (Név: name or location, Bekapcsolási költség: cost of starting up, Indítási idő: start-up time, Üzemköltség: operational cost, Környezeti szorzó: environmental factor, Optimális sorrend: optimal order)

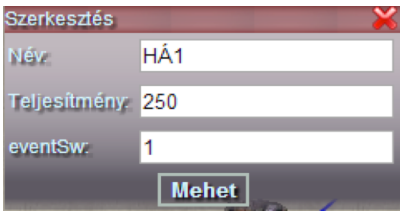

Figure 3: Edit station properties
(Név: name or location, Teljesítmény: power)

Each energy source has a unique name and a maximum output, which defines an upper limit for the source (*Fig.2*). A minimum output is defined as a lower limit, below that the operation is not profitable. Start-up cost is the cost needed to switch on the source, and start-time is the time required to start producing energy. The operational cost is a financial value which is needed for one hour of operation. Power sources have an environmental multiplier. This multiplier is 1 for renewable sources, 0.2 for non-renewable ones and 0.1 for quick start-up sources by default, but it can be edited any time during the modelling. Larger values are better, the maximum is 1 but the value cannot be 0. The system calculates an order between sources from their start-up cost, operational cost and environmental multiplier. This order can be modified by the user before starting the simulation.

Distributing Elements

Distributing elements for the system are power plant stations that distribute the energy to multiple network stations that further distribute the energy to retail stations directly transmit the energy to consumers.

Distributing stations have only two properties (*Fig.3*). They have a unique name to identify them and a maximum throughput, which is the maximum power that the station can distribute to lower stations or consumers. If that limit is reached the station will not pick up more power even if the consumers need more.

Figure 4: Edit consumer properties (Név: name or location, Fogyasztás: consumption, Prioritás: priority)

Consumers

The residential consumers are linked to the model through homes, while corporate consumers include factories, public institutions, etc.

Consumers have a rate of consumption that describes their maximum required power. Current consumption is estimated during the daytime in the simulation. Consumers also have an order of priority that can be modified by the user but corporate consumers always have priority over residential consumers (*Fig.4*).

Connections

Connections have a length property, which will be used for calculating the loss, dissipated by the cables resistance. Networks can be built up by the previously introduced network nodes by connecting them appropriately. The order of connectivity is as follows:

- power sources,
- power plant distribution station,
- network distribution station,
- retail distribution station, and
- consumer.

Connections can be established only in this order regardless of the performance of individual components.

Database and Implementation Details

Properties of the network model elements and the network formed are stored in an associative array that can be used directly by the system. At each time it is saved, this array is stored in JavaScript Object Notation (`JSON`) format in a text file for each project separately.

The database array contains an entry for all components of the model. Every component has an ID, a name, a type and position on the modelled field. Energy sources also have a fuel type, start-up time, start-up cost, running cost, environmental factor, and minimum and maximum performance level attributes. Stations have a defined maximum tolerance. For consumers, there is a stored average consumption rate, which dynamically changes over time. Each object has a sub-array, which stores the ID of any other components that are connected to the current one.

Consumer objects have priority numbers that define the relevance of the consumer. If the power source cannot produce enough energy to satisfy all needs, then the consumer that has the highest priority number will be switched off from the network. The priority order equals the order of creation of components, but the corporate consumers always have preference. The order can be changed by the user any time in modelling mode and during the simulation.

Implementation Details

The program is implemented in JavaScript language with plug-ins like `jQuery` and `jsPlumb`. The plug-in `jQuery` is the most popular extension of the JavaScript language. It makes it easier to select, move, remove or modify the elements on the interface by selecting the element by its ID and modifying its properties. The system uses an in-house `jQuery` plug-in, `windows.js`. This plug-in creates free movable small windows on the interface and fills them with appropriate content defined by the programmer. The `jsPlumb` plug-in is an open-source plug-in for JavaScript, created to visually connect elements on the interface with straight lines or Bezier curves. The database is stored in `JSON` format text files, created and edited by Hypertext Preprocessor (`PHP`) functions and called asynchronously by JavaScript's Asynchronous JavaScript And XML (`AJAX`) protocol. `PHP` is a server-side scripting language, but in our case its only function is to properly save and load database files to the server computer. The whole software can be started in a browser on the user's computer and it connects to the server only while loading or saving the project. The interface is fully interactive, in modelling mode the objects can be moved or removed, in simulating mode switched on and off.

Simulation Possibilities

The system was created for simulating immediate events during the operation of a modelled energy distribution network. After forming the network, the software makes it possible to cause different immediate events. These severe a connection or switch on/off sources, stations and/or consumers. All of these events can be carried out on the graphical interface of the software *(Fig.5)*.

The simulation is daytime-based. It starts at 6:00 am. Users can set the step time from 1 min or sec to 60 min or sec. At the beginning the system distributes the energy produced by the power plant(s) to all consumers in a user defined order. If a power plant does not produce enough power then the last consumer will be switched off and so on. The electricity-related behaviour will be implemented in the future into the software. A possible solution is to build an ideal flow model as a cooperative game over a graph with the sources and consumers located at the nodes, each described by a maximum supply or desired demand and the power lines

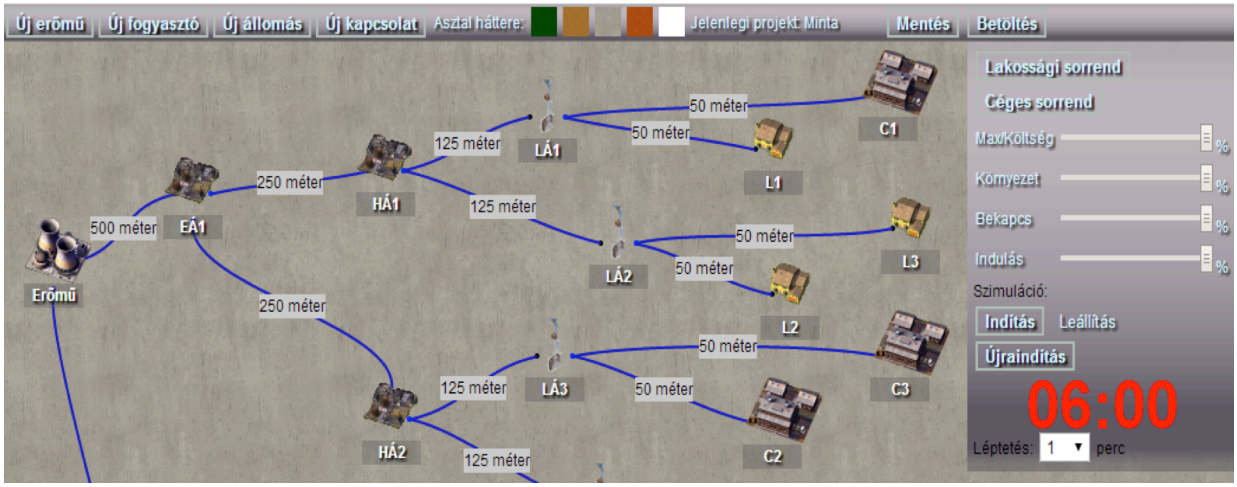

Figure 5: The graphical interface of the software (Új erőmű: new powerplant, Új fogyasztó: new consumer, Új állomás: new station, Új kapcsolat: new connection, Mentés: Save, Betöltés: Load, Lakossági sorrend: order of households, Céges sorrend: order of companies, MaxKöltség: maximum cost, Környezet: environment, Bekaps: start-up, Indulás: begin, Indítás: start, Leállítás: stop, Újraindítás: restart

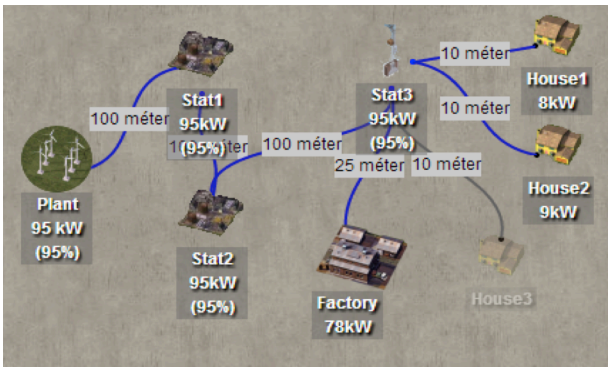

Figure 6: The model of our example (méter: distance in m)

represented by the edges, each with a given power transmission capacity and admittance value describing their ability to transmit electricity. [4] The user is able to initiate immediate events and the system reacts to them in real-time and recalculates the distribution. Calculation of the consumption rate is based on the Hungarian average with a small random factor.

An Example for a Simulation

Let us assume that we have a power plant with a maximum power of 100 kW. The model has one of each type of stations, three households (10-10 kW maximum) and a factory (80 kW maximum) (*Fig.6*). Normally, all of the consumers are satisfied, but in the peak times, when the factory and the houses also approach their maximum consumption, the power will not be enough for every consumer, so the system switches off the retail consumer that is last in the priority order. There will not be a consumption reduction, but a complete shutdown. Subsequently, the plant will have to produce 95% of the maximum power. In this example all of the stations can transfer the maximum of 100 kW, but if a station cannot transfer this, then the consumer with the largest priority number connected to this station will be switched off, regardless of the current level of the power source. If the consumption is too high, it is possible that complete distribution stations are switched off.

Further Developments

The current system can model and simulate a fictional power network with components and connections, but the main goal of the project is to create a simulating software that can model and simulate a real electrical network. It is important to emphasize that the unit of the power of the sources and the consumption are now only kW. We need to include that the voltage of connection cables depends on the length of the connection and the diameter of the cable that are required to calculate the amperage from the resistance of the cable.

International connections transmit 750 kV, and the main network in Hungary transmits 400 kV starting from the power plants (*Fig.7*). The distribution stations transform and divide it to lower values until the voltage reaches the necessary 250 V for retail and 360 V (or more) for corporate consumers. During the transformations, the system needs to use Kirchhoff's current law that states that at any node in an electrical circuit, the sum of currents flowing into that node is equal to the sum of currents flowing out of that node. That means that the system has to calculate amperages for every incoming and outgoing connection of the distribution stations based on the consumption of the consumers and the target voltage of the cables.

The biggest problem of power distribution networks in reality is to satisfy all consumers at all the time, even if the load is very low, without making large changes to the output of the power sources everyday. The current solution in Hungary is nighttime power. Households using electric water heaters have nighttime electric meters, when the consumption of corporate consumers is drastically reduced. This solution slightly optimizes the operation of power plants.

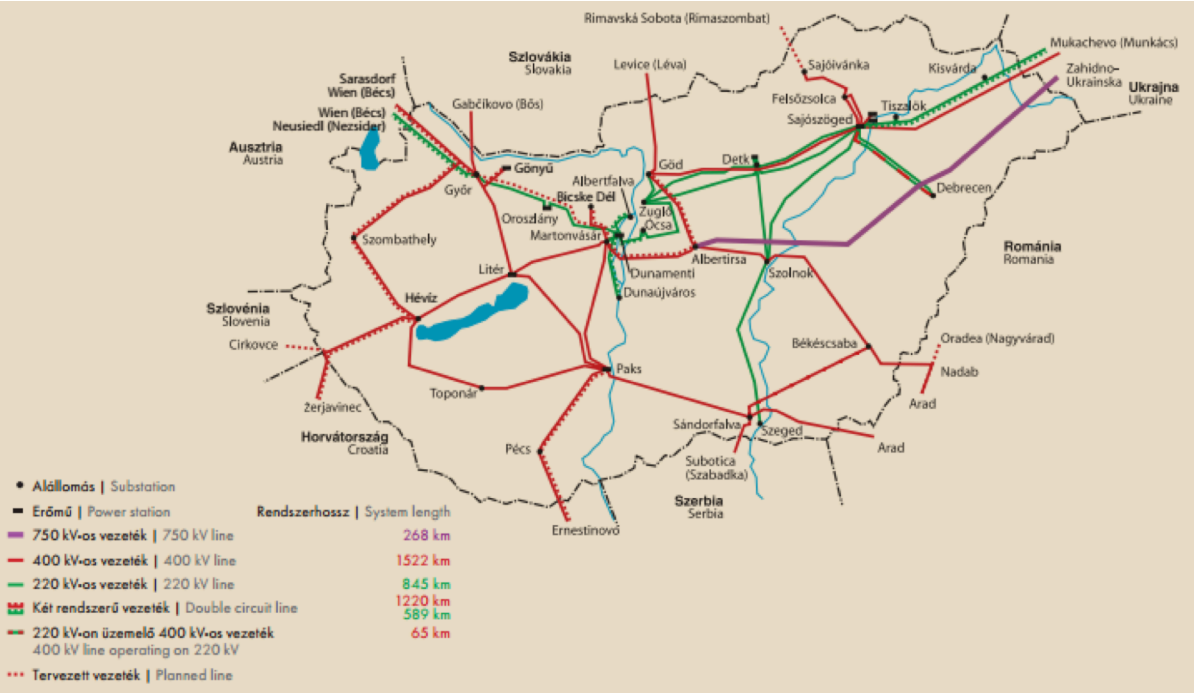

Figure 7: The Hungarian transmission network

Conclusion

This paper presented the planning phase and implementation of a web-based system that makes it possible to construct an energy distribution network together with different types of energy sources and consumers. The simulations are carried out to determine the most effective response to different immediate events (e.g. a sudden network problem or failure of an energy source). The simulation takes into account both cost-related and time-related properties, too. The present state of the software provides a basis for further works, which intend to add deeper electricity-related properties and behaviour to the system.

ACKNOWLEDGEMENT

The authors are thankful for scientific guidance by Prof. KATALIN M. HANGOS from the Computer and Automation Research Institute. We acknowledge the financial support of the Hungarian State and the European Union under the TAMOP-4.2.2.A-11/1/KONV-2012-0072 project.

REFERENCES

[1] BREITNER M.H.: Modeling the transformation of the German energy system until 2050: A multi-criteria, long term optimization problem with many constraints, Operations Res. Proc. *2012*, 369-374

[2] GEYSEN D., BOOIY P., WARMER C.: A framework for simulation and control of hybrid energy networks, Proc. EnergyCon 2014, Dubrovnik, Croatia, *2014*

[3] PADULLES J., AULT G.W., MCDONALD J.R.: An integrated SOFC plant dynamic model for power systems simulation, Int. J. Power Sources *2000*, 86, 495-500

[4] CSERCSIK D., KÓCZY L.Á.: Externalities in the games over electrical power transmission networks, IEHAS Discussion Papers, *2011*, No 1125

HUNGARIAN JOURNAL OF INDUSTRY AND CHEMISTRY

HJIC

Advertise upcoming meetings,

conferences, workshops,

new products or services;

make public announcements,

introduce your research laboratory

on the pages of the

Hungarian Journal of Industry and Chemistry

Please contact us if interested!

EDITORIAL OFFICE: UNIVERSITY OF PANNONIA
P.O. BOX 158, VESZPRÉM H-8201 (HUNGARY)
Tel.: +36 (88) 624-746, E-mail: hjic@almos.uni-pannon.hu;
web: hjic.mk.uni-pannon.hu
Felelős szerkesztő: Szilágyi Róbert Károly, PhD
Kiadja: Pannon Egyetem, 8200 Veszprém, Egyetem u. 10.
Levélcím: H-8201 Veszprém, Postafiók 158, Tel.: (88) 624-000
Felelős kiadó: a Pannon Egyetem, Mérnöki Kar dékánja

HUNGARIAN JOURNAL
OF INDUSTRY AND CHEMISTRY
VESZPRÉM
Vol. 42(2) pp. 103–107 (2014)

ON THE PARAMETRIC UNCERTAINTY OF WEAKLY REVERSIBLE REALIZATIONS OF KINETIC SYSTEMS

GYÖRGY LIPTÁK ✉[1], GÁBOR SZEDERKÉNYI[1,2] AND KATALIN M. HANGOS[1,3]

[1]Process Control Research Group, MTA SZTAKI, Kende u. 13-17, Budapest, 1111, HUNGARY
[2]Faculty of Information Technology, Péter Pázmány Catholic University, Práter u. 50/a, Budapest, 1083, HUNGARY
[3]Department of Electrical Engineering and Information Systems, University of Pannonia, Egyetem u. 10, Veszprém, 8200, HUNGARY
✉E-mail: lipgyorgy@gmail.com

The existence of weakly reversible realizations within a given convex domain is investigated. It is shown that the domain of weakly reversible realizations is convex in the parameter space. A LP-based method of testing if every element of a convex domain admits weakly reversible realizations is proposed. A linear programming method is also presented to compute a stabilizing kinetic feedback controller for polynomial systems with parametric uncertainty. The proposed methods are illustrated using simple examples.

Keywords: parametric uncertainty; computational methods; optimization; kinetic systems

Introduction

The notion of parametric robustness is well-known and central in linear and nonlinear systems and control theory [1]. It is used for ensuring a desirable property, such as stability, in a given domain in the parameter space around a nominal realization having the desired property.

The aim of the paper is to extend the notions and tools of parametric robustness for a class of positive polynomial systems, namely a class of kinetic systems. Only the very first steps are reported here that offer a computationally efficient method for checking one of the many important properties of kinetic systems, their weak reversibility.

Basic Notions and Methods

The basic notions and tools related to reaction kinetic systems and their realizations are briefly summarized in this section.

Kinetic Systems, their Dynamics and Structure

Deterministic kinetic systems with mass action kinetics or simply chemical reaction networks (CRNs) form a wide class of non-negative polynomial systems, that are able to produce all the important qualitative phenomena (e.g. stable/unstable equilibria, oscillations, limit cycles, multiplicity of equilibrium points and even chaotic behaviour) present in the dynamics of nonlinear processes [2].

The general form of dynamic models studied in this paper is the following

$$\dot{x} = M \cdot \psi(x), \tag{1}$$

where $x \in \mathbb{R}^n$ is the state variable and $M \in \mathbb{R}^{n \times m}$. The monomial vector function $\psi : \mathbb{R}^n \to \mathbb{R}^m$ is defined as

$$\psi_j(x) = \prod_{i=1}^{n} x_i^{Y_{ij}}, \;\; j = 1, \ldots, m \tag{2}$$

where $Y \in \mathbb{N}_0^{n \times m}$. The system *Eq.(1)* is kinetic if and only if the matrix M has a factorization

$$M = Y \cdot A_k. \tag{3}$$

The Kirchhoff-matrix A_k has non-positive diagonal and non-negative off-diagonal elements and zero column sums. The matrix pair (Y, A_k) is called the realization of the system *Eq.(1)*.

The chemically originated notions: The chemically originated notions of kinetic systems are as follows: the *species* of the system are denoted by $X_1, \ldots, X_n$, and the concentrations of the species are the state variables of *Eq.(1)*, i.e. $x_i = [X_i] \geq 0$ for $i = 1, \ldots, n$. The structure of kinetic systems is given in terms of its *complexes* C_i, $i = 1, \ldots, m$ that are non-negative linear combinations of the species i.e. $C_i = \sum_{j=1}^{n} [Y]_{ji} X_j$ for $i = 1, \ldots, m$, and therefore Y is also called the *complex composition matrix*.

The reaction graph: The weighted directed graph (or reaction graph) of kinetic systems is $G = (V, E)$, where

$V = \{C_1, C_2, \ldots, C_m\}$ and E denote the set of vertices and directed edges, respectively. The directed edge (C_i, C_j) (also denoted by $C_i \to C_j$) belongs to the reaction graph if and only if $[A_k]_{j,i} > 0$. In this case, the weight assigned to the directed edge is $C_i \to C_j$ is $[A_k]_{j,i}$.

Stoichiometric subspace: Stoichiometric subspace S is given by the span of the reaction vectors

$$S = \{[Y]_{\cdot i} - [Y]_{\cdot j} \mid [A_k]_{ij} > 0\}. \tag{4}$$

The stoichiometric compatibility classes of a kinetic system are the affine translations of the stoichiometric subspace: $(x_0 + S) \cap \mathbb{R}^n_{\geq 0}$.

Structural Properties and Dynamical Behaviour

It is possible to utilize certain structural properties of kinetic systems that enable us to effectively analyze the stability of the system.

Deficiency: There are several equivalent ways to define deficiency. We will use the following definition

$$\delta = \dim(\ker(Y) \cap \mathrm{Im}(B_G)), \tag{5}$$

where B_G is the incidence matrix of the reaction graph. It is easy to see that deficiency is zero if $\ker(Y) = \{0\}$ or equivalently $\mathrm{rank}(Y) = m$.

Weak reversibility: A CRN is called *weakly reversible* if whenever there exists a directed path from C_i to C_j in its reaction graph, then there exists a directed path from C_j to C_i. In graph theoretic terms, this means that all components of the reaction graph are strongly connected components.

Deficiency zero theorem: A weakly reversible kinetic system with zero deficiency has precisely one equilibrium point in each positive stoichiometric compatibility class that is locally asymptotically stable (conjecture: globally asymptotically stable).

Computing Weakly Reversible Realizations Formulated as an Optimization Problem

In this section, first a method for computing weakly reversible realization based on Ref.[3] is briefly presented. We assume that we have a kinetic polynomial system of the form *Eq.(1)*.

We use the fact known from the literature that a realization of a CRN is weakly reversible if and only if there exists a vector with strictly positive elements in the kernel of A_k, i.e. there exists $b \in \mathbb{R}^n_+$ such that $A_k \cdot b = 0$ [4]. Since b is unknown, too, this condition in this form is not linear. Therefore, we introduce a scaled matrix $\tilde{A}_k$

$$\tilde{A}_k = A_k \cdot \mathrm{diag}(b) \tag{6}$$

where $\mathrm{diag}(b)$ is a diagonal matrix with elements of b. It is clear from *Eq.(6)* that $\tilde{A}_k$ is also a Kirchhoff matrix and that $\mathbf{1} \in \mathbb{R}^m$ (the m-dimensional vector containing only ones) lies in kernel of $\tilde{A}_k$. Moreover, it is easy to see that $\tilde{A}_k$ defines a weakly reversible network if and only if A_k corresponds to a weakly reversible network. Then, the weak reversibility and the Kirchhoff property of $\tilde{A}_k$ can be expressed using the following linear constraints

$$\begin{aligned}
\sum_{i=1}^{m} \left[\tilde{A}_k\right]_{ij} &= 0, \quad j = 1, \ldots, m \\
\sum_{i=1}^{m} \left[\tilde{A}_k\right]_{ji} &= 0, \quad j = 1, \ldots, m \\
\left[\tilde{A}_k\right]_{ij} &\geq 0, \quad i, j = 1, \ldots, m,\ i \neq j \\
\left[\tilde{A}_k\right]_{ii} &\leq 0, \quad i = 1, \ldots, m.
\end{aligned} \tag{7}$$

Moreover, the equation *Eq.(3)* is transformed by $\mathrm{diag}(b)$ (we can do this, because $\mathrm{diag}(b)$ is invertible):

$$M \cdot \mathrm{diag}(b) = Y \cdot \underbrace{A_k \cdot \mathrm{diag}(b)}_{\tilde{A}_k} \tag{8}$$

Finally, by choosing an arbitrary linear objective function of the decision variables $\tilde{A}_k$ and b, weakly reversible realizations of the studied kinetic system can be computed (if any exist) in a LP framework using the linear constraints *Eq.(7)* and *(8)*.

Weakly Reversible CRN Realizations

In this section, first the convexity of the weakly reversible Kirchhoff matrix will be shown. After that the practical benefits of this property will be demonstrated in the field of system analysis and robust feedback design.

Convexity of the Weak Reversibility in the Parameter Space

Theorem 1. *Let $A_k^{(1)}$ and $A_k^{(2)}$ be $m \times m$ weakly reversible Kirchhoff matrices. Then the convex combination of the two matrices remains weakly reversible.*

Proof. The idea behind the proof is based on Ref.[5]. A Kirchhoff matrix is weakly reversible if and only if there is a strictly positive vector in its kernel. Therefore strictly positive vectors p_1, p_2 exist such as $A_k^{(1)} \cdot p_1 = 0$ and $A_k^{(2)} \cdot p_2 = 0$. Let us define the following scaled Kirchhoff matrix: $\hat{A}_k^{(1)} = A_k^{(1)} \cdot \mathrm{diag}(p_1)$ and $\hat{A}_k^{(2)} = A_k^{(2)} \cdot \mathrm{diag}(p_2)$. These scaled matrices have identical structures to the original ones. Moreover, $\hat{A}_k^{(1)} \cdot \mathbf{1^{(m)}} = 0$ and $\hat{A}_k^{(2)} \cdot \mathbf{1^{(m)}} = 0$ where the vector $\mathbf{1^{(m)}}$ denotes the m dimensional column vector composed of ones. For that

$$(\lambda \hat{A}_k^{(1)} + (1 - \lambda)\hat{A}_k^{(2)}) \cdot \mathbf{1^{(m)}} = 0. \tag{9}$$

for any $\lambda \in [0, 1]$. Therefore the convex combination of the original two realizations has to be weakly reversible. □

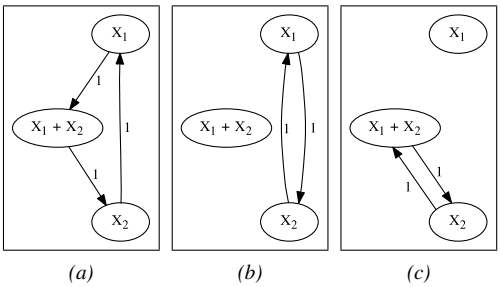

Figure 1: A weakly reversible reaction graphs of the three realizations $(Y, A_k^{(1)})$, $(Y, A_k^{(2)})$ and $(Y, A_k^{(3)})$

Weak Reversibility of CRN Realizations with Parametric Uncertainty

We assume that a CRN with parametric uncertainty is given as

$$\dot{x} = M \cdot \psi(x), \tag{10}$$

where $x \in \mathbb{R}^n$ is the state variable, $\psi \in \mathbb{R}^n \to \mathbb{R}^m$ contains the monomials and the matrix $M \in \mathbb{R}^{n\times m}$ is an element of the following set

$$\mathcal{M} = \Big\{\sum_{i=1}^{l} \alpha_i M_i \;\mid\; (\forall i : \alpha_i \geq 0) \;\wedge\; \sum_{i=1}^{l} \alpha_i = 1\Big\}. \tag{11}$$

The goal is to find a method for checking the weak reversibility of the system *Eq.(10)* for all matrices $M \in \mathcal{M}$.

When all vertices M_i have a weakly reversible realization $(Y, A_k^{(i)})$ then any element of the set $\mathcal{M}$ has a realization (Y, A_k) such that A_k is the convex combination of the Kirchhoff matrices $A_k^{(i)}$. The obtained realization A_k will be weakly reversible due to Theorem 1. Therefore, it is enough to compute a weakly reversible realization for each matrix M_i by using the previously presented LP-based method.

A Simple Example

Let us consider the following polynomial system

$$\begin{bmatrix} \dot{x}_1 \\ \dot{x}_2 \end{bmatrix} = M \cdot \begin{bmatrix} x_1 \\ x_2 \\ x_1x_2 \end{bmatrix}, \tag{12}$$

where M is an arbitrary convex combination of the following three matrices

$$M_1 = \begin{bmatrix} 0 & 1 & -1 \\ 1 & -1 & 0 \end{bmatrix},$$

$$M_2 = \begin{bmatrix} -1 & 1 & 0 \\ 1 & -1 & 0 \end{bmatrix}, \text{and}$$

$$M_3 = \begin{bmatrix} 0 & 1 & -1 \\ 0 & 0 & 0 \end{bmatrix}.$$

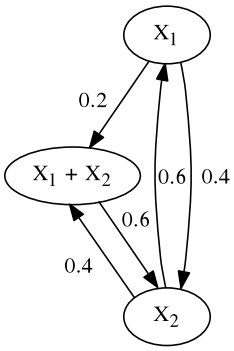

Figure 2: A weakly reversible realization of the convex combination $M = 0.2M_1 + 0.4M_2 + 0.4M_3$

In order to show weak reversibility for all possible convex combinations, we have to find a weakly reversible realization for each matrix M_1, M_2 and M_3. The resulting weakly reversible reaction graphs are depicted in *Fig.1*, while *Fig.2* illustrates an inner point realization which is weakly reversible too.

Computing Kinetic Feedback for a Polynomial System with Parametric Uncertainty

Besides the possible application of the above described LP-based method for robust stability analysis, it can also be used for stabilizing feedback controller design. For this purpose, a generalized version of our preliminary work on kinetic feedback computation for polynomial systems to achieve weak reversibility and minimal deficiency [6] is used here.

The Feedback Design Problem

We assume that the equation of the open-loop polynomial system with linear constant parameter input structure is given as

$$\dot{x} = M \cdot \psi(x) + Bu, \tag{13}$$

where $x \in \mathbb{R}^n$ is the state vector, $u \in \mathbb{R}^p$ is the input and $\psi \in \mathbb{R}^n \to \mathbb{R}^m$ contains the monomials of the open-loop system. The input matrix is $B \in \mathbb{R}^{n\times p}$, the corresponding complex composition matrix is Y with rank m, and $M \in \mathbb{R}^{n\times m}$ is an element of the following set

$$\mathcal{M} = \left\{\sum_{i=1}^{l} \alpha_i M_i \;\mid\; (\forall i : \alpha_i \geq 0) \;\wedge\; \sum_{i=1}^{l} \alpha_i = 1\right\}. \tag{14}$$

Moreover, a positive vector $\overline{x} \in \mathbb{R}^n_{>0}$ being the desired equilibrium point is given as a design parameter. Note that the above polynomial system is not necessarily kinetic, i.e. not necessarily positive, and may not have a positive equilibrium point at all.

The aim of the feedback is to set a region in the state space $R \subseteq \mathbb{R}^n_{\geq 0}$ where $\overline{x}$ is (at least) a locally asymptotically stable equilibrium point of the closed-loop system for all $M \in \mathcal{M}$.

For this purpose we are looking for a feedback in the form

$$u = K\psi(x) \tag{15}$$

which transforms the open-loop system into a weakly reversible kinetic system with zero deficiency for all $M \in \mathcal{M}$ with the given equilibrium point $\overline{x}$.

Feedback Computation

Similarly to the realization computation, the matrix K will be determined by solving an LP problem. The convexity result shows that it is enough to compute one weakly reversible realization $(Y, A_k^{(r)})$ in each vertex M_r to ensure weak reversibility for all possible closed-loop systems. All realizations will have zero deficiency, because of the rank condition $\mathrm{rank}(Y) = m$ [7].

First we note, that the realization $(Y, A_k^{(r)})$ that corresponds to the closed-loop system is

$$M_r + B \cdot K = Y \cdot A_k^{(r)}. \tag{16}$$

where the matrix $A_k^{(r)}$ should be Kirchhoff

$$\begin{aligned} \sum_{i=1}^{m} [\tilde{A}_k]_{ij} &= 0, \quad j = 1, \ldots, m \\ [\tilde{A}_k]_{ij} &\geq 0, \quad i, j = 1, \ldots, m,\ i \neq j \\ [\tilde{A}_k]_{ii} &\leq 0, \quad i = 1, \ldots, m. \end{aligned} \tag{17}$$

In order to obtain a weakly reversible closed-loop system with an equilibrium point $\overline{x}$, the matrix $A_k^{(r)}$ should be weakly reversible and has to have the vector $\psi(\overline{x})$ in its right kernel, i.e.

$$A_k^{(r)} \cdot \psi(\overline{x}) = 0. \tag{18}$$

Finally, by choosing an arbitrary linear objective function of the decision variables $A_k^{(1)}, \ldots, A_k^{(l)}$ and K, the feedback gain K can be computed (if it exists) in a LP framework using the linear constraints *Eqs.(16-18)*.

With the resulting feedback gain K, the point $\overline{x}$ will be an equilibrium point of all possible closed-loop systems, and $\overline{x}$ will be locally asymptotically stable in the region $\mathcal{S} = (\overline{x} + S) \cap \mathbb{R}^n_{\geq 0}$, where S is the stoichiometric subspace of the closed-loop system.

Example

Let the open-loop system be given as

$$\dot{x} = M \begin{bmatrix} x_1 x_2 \\ x_2 x_3 \\ x_1 \end{bmatrix} + \begin{bmatrix} 0 \\ 1 \\ 0 \end{bmatrix} u \tag{19}$$

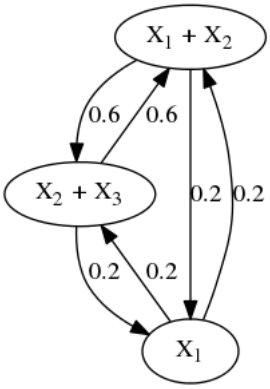

Figure 3: Weakly reversible realization of the closed-loop system, where $M = 0.6M_1 + 0.2M_2 + 0.2M_3$

where M is an arbitrary convex combination of the following three matrices:

$$M_1 = \begin{bmatrix} -1 & 1 & 0 \\ 2 & 1 & 2 \\ 1 & -1 & 0 \end{bmatrix},$$

$$M_2 = \begin{bmatrix} 0 & 0 & 0 \\ 1 & 1 & 3 \\ 0 & 0 & 0 \end{bmatrix}, \text{and}$$

$$M_3 = \begin{bmatrix} 0 & 1 & -1 \\ 2 & 0 & 3 \\ 0 & -1 & 1 \end{bmatrix}.$$

The desired equilibrium point $\overline{x} = [1\ 1\ 1]^T$.

We are looking for a feedback law with gain K which transforms the matrices M_i into weakly reversible kinetic systems with the given equilibrium point.

By solving the feedback design LP optimization problem using the linear constraints *Eqs.(16-18)*, the computed feedback is in the following form:

$$u = \begin{bmatrix} 2 & 1 & 2 \end{bmatrix} \psi(x). \tag{20}$$

Fig.3 depicts a weakly reversible realization of the closed-loop system. The obtained closed-loop system in an inner point of the convex set $\mathcal{M}$ has the following stoichiometric subspace:

$$S = \mathrm{span}\left(\begin{bmatrix} 1 \\ 1 \\ 0 \end{bmatrix} - \begin{bmatrix} 0 \\ 1 \\ 1 \end{bmatrix}, \begin{bmatrix} 1 \\ 1 \\ 0 \end{bmatrix} - \begin{bmatrix} 1 \\ 0 \\ 0 \end{bmatrix} \right). \tag{21}$$

Therefore, the equilibrium point $\overline{x}$ will be asymptotically stable with the region $\mathcal{S} = (\overline{x} + S) \cap \mathbb{R}^n_{\geq 0}$. Note, that one should choose the initial value of the state variables from $\mathcal{S}$.

Fig.4 shows the time dependent behaviour of the closed-loop solutions started from different initial points in $\mathcal{S}$.

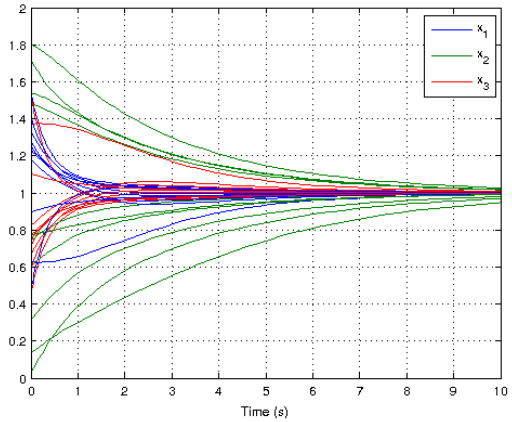

Figure 4: Time-domain simulation of the closed-loop system

Conclusion

It is shown in this paper that the domain of weakly reversible realizations is convex in the parameter space. This property is utilized for developing methods in system analysis and robust control design. An LP-based optimization method is proposed for testing if every element of a convex domain given by its extremal matrices admits a weakly reversible realization. An LP-based feedback design method is also proposed that guarantees stability with a desired equilibrium point. The proposed methods are illustrated with simple examples.

REFERENCES

[1] SILJAK D.: Parameter space methods for robust control design: a guided tour, Aut. Contr., IEEE Transactions on, *1989*, 34(7), 674–688

[2] ANGELI D.: A tutorial on chemical network dynamics, Eur. J. Contr., *2009*, 15, 398–406

[3] SZEDERKÉNYI G., HANGOS K. M., TUZA Z.: Finding weakly reversible realizations of chemical reaction networks using optimization, MATCH Commun. Math. Comp. Chem., *2012*, 67, 193–212

[4] FEINBERG M., HORN F.: Chemical mechanism structure and the coincidence of the stoichiometric and kinetic subspaces, Arch. Rational Mechanics and Analysis, *1977*, 66(1), 83–97

[5] RUDAN J., SZEDERKÉNYI G., HANGOS K.M., PÉNI T.: Polynomial time algorithms to determine weakly reversible realizations of chemical reaction networks, J. Math. Chem., *2014*, 52(5), 1386–1404

[6] LIPTÁK G., SZEDERKÉNYI G., HANGOS K.M.: Kinetic feedback computation for polynomial systems to achieve weak reversibility and minimal deficiency, 13th Eur. Control Conf. ECC, Strasbourg, France, *2014*, 2691–2696

[7] ANGELI D., LENHEE, P.D., SONTAG E.D.: On the structural monotonicity of chemical reaction networks, Proc. 45th IEEE Conf. Decision and Control, *2006*, 7–12

HUNGARIAN JOURNAL OF INDUSTRY AND CHEMISTRY

HJIC

Advertise upcoming meetings,

conferences, workshops,

new products or services;

make public announcements,

introduce your research laboratory

on the pages of the

Hungarian Journal of Industry and Chemistry

Please contact us if interested!

EDITORIAL OFFICE: UNIVERSITY OF PANNONIA
P.O. BOX 158, VESZPRÉM H-8201 (HUNGARY)
Tel.: +36 (88) 624-746, E-mail: hjic@almos.uni-pannon.hu;
web: hjic.mk.uni-pannon.hu
Felelős szerkesztő: Szilágyi Róbert Károly, PhD
Kiadja: Pannon Egyetem, 8200 Veszprém, Egyetem u. 10.
Levélcím: H-8201 Veszprém, Postafiók 158, Tel.: (88) 624-000
Felelős kiadó: a Pannon Egyetem, Mérnöki Kar dékánja

HUNGARIAN JOURNAL
OF INDUSTRY AND CHEMISTRY
VESZPRÉM
Vol. 42(2) pp. 109–113 (2014)

STABILITY AND PARAMETER SENSITIVITY ANALYSES OF AN INDUCTION MOTOR

ATTILA FODOR[1], ROLAND BÁLINT✉[1], ATTILA MAGYAR[1], AND GÁBOR SZEDERKÉNYI[2]

[1]Department of Electrical Engineering and Information Systems, University of Pannonia,
Egyetem u. 10., Veszprém, 8200, HUNGARY
[2]Pazmány Péter Catholic University, Práter u. 50/a, Budapest, 1083, HUNGARY
✉E-mail: balint.roland27@gmail.com

A simple dynamical model of an induction motor is derived and analyzed in this paper based on engineering principles that describe the mechanical phenomena together with the electrical model. The used state space model consists of nonlinear state equations. The model has been verified under the usual controlled operating conditions when the speed is controlled. The effect of load on the controlled induction motor has been analyzed by simulation. The sensitivity analysis of the induction motor has been applied to determine the model parameters to be estimated.

Keywords: induction motor, stability analysis, sensitivity analysis

Introduction

Induction motors (IM) are the most commonly used electrical rotating machines in several industrial applications. Irrespective of size and the application area, these motors share the most important dynamical properties, and their dynamical models have a similar structure.

Because of the specialties and great practical importance of IMs in industrial applications, their modelling for control purposes is well investigated in the literature. Besides basic textbooks [1-3], there are several papers that describe the modelling and use the developed models for the design of different types of controllers: vector control [1, 4], sensorless vector control [5] and direct torque control (DTC) [6]. The aim of this paper is to build a simple dynamical model of the IM and to perform its parameter sensitivity analysis. The results of this analysis will be the basis of the next step since the final aim of our study is to estimate the parameters of the IM and design a controller that can control the speed and torque of the IM. The state space model has been implemented in the Matlab/Simulink environment which enables us to analyze the parametric sensitivity based on simulation experiments.

Nonlinear Model of an Induction Motor

In this section a state space model of an induction motor (IM) is presented. The model development is largely based on Refs.[1, 8-10]. For constructing the IM model, the following modelling assumptions are made:

1. a symmetrical triphase stator winding system is assumed,
2. the flux density is radial in the air gap,
3. the copper loss and the slots in the machine can be neglected,
4. the spatial distribution of the stator fluxes and apertures wave are considered to be sinusoidal,
5. stator and rotor permeability are assumed to be infinite with linear magnetic properties.

According to the above modelling conditions the mathematical description of the IM is developed through the space-vector theory. If the voltage of the stator is presumed to be the input excitation of the machine, then the spatial distribution along the stator of the x phase voltage can be described by the complex vector $v_{\mathrm{sx}}(t)$. We can determine the orientation of the voltage vector v_{s}, the direction of the respective phase axis and the voltage polarity.

$$\begin{aligned} i_{\mathrm{s}}(t) &= \frac{2}{3}\left(a^0 \cdot i_{\mathrm{sa}}(t) + a^1 \cdot i_{\mathrm{sb}}(t) + a^2 \cdot i_{\mathrm{sc}}(t)\right) \\ &= \sqrt{2} \cdot i_{\mathrm{eff}}(t) \cdot e^{j\omega_0 t + \frac{\pi}{2} + \varphi_i}, \end{aligned} \tag{1}$$

where a is the e^{j120^o} vector and i_{sa}, i_{sb} and i_{sc} are the following:

$$i_{\mathrm{sa}}(t) = \mathrm{Re}(a^0 \cdot i_{\mathrm{s}}(t)) = \mathrm{Re}(i_{\mathrm{s}}(t)),$$

$$i_{\mathrm{sb}}(t) = \mathrm{Re}(a^2 \cdot i_{\mathrm{s}}(t)), \text{and}$$

$$i_{\mathrm{sc}}(t) = \mathrm{Re}(a^1 \cdot i_{\mathrm{s}}(t)).$$

In *Eq.(1)*, 2/3 is the normalizing factor. The flux density distribution can be obtained by integrating the current density wave along the cylinder of the stator. The flux linkage wave is a system variable, because it contains detailed information about the winding geometry.

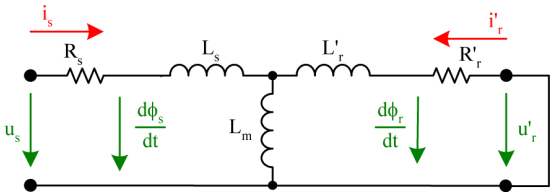

Figure 1: The equivalent circuit of the IM

The rotating flux density wave induces voltages in the individual stator windings. Thus stator voltage $v_{\mathrm{s}}(t)$ can be represented as the overall distributed voltages in all phase windings:

$$\begin{aligned} v_{\mathrm{s}}(t) &= \frac{2}{3}\left(a^0 \cdot v_{\mathrm{sa}}(t) + a^1 \cdot v_{\mathrm{sb}}(t) + a^2 \cdot v_{\mathrm{sc}}(t)\right) \\ &= \sqrt{2} \cdot v_{\mathrm{eff}}(t) \cdot e^{j\omega_0 t + \frac{\pi}{2} + \varphi_u}, \end{aligned} \tag{2}$$

where a is the e^{j120^o} vector and i_{sa}, i_{sb} and i_{sc} are the following:

$$v_{\mathrm{sa}}(t) = \mathrm{Re}(a^0 \cdot u_{\mathrm{s}}(t)) = \mathrm{Re}(u_{\mathrm{s}}(t)),$$
$$v_{\mathrm{sb}}(t) = \mathrm{Re}(a^2 \cdot u_{\mathrm{s}}(t)), \text{and}$$
$$v_{\mathrm{sc}}(t) = \mathrm{Re}(a^1 \cdot u_{\mathrm{s}}(t)).$$

Considering the stator of the IM as the primer side of the transformer, then using Kirchoff's voltage law the following equation can be written (*Fig.1*):

$$v_{\mathrm{s}}(t) = i_{\mathrm{s}}(t) \cdot R_{\mathrm{s}} + \frac{d\phi_{\mathrm{s}}(t)}{dt}. \tag{3}$$

As for the secondary side of the transformer, it can be deduced that the same relationship is true for the rotor side space vectors:

$$v_{\mathrm{r}}(t) = i_r(t) \cdot R_{\mathrm{r}} + \frac{d\phi_{\mathrm{r}}(t)}{dt} = 0. \tag{4}$$

Eqs.(3) and *(4)* describe the electromagnetic interaction as the connection of first order dynamical subsystems:

$$\phi_{\mathrm{s}}(t) = i_{\mathrm{s}}(t) \cdot L_{\mathrm{s}} + i_{\mathrm{r}}(t) \cdot L_{\mathrm{m}}, \text{and} \tag{5}$$

$$\phi_{\mathrm{r}}(t) = i_{\mathrm{s}}(t) \cdot L_{\mathrm{m}} + i_{\mathrm{r}}(t) \cdot L_{\mathrm{r}}. \tag{6}$$

Since four complex variables $(i_{\mathrm{s}}(t)$, $i_{\mathrm{r}}(t)$, $\phi_{\mathrm{s}}(t)$, and $\phi_{\mathrm{r}}(t))$ are presented in *Eqs.(5)* and *(6)*, flux equations are needed to complete the relationship between them.

The mechanical power $(P_{\mathrm{mech}}(t))$ of the IM can be defined as:

$$P_{\mathrm{mech}}(t) = \frac{W_{\mathrm{mech}}(t)}{dt}, \tag{7}$$

where the mechanical energy $(P_{\mathrm{mech}}(t))$ in the rotating system can be given by the following expression:

$$P_{\mathrm{mech}}(t) = \frac{W_{\mathrm{mech}}(t)}{dt} = T_{\mathrm{mech}}(t) \cdot \omega_{\mathrm{r}}, \tag{8}$$

where $T_{\mathrm{e}}(t)$ is the torque and ω_{r} is the angular velocity of the IM. Afterwards the energy balance of the IM is as follows:

$$W_{\mathrm{e}} = W_{\mathrm{mech}} + W_{\mathrm{R}} + W_{\mathrm{Field}}, \tag{9}$$

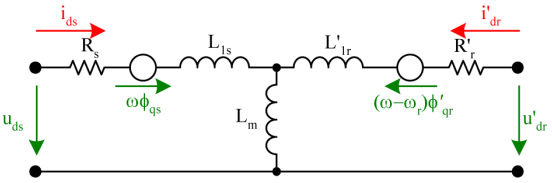

Figure 2: The equivalent circuit of the d-axis of the IM

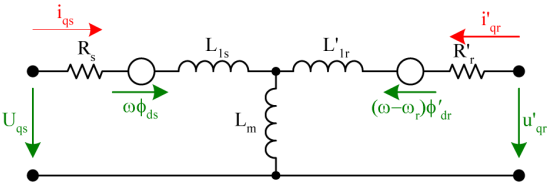

Figure 3: The equivalent circuit of the q-axis of the IM

where

$$P_{\mathrm{e}} = \frac{W_{\mathrm{e}}(t)}{dt} = \frac{3}{2}\mathrm{Re}\left(u_{\mathrm{s}} \cdot i_{\mathrm{s}} + u_{\mathrm{r}} \cdot i_{\mathrm{r}}\right) \tag{10}$$

is the input electrical power,

$$P_{\mathrm{R}} = \frac{W_{\mathrm{R}}(t)}{dt} = \frac{3}{2}\mathrm{Re}\left(R_{\mathrm{s}} \cdot |i_{\mathrm{s}}|^2 + R_{\mathrm{r}} \cdot |i_{\mathrm{r}}|^2\right) \tag{11}$$

represents the resistive power losses and

$$P_{\mathrm{Field}} = \frac{W_{\mathrm{Field}}(t)}{dt} = \frac{3}{2}\mathrm{Re}\left(\frac{d\phi_{\mathrm{s}}}{dt} i_{\mathrm{s}} + \frac{d\phi_{\mathrm{r}}}{dt} i_{\mathrm{r}}\right) \tag{12}$$

is the air gap power. Using *Eqs.(8-12)*,

$$P_{\mathrm{mech}}(t) = T_{\mathrm{mech}}(t) \cdot \omega_{\mathrm{r}} = \frac{3}{2} \cdot \frac{L_{\mathrm{m}}}{L_{\mathrm{r}}} \cdot \phi_{\mathrm{s}}(t) \times i_{\mathrm{s}}(t), \text{and} \tag{13}$$

$$T_{\mathrm{e}} = 1.5p \cdot (\phi_{\mathrm{ds}} i_{\mathrm{qs}} - \phi_{\mathrm{qs}} i_{\mathrm{ds}}). \tag{14}$$

The equivalent circuit of the IM can be decomposed to direct axis and quadratic axis components by Park's transformation as shown in *Figs.2* and *3*.

The actual terminal voltage v of the windings can be written in the form

$$v = \pm \sum_{j=1}^{J} (R_j \, i_j) \pm \sum_{j=1}^{J} \left(\frac{\mathrm{d}\phi_j}{\mathrm{dt}}\right), \tag{15}$$

where i_j are the currents, R_j are the winding resistances, and ϕ_j are the flux linkages. The positive directions of the stator currents point out of the IM terminals.

By composing the d and q axes of the IM the following equations can be written:

$$v_{\mathrm{qs}} = R_{\mathrm{s}} \cdot i_{\mathrm{qs}} + \frac{\phi_{\mathrm{qs}}}{dt} + \omega \cdot \phi_{\mathrm{ds}}, \tag{16}$$

$$v_{\mathrm{ds}} = R_{\mathrm{s}} \cdot i_{\mathrm{ds}} + \frac{\phi_{\mathrm{ds}}}{dt} - \omega \cdot \phi_{\mathrm{qs}}, \tag{17}$$

$$v_{\mathrm{qr}} = R'_{\mathrm{r}} \cdot i'_{\mathrm{ds}} + \frac{\phi'_{\mathrm{dr}}}{dt} + (\omega - \omega_{\mathrm{r}}) \cdot \phi'_{\mathrm{dr}}, \text{and} \tag{18}$$

$$v_{\mathrm{dr}} = R'_{\mathrm{r}} \cdot i'_{\mathrm{dr}} + \frac{\phi'_{\mathrm{dr}}}{dt} - (\omega - \omega_{\mathrm{r}}) \cdot \phi'_{\mathrm{qr}}. \tag{19}$$

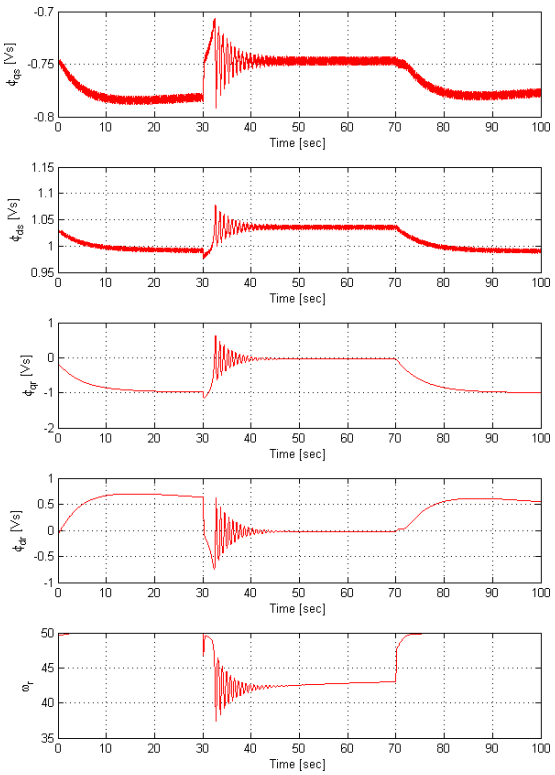

Figure 4: Response to the step change of the speed-controlled IM

$$\frac{d\omega_{\rm m}}{dt} = \frac{1}{2H}(T_{\rm e} - F \cdot \omega_{\rm m} - T_{\rm mech}) \tag{20}$$

where ω is the reference frame angular velocity, $\omega_{\rm r}$ is the electrical angular velocity,

$$\phi_{\rm qs} = L_{\rm s} \cdot i_{\rm qs} + L_{\rm m} i'_{\rm qr}, \tag{21}$$

$$\phi_{\rm ds} = L_{\rm s} \cdot i_{\rm ds} + L_{\rm m} i'_{\rm dr}, \tag{22}$$

$$\phi_{\rm qr} = L_{\rm r} \cdot i'_{\rm qr} + L_{\rm m} i'_{\rm qs}, \text{and} \tag{23}$$

$$\phi_{\rm dr} = L_{\rm r} \cdot i'_{\rm dr} + L_{\rm m} i'_{\rm ds}. \tag{24}$$

The above model can be written in state space form by expressing the time derivative of the fluxes and ω from the voltage and swing equations *Eqs.(21-24)*. The nonlinear state space model of the IM is given by *Eqs.(25-29)*:

$$\begin{aligned}\frac{d\phi_{\rm qs}}{dt} &= \frac{-R_{\rm s}}{L_{\rm s} - \frac{L_{\rm m}^2}{L'_{\rm r}}} \cdot \phi_{\rm qs} \frac{R_{\rm s} \cdot L_{\rm m}}{L'_{\rm r}(L_{\rm s} - \frac{L_{\rm m}^2}{L'_{\rm r}})} \cdot \phi'_{\rm qr} \\ &- \omega \cdot \phi_{\rm ds} + v_{\rm qs},\end{aligned} \tag{25}$$

$$\begin{aligned}\frac{d\phi_{\rm ds}}{dt} &= \frac{-R_{\rm s}}{L_{\rm s} - \frac{L_{\rm m}^2}{L'_{\rm r}}} \cdot \phi_{\rm ds} + \frac{R_{\rm s} \cdot L_{\rm m}}{L'_{\rm r}(L_{\rm s} - \frac{L_{\rm m}^2}{L'_{\rm r}})} \cdot \phi'_{\rm dr} \\ &- \omega \cdot \phi_{\rm qs} + v_{\rm ds},\end{aligned} \tag{26}$$

$$\begin{aligned}\frac{d\phi'_{\rm qr}}{dt} &= \frac{-R'_{\rm r}}{L_{\rm m} - \frac{L'_{\rm r} \cdot L_{\rm s}}{L_{\rm m}}} \cdot \phi_{\rm qs} \\ &+ \frac{-R'_{\rm r} \cdot L_{\rm s}}{L_{\rm m} \cdot (L_{\rm m} - \frac{L'_{\rm r} \cdot L_{\rm s}}{L_{\rm m}})} \cdot \phi'_{\rm qr} \\ &- \omega \cdot \phi'_{\rm dr} + \omega_{\rm r} \cdot \phi'_{\rm dr} + v_{\rm qr},\end{aligned} \tag{27}$$

$$\begin{aligned}\frac{d\phi'_{\rm dr}}{dt} &= \frac{-R'_{\rm r}}{L_{\rm m} - \frac{L'_{\rm r} \cdot L_{\rm s}}{L_{\rm m}}} \cdot \phi_{\rm ds} \\ &+ \frac{-R'_{\rm r} \cdot L_{\rm s}}{L_{\rm m} \cdot (L_{\rm m} - \frac{L'_{\rm r} \cdot L_{\rm s}}{L_{\rm m}})} \cdot \phi'_{\rm dr} \\ &+ \omega \cdot \phi'_{\rm qr} - \omega_{\rm r} \cdot \phi'_{\rm qr} + v_{\rm dr}, \text{and}\end{aligned} \tag{28}$$

$$\begin{aligned}\frac{d\omega_{\rm r}}{dt} &= \frac{1}{2H} \cdot \frac{1.5 \cdot p \cdot L_{\rm m}}{L_{\rm m} \cdot (L_{\rm s} - \frac{L_{\rm m}^2}{L'_{\rm r}})} \cdot \phi'_{\rm dr} \cdot \phi_{\rm qs} \\ &- \frac{1}{2H} \cdot \frac{1.5 \cdot p \cdot L_{\rm m}}{L_{\rm m} \cdot (L_{\rm s} - \frac{L_{\rm m}^2}{L'_{\rm r}})} \cdot \phi'_{\rm qr} \cdot \phi_{\rm ds} \\ &- \frac{F}{2H} \cdot \omega_{\rm r} - \frac{T_{\rm m}}{2H}.\end{aligned} \tag{29}$$

The state vector of the above model is $\mathbf{x}$=$[\phi_{\rm qs},\ \phi_{\rm ds},\ \phi'_{\rm qr},\ \phi'_{\rm dr},\ \omega_{\rm r}]^T \in \mathbb{R}^5$, and the input variables are organized in terms of the the input vector $\mathbf{u}$=$[v_{\rm q},\ v_{\rm d},\ -T_{\rm mech}]^T \in \mathbb{R}^3$. It is assumed that all the state variables can be measured i.e. $\mathbf{y} = \mathbf{x}$.

Model Validation

The dynamical properties of the IM have been investigated. The response of the speed-controlled motor has been tested under step-like changes. The simulation results are shown in *Fig.4*, where the fluxes ($\phi_{\rm qs}$, $\phi_{\rm ds}$, $\phi'_{\rm qr}$, and $\phi'_{\rm dr}$) and the angular velocity (ω) are shown.

Model Analysis

The above model *Eqs.(21-24)* has been verified by simulation against engineering intuition.

Local Stability Analysis

As the final aim of our research is to estimate the parameters of a particular Grundfos IM, first of all the resistances ($R_{\rm s}$ and $R_{\rm r}$) of the IM were measured. Afterwards the values of the inductances ($L_{\rm ls}$, $L_{\rm lr}$ and $L_{\rm m}$) and the mechanical parameters (H and F) of a similar IM with similar $R_{\rm s}$ and $R_{\rm r}$ found in the literature have been used. The parameters used during the model and the sensitivity analyses are the following:

$$\begin{aligned} R_{\rm s} &= 0.196\ \text{Ohm} \\ R_{\rm r} &= 0.0191\ \text{Ohm} \\ L_{\rm ls} &= 0.0397\ \text{H} \\ L_{\rm lr} &= 0.0397\ \text{H} \\ L_{\rm m} &= 1.354\ \text{H} \\ H &= 0.095 \\ F &= 0.0548 \\ p &= 1 \end{aligned} \tag{30}$$

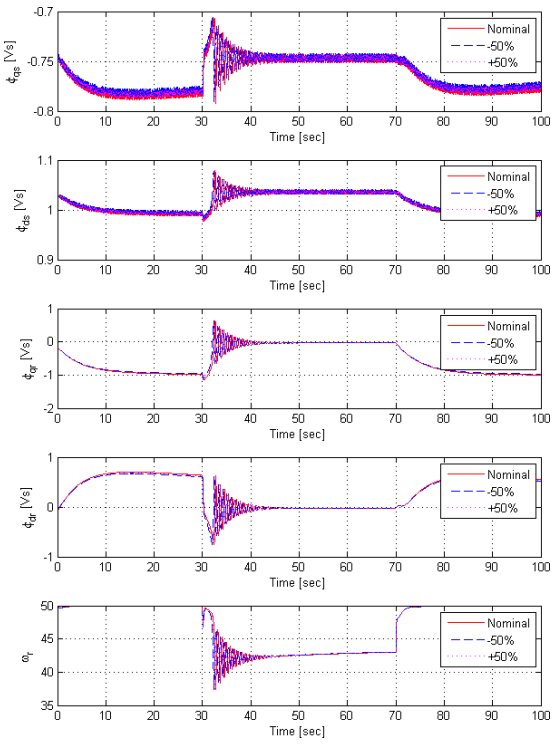

Figure 5: The model state variables for a $\pm 50\%$ change of L_{m}

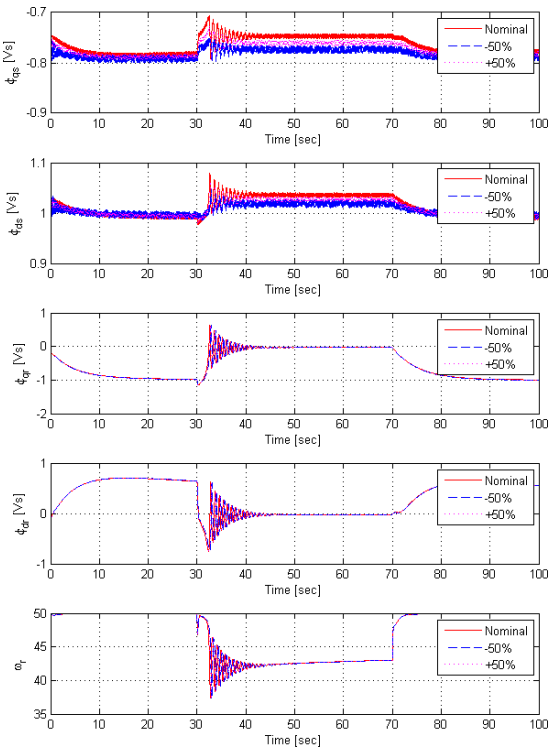

Figure 6: The model state variables for a $\pm 50\%$ change in R_{s}

It can easily be seen that the IM model is nonlinear since there are products of two state variables in the following equations:

- *Eq.(27)*: ϕ'_{dr} is multiplied by ω_{r}
- *Eq.(28)*: ϕ'_{qr} is multiplied by ω_{r}
- *Eq.(29)*: ϕ'_{dr} is multiplied by ϕ_{qs}
- *Eq.(29)*: ϕ'_{qr} is multiplied by ϕ'_{ds}

For the local stability analysis we have to calculate the eigenvalues of the system. The examined equilibrium point is

$$\begin{aligned} \phi_{\mathrm{qs}} &= -0.744 \ \mathrm{Vs} \\ \phi_{\mathrm{ds}} &= 1.0287 \ \mathrm{Vs} \\ \phi'_{\mathrm{qr}} &= -0.174 \ \mathrm{Vs} \\ \phi'_{\mathrm{dr}} &= -0.087 \ \mathrm{Vs} \\ \omega_{\mathrm{r}} &= 48.477 \ \mathrm{s}^{-1} \end{aligned} \tag{31}$$

The numerical value of the Jacobian of the nonlinear model (i.e. the state matrix of the locally linearized model) is as follows:

$$\begin{bmatrix} -2.504 & -50 & 2.4328 & 0 & 0 \\ 50 & -2.504 & 0 & 2.4328 & 0 \\ 0.2370 & 0 & -0.244 & -1.522 & 0 \\ 0 & 0.2370 & 1.5222 & -0.244 & 0 \\ -8.617 & 17.077 & 0 & 0 & -0.288 \end{bmatrix}. \tag{32}$$

The eigenvalues of the state matrix of the linearized systems are:

$$\begin{aligned} \lambda_{1,2} &= -2.504 \pm \mathrm{j}49.98, \\ \lambda_{3,4} &= -0.243 \pm \mathrm{j}1.534, \text{and} \\ \lambda_5 &= -0.288 \end{aligned} \tag{33}$$

It is apparent that the real parts of the eigenvalues are negative with small magnitudes.

Parameter Sensitivity Analysis

the sensitivity of the nonlinear model to the mutual inductance has been investigated. The steady state value of the system variables does not change (as is apparent in *Fig.5*) even for a considerably large change in L_{m}. Sensitivity analysis of the inductances L_{lr}, L_{ls} of the stator and rotor, resistances of the stator R_{s} and the damping constant F has also been investigated. In this investigation it can be seen that the values of the state variables were changed a bit, as shown in *Fig.6*.

The analysis of the resistances of the rotor R'_{r} and the inertia H of the rotor showed that every value of the state variables changed significantly, as shown in *Fig.7*.

As a final result of the sensitivity analysis, we can define the following groups of parameters:

- *Not sensitive*: Mutual inductance L_{m}. Since the state space model of interest is insensitive in this respect, the values of this parameter cannot be reliably determined from measurement data using any parameter estimation method.
- *Sensitive*: These sensitive parameters are candidates for parameter estimation.
  - Less: inductances L_{lr} and L_{ls}, resistance of the stator R_{s} and the damping constant F.
  - More: resistances of the rotor R'_{r} and the inertia H of the rotor.
- *Critically sensitive*: none.

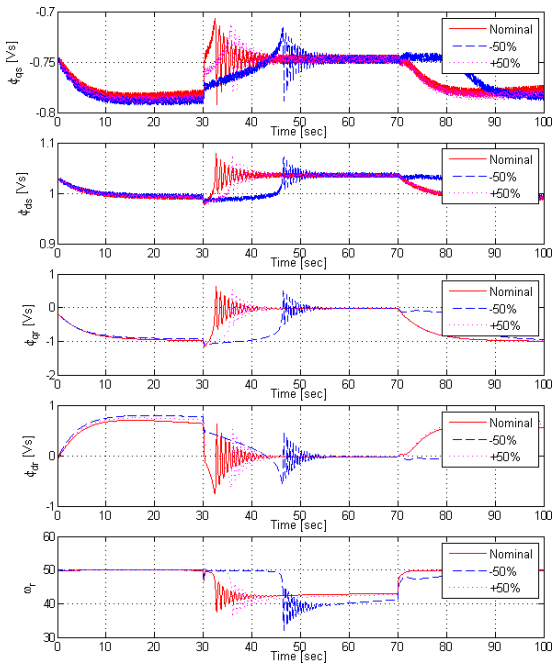

Figure 7: The model state variables for a $\pm 50\%$ change in H

Conclusion

The simple nonlinear dynamical model of an IM has been investigated in this paper. It has been shown that the model is locally asymptotically stable with regards to a physically meaningful equilibrium state. The effect of the controlled generator has been analyzed by simulation using a traditional PI controller. It has been found that the controlled system is stable and can follow the set-point changes. Seven parameters of the model were selected for sensitivity analysis, and the sensitivity of the state variables has been investigated. As a result, the parameters were partitioned into three groups. Based on the results presented here, a future aim is to estimate the parameters of the model for a real system from measurements. The sensitivity analysis enables us to select the candidates for estimation that are inductances L_{lr} and L_{ls}, resistances R_{s} and R_{r}, the damping constant F and the inertia H. An additional future aim is to develop a model for control purposes and investigate different controllers before applying them on real systems.

ACKNOWLEDGEMENT

We acknowledge the financial support of this work by the Hungarian State and the European Union under the TAMOP-4.2.2.A-11/1/KONV-2012-0072 project. We acknowledge also the investigated IM of Grundfos Hungary Producer Ltd.

SYMBOLS

C_1, C_2, C_3	constant
F	damping constant
ϕ_{qs} and ϕ_{ds}	q and d components of the stator flux
ϕ'_{qr} and ϕ'_{dr}	q and d components of the reduced rotor flux
H	inertia constant
i_{qs} and i_{ds}	q and d components of the stator current
i'_{qr} and i'_{dr}	q and d components of the reduced rotor current
L_{m}	mutual inductance
p	number of pole pairs
R_{r} and L_{r}	rotor resistance and inductance
R'_{r} and L'_{r}	reduced value of rotor resistance and inductance
R_{s} and L_{s}	stator resistance and inductance
v_{d} and v_{q}	q and d components of the stator voltage
ω	angular velocity of the magnetic field
ω_{r}	angular velocity of the rotor
T_{mech}	mechanical torque

REFERENCES

[1] VAS P.: Artifical-intelligence-Based Electrical Machines and Drives, Oxford University Press, *1999*

[2] VAS P.: Sensorless Vector and Direct Torque Control. Oxford University Press, *1998*.

[3] ZHENG L., FLETCHER J.E., WILLIAMS B.W. HE X.: Dual-Plane Vector Control of a Five-Phase Induction Machine for an Improved Flux Pattern, IEEE Transac. Ind. Elec., *2008*, 55(5), 1996–2005

[4] LEVI E.: Impact of Iron Loss on Behavior of Vector Controlled Induction Machines, IEEE Transac. Ind. Appl., *1995*, 31(6), 1287–1296

[5] HASEGAWA M., MATSUI K.: Robust Adaptive Full-Order Observer Design with Novel Adaptive Scheme for Speed Sensorless Vector Controlled Induction Motors, Proc. 28th Annual Conf. Industrial Electronics Society, IEEE 2002, *2002*, 1, 83–88

[6] GEYER T., PAPAFOTIOU G., MORARI M.: Model Predictive Direct Torque Control-Part I: Concept, Algorithm, and Analysis, IEEE Transac. Ind. Elec., *2009*, 56(6), 1894–1905

[7] KRAUSE P.C., WASYNCZUK O., SUDHOFF S.D.: Analysis of Electric Machinery, IEEE Press, New York, *1995*

[8] MOHAN N., UNDELAND T.M., ROBBINS W.P.: Power Electronics: Converters, Applications, and Design, John Wiley & Sons Inc., New York, *1995*

[9] HATOS P., FODOR, A., MAGYAR A.: Parameter sensitivity analysis of an induction motor, Hung. J. Ind. Chem., *2011*, 39(1), 157–161

HUNGARIAN JOURNAL OF INDUSTRY AND CHEMISTRY

HJIC

Advertise upcoming meetings,

conferences, workshops,

new products or services;

make public announcements,

introduce your research laboratory

on the pages of the

Hungarian Journal of Industry and Chemistry

Please contact us if interested!

EDITORIAL OFFICE: UNIVERSITY OF PANNONIA
P.O. BOX 158, VESZPRÉM H-8201 (HUNGARY)
Tel.: +36 (88) 624-746, E-mail: hjic@almos.uni-pannon.hu;
web: hjic.mk.uni-pannon.hu
Felelős szerkesztő: Szilágyi Róbert Károly, PhD
Kiadja: Pannon Egyetem, 8200 Veszprém, Egyetem u. 10.
Levélcím: H-8201 Veszprém, Postafiók 158, Tel.: (88) 624-000
Felelős kiadó: a Pannon Egyetem, Mérnöki Kar dékánja